工學博士學位論文

Fabrication of multifunctional hybrid nanoparticles for enhancement of neuronal differentiation and specific molecule detection

신경 분화 촉진과 특정 분자 검출을 위한
다기능성 복합 나노 입자 제조

2014年 8月

서울大學校 大學院

化學生物工學部

金 昭 鎭

Fabrication of multifunctional hybrid nanoparticles for enhancement of neuronal differentiation and specific molecule detection

by

Sojin Kim

Submitted to the Graduate School of Seoul National University

in Partial Fulfillment of the Requirements

for the Degree of Doctor of Philosophy

August, 2014

Thesis Adviser: Jyongsik Jang

ABSTRACT

In recent decades, to incorporate diverse components into a single nanoscale system have been a great deal of interest in biomedical fields. These hybrid nanomaterials provide multifunctionality and the extraordinarily enhanced performance than bulk sized material- or single component nanomaterial-based applications. Therefore, with advancing in nanotechnology, many efforts have been also paid to the fabrication of hybrid materials. Nanoparticle is the basic structure to achieve such hybridization. Additionally, nanoparticle is the most internalized structure in the cells compared to other nanostructures. However, there is still lack of literature about fabrication of hybrid nanoparticles for biomedical applications.

The dissertation describes fabricating multifunctional hybrid nanoparticles, evaluating their cytotoxicity, and applying them into neuronal differentiation enhancer and specific molecule detection. This dissertation consists of three parts; silica based, PEDOT based, and PAN based hybrid nanoparticles. Three types of silica based hybrid nanoparticles were suggested by chemical reduction method and sonication mediated etching/redeposition methods. Five different metal oxide (MOx; CeO_2, CuO, Fe_2O_3, MnO_2, and ZnO) decorated SiO_2 NP and HNPs were exhibited element- and

size-dependent toxicity. The p-HNP, Ba-HNP, and Sr-HNPs were applied as neuronal differentiation enhancer, and further modified as encapsulating agent for nerve growth factor. Nerve growth factor encapsulating Sr-HNPs were exceptionally efficient for promoting neuronal differentiation.

PEDOT nanoparticles were fabricated by oxidation polymerization in reverse microemulsion, and used as substrate. The MnO_2 was decorated on the PEDOT nanoparticles by redox deposition, and the hybrid nanoparticles successfully enhanced the neuronal differentiation and detected the catecholamines released from the living cells.

APAN nanoparticles were synthesized by sonication mediated emulsion polymerization and modified with amidine group by pinner method. The fluorescent APAN NPs with biocompatibility provide a new direction for the development of highly sensitive and selective sensors for intracellular Cu^{2+} in living cells. Then, AuNC were decorated on the APAN nanoparticles, which exhibits dual emission property. This fluorescence behavior was highly selective for hROS, and change in dual emission wavelengths results in the enhanced sensitivity and resolution for ratiometric detection. They could provide both efficient cell imaging agents as well as

hROS detection probe *in vitro* with low toxicity.

This dissertation provides the possibility of various approaches for the preparation of multifunctional hybrid nanoparticles and their biomedical applications. The hybrid nanoparticles presented in the dissertation could be applied into biomedical fields such as neuronal differentiation enhancer, catecholamine sensor, and fluorescence sensing probe. Each hybrid nanoparticle are deliberately designed and customized for superior performance in specific applications. This study may provide understanding of fabricating various hybrid nanoparticles with multifunctionality and application of hybrid nanoparticles to biomedical application.

KEYWORDS: Hybrid nanoparticle; Multifunctionality; Cytotoxicity; Neuronal differentiation; Catecholamine sensor; Fluorescence sensor

STUDENT NUMBER: 2009–20981

List of Abbreviations

AOT : sodium bis(2-ethylhexyl) sulfosuccinate

APAN : amidine-PAN

ATP : adenosine triphosphate

Au-APAN : gold nanocluster decorated APAN

AuNC : gold nanocluster

aV : annexin V

BET : Brunauer-Emmett-Teller

BJH : Barrett–Joyner–Halenda

BSA : bovine serum albumin

CSNP : silica/titania core/shell nanoparticle

CV : cyclic voltamogram

DCF-DA : 2´,7´- dichlorodihydrofluorescein diacetate

DMT1 : divalent metal transporter 1

EDX : energy-dispersive X-ray spectroscopy

ELS : electrophoretic light scattering

FACS : flow cytometry

FBS : fetal bovine serum

FE–SEM : field emission scanning electron microscope

FITC : fluorescein isothiocyanate

FITC-HNPs : fluorescein isothiocyanate cojugated HNPs

FRET : fluorescence resonance energy transfer

FT-IR : fourier transform-infrared

HBSS : Hank's buffered salt solution

HEPES : 4-(2-hydroxyethyl)-1-piperazineethanesulfonic acid

HNP : silica/titania hollow nanoparticle

HRTEM : high resolution-transmission electron microscopy

HS : horse serum

ICP : inductively coupled plasma

MMP : mitochondrial membrane potential

MOx : metal oxide

NGF : nerve growth factor

NP : nanoparticle

PAN : polyacrylonitrile

PBS : phosphate buffered saline

PEDOT : poly(3,4-ethylenedioxythiophene)

PI : propidium iodide

PL : photoluminescent

ROS : reactive oxygen species

STEM : scanning transmission electron microscopy

TEM : transmission electron microscopy

XPS : X-ray photoelectron spectroscopy

XRD : X-ray diffraction

List of Figures

for 24 h, followed by addition of 1 μg mL^{-1} of PMA for 0, 2, and 12 h. The PMA plays a role as ROS inducer in cells. Among graphs, free of NPs in the cells was used as a negative control. (b) XPS spectrum of Ce-SiO$_2$ NP. Two sets of spin-orbital multiplets, corresponding to the 3d$_{3/2}$ and 3d$_{5/2}$, were labeled as u and v, respectively.

Figure 13. Effect of MOx-SiO$_2$ NPs on MMP. Cells were treated with the MOx-SiO$_2$ NPs for 24 h (25 μg mL^{-1}). Free of NPs in the cells was used as a control (Ctrl). The red and blue area means Group I and Group III, respectively.

Figure 14. Cell death mechanism determined by fluorescence images and flow cytometric analysis. Unstained and dual-stained cells were presented viable and late apoptotic cells. The green/red fluorescent labels represent as early apoptotic/necrotic cells (scale: 20 μm). Among the experiments, cells were treated with the MOx-SiO$_2$ NPs for 24 h (25 μg mL^{-1}). Free of NPs in the cells was used as a control (Ctrl). The red and blue area means Group I and Group III,

respectively.

(25 μg mL^{-1}). Green (aV) means apoptosis, red (PI) means necrosis. Scale bars: 15 μm.

Immunofluorescent images of cells treated with 0.1% BSA and 25 µg mL^{-1} NGF-HNPs. The cells were stained with β-tubulin (class III; neural specific marker; green) and DAPI (nucleus; blue).

UV light (365 nm). (b) Fluorescence spectra of APAN NPs under different excitation wavelength.

Figure 58. (a) Selectivity of APAN NPs (10 μg mL^{-1}) for different metal ions (10 μM). Inset represents the possible sensing mechanism of APAN NP for Cu^{2+}. (b) Fluorescence emission spectra of APAN NPs in the presence of Cu^{2+} at different concentrations (0-100 μM). (c) Based on the Figure 4b, the relationship between emission fluorescence intensity of APAN NPs and concentrations of Cu^{2+} was calculated. I and I$_0$ are the emission fluorescence intensities of the APAN NPs at 290 nm in the presence and absence of Cu^{2+}, respectively. Inset is the linear region. (d) Representative fluorescence spectra with the addition of Cu^{2+} and EDTA in the quenching recovering. The inset shows the fluorescence photograph of (a) APAN NPs, (b) APAN NPs + Cu^{2+}, and (c) APAN NPs + Cu^{2+}+ EDTA under UV light (365 nm).

Figure 59. Live cell differential interference and fluorescence images of the SK-BR-3 cells. The cells were treated with (a) APAN NPs, (b)

presence of hydroxyl radicals at different concentrations (0-100 nM). (f) The relationship between emission fluorescence intensity of Au-APAN NPs and concentrations of hROS (superoxide, hypochlorite, and hydroxyl radical) was calculated. Insets: photograph taken with UV lamp irradiation (365 nm).

RAW264.7 cells based on the AuNCs (red fluorescence). The concentration of Au-APAN NP was 10 and 25 μg mL^{-1} in fluorescence images and flow cytometry analysis, respectively. Experimental conditions were below. Negative control: Non-Au-APAN NP treated cells. Au-APAN: cells were incubated with Au-APAN NPs for 24 h. Au-APAN NP+PMA: Cells treated with Au-APAN NPs for 24 h, followed by 1 μg mL^{-1} PMA for 2 h. Au-APAN NP+PMA+TEMPO: Cells treated with Au-APAN NPs for 24 h, followed by 1 μg mL^{-1} PMA for 2 h. Au-APAN NP+PMA+Uric acid/DMSO: Cells treated with Au-APAN NPs for 24 h, followed by 1 μg mL^{-1} PMA for 2 h. Then, 250 μM UA and 0.5% DMSO were inserted for additional 15 min.

Figure 70. Viability of and ROS production by RAW264.7 incubated with Au-APAN NPs for 24 h.

List of Tables

Table of Contents

1. INTRODUCTION

1.1. Background

1.1.1. Nanomaterials

Nanomaterials can be defined by their size in the range of 1-100 nm (in at least one dimension). Recently, nanomaterials based on metal, inorganic, and polymers have been extensively investigated in various fields such as physics, chemistry, and biology. They exhibited unique quantum phenomena, atomic physics, and enhanced performances compared to bulk materials (over the micron size) due to their quantum confinement effect and increased surface-to-volume ratio. These nanomaterials can be roughly categorized into two groups by their origins; organic (any molecule containing carbon originated from animate thing) and inorganic nanomaterials. A classified table for these nanomaterials was shown in Figure 1. In this research, I focused on the polymer (polyacrylonitrile and poly(3,4-ethylenedioxythiophene)), mineral based (metal and metal oxide), and their hybrid nanomaterials.

The nanomaterials have many different types of structure such as a sphere (particle), rod, fiber, tube, sheet, and so on. Interest in nanomaterials with diverse structure has been steadily growing because their fascinating properties and potential applications stem from their nanoscale dimension and structure.[1] Among the various structures, I concentrated on the particle

structure. Nanoparticles are zero-dimensional materials, and can be used as building block for other structure including fiber even 2-D sheet structure. For these reasons, nanoparticles are considered as most basic structure among the various structures. As perspective for biological application, the internalization efficiency of the nanomaterials increases as aspect ratio getting shorter and shorter, that is the spherical shape is most effective structure for internalization into the cell or human body.[2] In addition, nanoparticle structure also have largest surface to volume ration compared to other structure such as rod or fiber. Collectively, the particle structured nanomaterials are most suitable form for the biomedical applications.
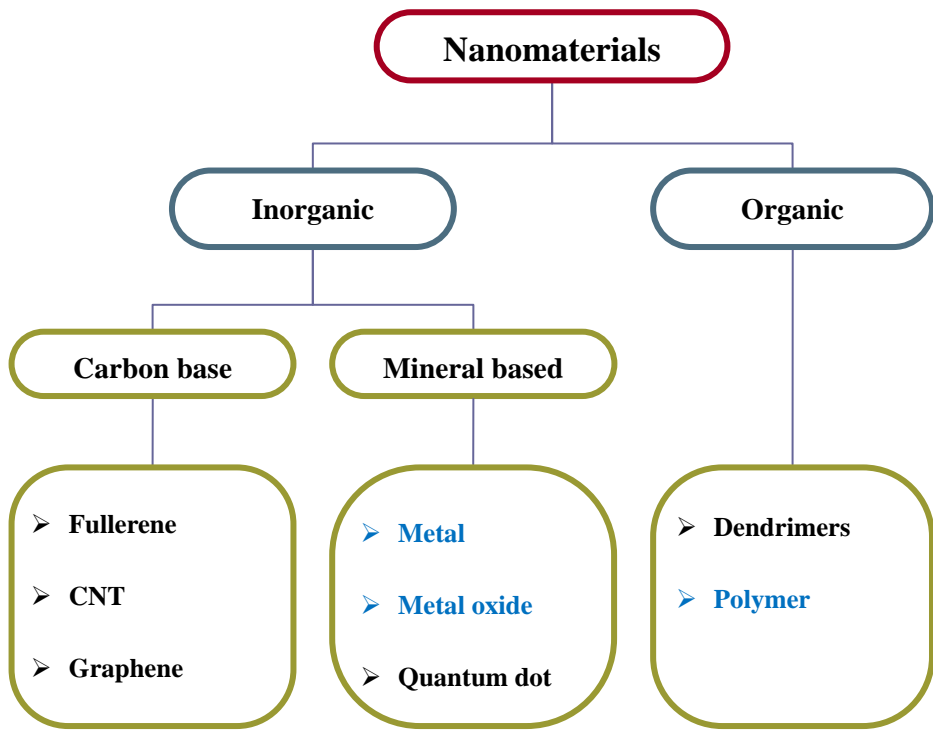
Figure 1. Classification of nanomaterials. The blue color means the materials that are used in this paper.

1.1.1.1 Synthesis of polymer nanoparticles

The advance of polymer particles has been a rapidly developing field of research owing to several advantages, including easy modifying surfaces with multiple ligands, excellent stability, and price competitiveness. Polymer nanoparticles are prepared using methods including solvent evaporation, spontaneous emulsification, solvent diffusion, salting out/emulsification-diffusion, and use of supercritical CO_2, among others.[3] These methods can be classified into three groups according to the template type; hard template method, soft template method, and template free method (Figure 2). In case of hard template method, top-down particle or other inorganic nanoparticles such as silica nanoparticles are mainly used as substrate and the polymer nanoparticles are fabricated as replica of the substrate particle. Their size and shape are dependent on those of substrate particles.

Soft template synthesis, which involves the introduction of precursor materials within channels of templates, has been extensively studied to fabricate polymer nanoparticles. They use various sized micelle as template instead of top-down particle or other inorganic nanoparticles. Microemulsion polymerization has become one of the most attractive methodologies for fabricating polymer nanoparticles because microemulsion provides advantages such as thermodynamic stability, the use of nanometer-sized micelles as nanoreactors, and a wide selection of surfactants. [4] In case of conducting

polymer nanoparticles including polypyrrole, polyaniline, poly(3,4-ethylenedioxythiophene), they are usually fabricated by chemical oxidation polymerization under microemulsion conditions.[5] In a broad sense, emulsion polymerization is also included in the soft- template method because the radical polymerization of monomers only occurs in the micelle. Polyacrylonitrile nanoparticles are one of the examples for emulsion polymerization.[6]

Compared to hard or soft template methods, template-free method provides a facile and practical route to produce pure and high quality nanoparticles. Template-free method encompasses various methods such as electrochemical synthesis, interfacial polymerization, and dispersion polymerization. For hybrid nanoparticles, electrohydrodynamic cojetting method is very useful. This technique has been used to prepare biphasic and triphasic nanoparticles that are able to encapsulate agents of various diverse physical-chemical properties.[7]

In this study, soft template was mainly used for preparing polymer nanoparticles, and further to the soft template method, two major synthetic methods were also introduced for polymer nanoparticles: chemical oxidation polymerization and ultrasonic-induced emulsion polymerization.
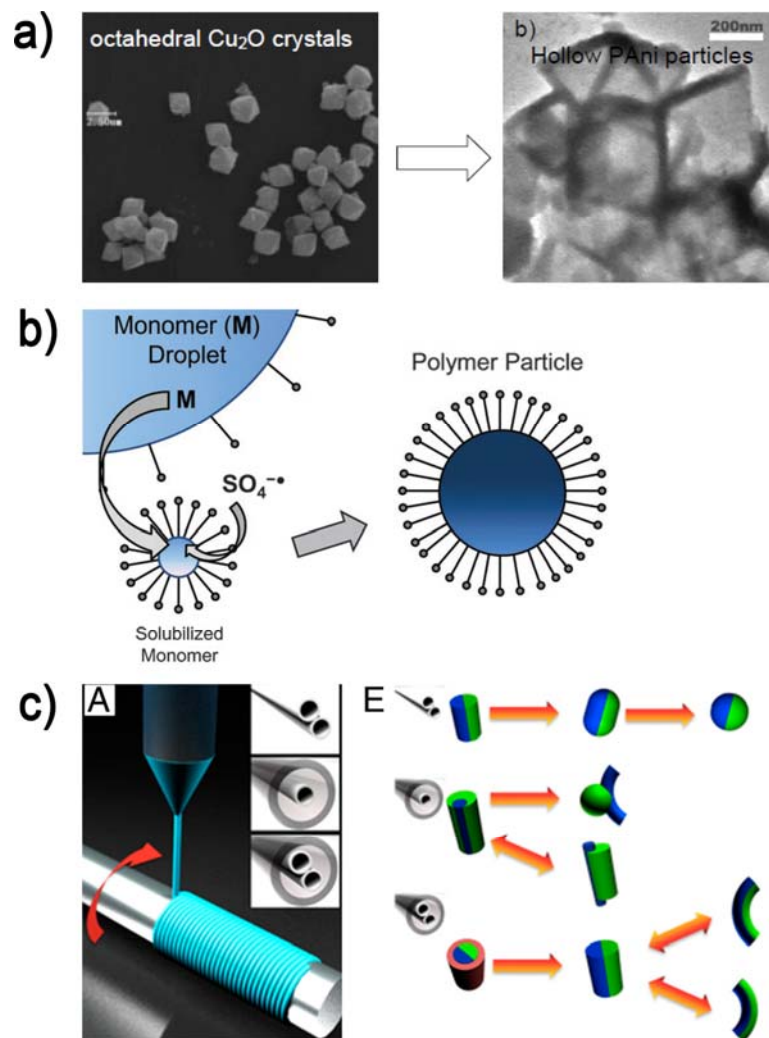
Figure 2. Various synthetic methods of polymer nanoparticles. (a) Hard template method, (b) soft template method, (c) template free method (electrohydrodynamic cojetting method). [7-9]

1.1.1.2 Synthesis of inorganic nanoparticles

Inorganic nanoparticles are often classified according to their chemical composition, and the simplest division is carbon based (*e.g.* fullerene, carbon nanotube, and graphene) and mineral based nanoparticles (*e.g.* metal, metal oxide, and quantum dot). In this research, only metal and metal oxide NPs was investigated. Various chemical methods were employed for the synthesis of these nanoparticles; For example, microemulsion system, thermal decomposition, hydrothermal and solvothermal synthesis, sol–gel method, phase-transfer method, use of the liquid–liquid interface, chemical reduction method (Figure 3).[10] Among various synthetic methods, chemical reduction method and sol–gel method were mainly used for fabricating metal and metal oxide nanomaterials.

In general, the sol–gel method is used for the synthesis of chemical metal oxide nanoparticles, especially for SiO_2 and TiO_2 nanoparticles. The sol-gel process consists of a series of distinct steps. At first, the metal precursors were hydrolyzed and condensed, resulting gelation of the metal precursors. Further condensation and polymerization makes metal oxide networks with three-dimensional structure. The sol–gel process can be either in aqueous or non-aqueous medium.[11] In the aqueous condition, oxygen source for the formation of the oxide is originated from the water. In case of the nonaqueous condition, oxygen is provided by a solvent such as ethers, alcohols, ketones, or

aldehydes or by an organic constituent of the precursor (*e.g.* alkoxides or acetylacetonates).[10] Controlling nanoparticle size and the structure is possible by control of pH. Commonly, base-catalyzed hydrolysis is preferred for the particles, though not always necessary.[11] Controlling the hydrolysis equilibrium can be another factor for directing the structure of the particles.

Another fabricating method for the inorganic nanoparticles is chemical reduction method. Chemical reduction method is widely used for synthesis of metal and metal oxide nanoparticles. In case of metal nanoparticles, reducing agents are necessary. The most common forms of reducing agents are ABH_4 (A= alkali metal), hydrazine hydrate ($N_2H_4 \bullet H_2O$), and hydrazine dihydrochloride ($N_2H_4 \bullet HCl$).[11] For reduction of any metal ion, the reduction potential of the metal is more positive than that of reducing agents at RT. The synthesis of metal oxide nanoparticles is generally less straightforward than the metal nanoparticles. Reactions for the synthesis of metal oxide can be classified into two groups: one is those that produce metal oxide directly, the other is those that produce what is best termed a precursor that must be subjected to further processing (drying, calcination, etc.). In either case, like metal nanoparticles, monodispersed metal oxide mostly requires a capping agent or other stabilizer to prevent aggregations. However, in the group that is needed further processing, some agglomeration will be unescapable.
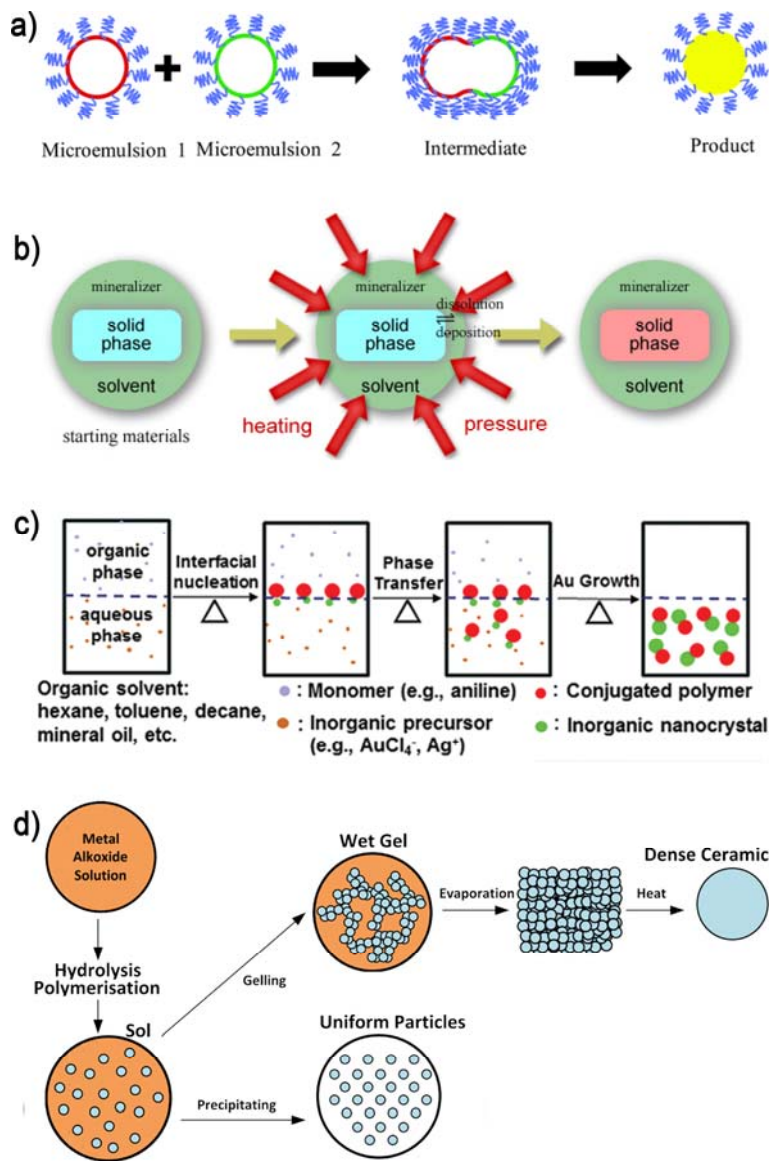
Figure 3. Various synthetic methods of metal and metal oxide nanoparticles. (a) microemulsion system, (b) hydrothermal synthesis, (c) use of the liquid–liquid interface, and (d) sol–gel method.[10, 12, 13]

1.1.1.3. Synthetic strategies of multifunctional hybrid nanoparticles

In general, there are several strategies for incorporating diverse components into a single nanoparticle. Focused on multifunctionality, some synthetic strategies of hybrid nanoparticles are represent in this study.

The easiest way to give multifunctionality on the nanoparticles and make hybrid nanoparticle is addition of small molecules on the nanoparticle (nanoparticle–small molecule assembly).[3] Representative small molecules are fluorescent dye, radioisotopes, drug molecules, siRNA/DNA, and peptides. Depending on the functional requirements, these small molecules are loaded at the center or the surface of nanoparticles. Nanoparticle–small molecule assembly can be prepared by physical adsorption or chemical conjugation. In case of siRNA or DNA, they are often adsorbed to nanoparticles *via* electrostatic interactions owing to their negative charge and small size. However, most small molecules prefer to be conjugated on the nanoparticle surface directly.[3]

Another synthetic method for hybrid nanoparticle is combining two different nanoparticles into one system (nanoparticle-nanoparticle assembly). [3] A direct method for combining two different nanoparticles is seed-mediated growth. One type of nanoparticle is fabricated, which is used as seeds for the other nanoparticle. In general, hybrid nanoparticles between metal

nanoparticles are used this method. Dumbbell-like gold-iron oxide nanoparticles is one the example.[14] In case of polymer nanoparticles, electrohydrodynamic cojetting belongs to this method.

The other method for combining two different nanoparticles is assembly between ready-made nanoparticles. To bridge two different nanoparticles, silica layer coating or covalent bond has widely been used. In case of silica layer, many metal oxides can grow on silica surfaces, including the surface of silica nanoparticles or other nanoparticles with a silica coating, therefore silica layer used as a linker for two nanoparticles.[3] Covalent bond is representative method for merging two nanoparticles; chemical groups such as -SH, -OH, -COOH are usually located on the one nanoparticle and -NH$_2$ exist on the other nanoparticle. This approach had wide applicability to all sorts of the nanoparticles such as polymer or metal, even metal oxide.

1.1.2. Hybrid nanoparticles for biomedical application

1.1.2.1. Cytotoxicity evaluation

Nanomaterials have attracted great attention because of their superior bioactivity by exponential increase in surface area and enhanced physicochemical properties with decreasing diameters.[15] However, nanomaterials can induce oxidative stress and an inflammatory response in biological systems, resulting in harmful effects.[16] The precise mechanism or reason of their toxicity is still beneath the veil, although intensive research has been conducted. The factors affecting cytotoxicity of the nanomaterials can be roughly categorized into two groups; one is physical variables such as size, shape, and surface charge (Figure 4). The other is chemical variables such as element. In this research, I studies size and element effect, as representatives for the each variable, on the cytotoxicity of the nanomaterials using silica based hybrid nanoparticles.

In view of the size effect, size of nanoparticles could affect cellular uptake rate and mechanism.[17] However, there are limited researches concerning size-dependent nanotoxicity on biological systems. The nanoparticles of different diameters should be evaluated systematically from a cytotoxic viewpoint. For the evaluation of the size-dependent nanotoxicity, controlled size and uniform shape of nanoparticles are required.

From an element dependent cytotoxicity standpoint, reports on element-based adverse health effect of nanomaterials have raised various controversial toxicological issues. For example, CeO_2 nanoparticles are known as antioxidants owing to the redox cycles between the Ce^{3+} and Ce^{4+} oxidation states.[18] However, other studies have indicated that CeO_2 nanoparticles induce apoptosis and autophagy in human monocytes.[19] Therefore, precise research is needed with nanomaterials produced by controlled synthesis. To address this issue, a library of nanomaterials with the same physical properties, but a wide range of elements, is required.

Comparing the cellular response of a wide range of nanomaterials has posed major obstacles due to the difficulty in fabricating nanostructures with similar physicochemical conditions (*e.g.*, size, shape). In order to prepare the nanoparticles with controlled physical properties, we chose decoration method on silicon dioxide nanoparticles. SiO_2 nanoparticles were used as a supporting material to be decorated and control materials to be compared with other elements. We selected widely used typical transition metals elements (Mn, Fe, Cu, and Zn) and representative antioxidant elements (Ce) to form metal oxides on SiO_2 nanoparticles. The transition metal nanomaterials have been widely researched in metal oxide form for biomedical application, such as MRI agent, anticancer agent, and biosensor.[20-22] However, metal oxide nanomaterials

13

may be responsible for oxygen radical generation and oxidative stress, which are principal injury mechanisms through which metal oxide nanomaterials may induce adverse health effects.[23] In case of Ce and Se, they exhibit antioxidant effects as form of CeO_2 and Se, respectively. However, there are conflicting reports regarding the cellular effects of them.[24, 25] Therefore, accurate and controlled toxicity tests are essential for the safe use of nanomaterials. The above-mentioned elements were necessary for accurate element-dependent cytotoxicity assessments and comparisons.
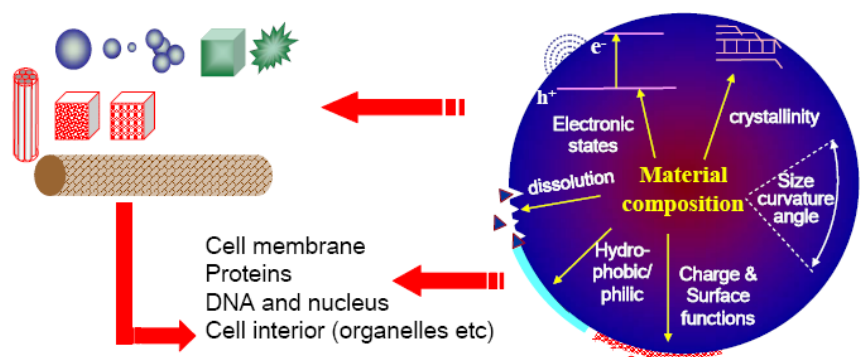
Figure 4. Elements of nanomaterials that can affect cellular system such as shapes, crystallinity, electronic states, dissolution, and charge or surface functionality

1.1.2.2 Neuronal differentiation enhancer

In general, the nervous system can be divided into two groups: the central nervous system and the peripheral nervous system. They have two different repair processes after damage (Figure 5). In case of the peripheral nervous system, the damaged axons usually regenerate and recover *via* proliferating Schwann cells, phagocytosing myelin by macrophages or monocytes, forming bands of Bünger by the bundling of Schwann cells and sprouting axons in the distal segment. [26] Unlike the peripheral nervous system, in the central nervous system, it is difficult to re-extend axons to recover their functions due to the absence of Schwann cells. Additionally, the glial tissue typically formed around the wounded axon because of the astrocytes, meningeal cells, and oligodendrocytes, which prevents proximal axon growth and inhibit neuron regeneration. Therefore, the wounded central nervous system may induce severe functional damages and are hard to repair than other injuries.

Although remarkable progress and the unexploited potential for therapy of neural disease and injury have been reported, integration with, and reconstruction of, native neural circuitry are still required. The preparation of artificial nerve regeneration represents an alternative strategy for the restoration of nerve function after injury.[27] However, the tissue engineering approach requires understanding of neurite-like processes to reproduce the complex architecture of neuronal networks. Therefore, the investigation of

neuron development and outgrowth has received considerable attention from biomedical engineers in past decades.[28]

Neuronal differentiation properties are strongly affected by the morphology and composition of the extracellular matrix and by the complex interactions between external physical and chemical stimuli.[29] Particularly, it has been reported that divalent metal cations, including Mn^{2+}, Mg^{2+}, Ni^{2+}, and Cu^{2+}, can enhance cell adhesion and neurite outgrowth. For example, Mn^{2+} was immobilized with the extracellular matrix, which is involved in neuronal differentiation, by activating cell adhesion molecules and controlling mechanical tension.[30] Moreover, Mn^{2+}, like nerve growth factor (NGF), promoted the differentiation of neurons through inhibition of the dividing ability of astrocytes.[31] Mn–induced cell differentiation is dependent on its interaction with the cell–surface integrin receptors and basement membrane proteins, fibronectin, and vitronectin.[31, 32]

Such as divalent metal cations, alkaline earth elements also received attention in neuronal differentiation researches. Barium (Ba) and strontium (Sr), alkaline earth elements, have been   widely used clinically for the treatment of osteoporosis.[33] Calcium hydroxyapatite in bones can be substituted by other competing divalent ions, such as Sr and Ba ions from the surrounding matrix *in vivo*.[33] For implantable use, the Ba- and Sr-doped materials showed better

mechanical performance than calcium materials.[34-37] Therefore, intensive research has focused on developing Ba- and Sr-doped implant materials for not only constant release of the Ba and Sr ions but also enhanced mechanical properties.[34-38] Recently, Ba and Sr ions were reported to evoke release of dopamine from rat pheochromocytoma cells (PC 12) used as model cells for neuronal differentiation, indicating that Ba- and Sr-doped materials affect the neural differentiation.[39] However, relatively little attention has been given to the effects of Ba and Sr-doped materials on neural differentiation.

Nanomaterials can interact with biological systems at fundamental, molecular levels with high specificity.[2] By taking advantage of this unique molecular specificity, nanomaterials can interact with, stimulate, and respond to target cells and tissues in controlled ways, while minimizing undesirable effects. The application of nanomaterials in neuroscience is stuck in the early stages of development, due to the complexities associated with interacting with neural cells and the mammalian nervous system. However, nanotechnology for neuroscience research is emerging because of its unique physicochemical properties (Figure 6).[40, 41] Specifically, neuronal adhesion and growth, interfacing neurons at the molecular level, and functional neural regeneration are of interest to nanotechnology researchers. Therefore, a necessity exists for understanding how nanomaterials work to enhance neural regeneration.
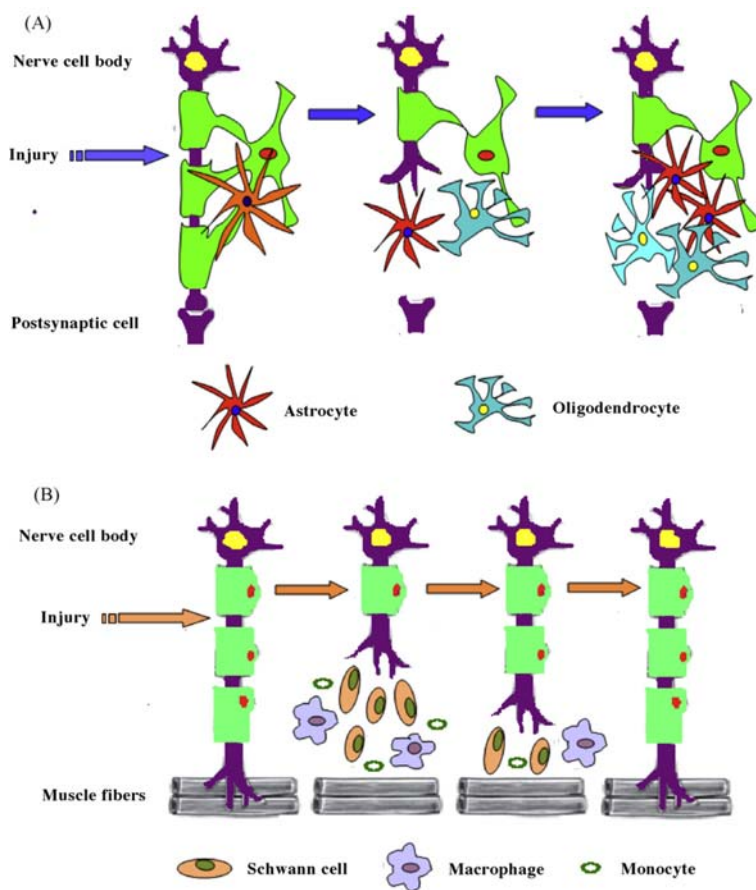
Figure 5. Schematic graphs of injured nerve regeneration in the central and peripheral nervous systems. (a) Central nervous system recovery process with glial scar tissue formation and (b) peripheral nervous system recovery process involving the activity of Schwann cells, macrophages, and monocytes [26].
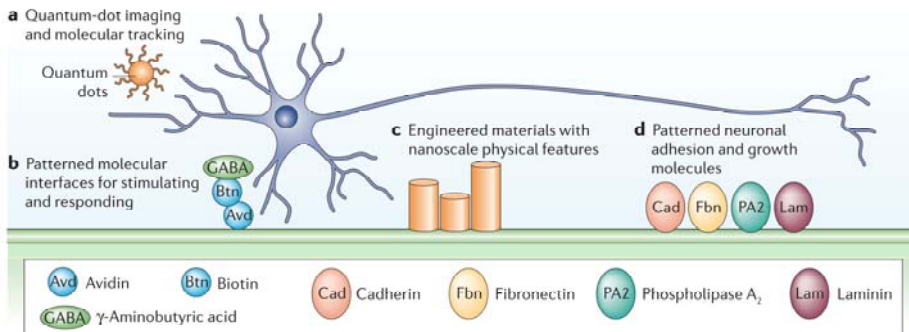
Figure 6. Applications of nanotechnologies in basic neuroscience. Nanomaterials and devices that interact with neurons at the molecular level can be used to influence and respond to cellular events. In all cases, these engineered technologies allow controlled interactions at cellular and subcellular scales. (a) Chemically functionalized fluorescent quantum dot nanocrystals used to visualize ligand–target interactions. (b) Surfaces modified with neurotransmitter ligands to induce controlled signaling. (c) Engineered materials with nanoscale physical features that produce ultrastructural morphological changes. (d) Surfaces and materials functionalized with different neuronal-specific effector molecules, such as cadherin and laminin, to induce controlled cellular adhesion and growth. [41]

1.1.2.3 Catecholamine sensor

Chemical communication between cells is accomplished by the release of specific biochemical molecules *via* an exocytosis; especially, neurotransmitters released from neurons.[42] Among the neurotransmitters, catecholamine (*e.g.*, dopamine, epinephrine, and norepinephrine) are major neurotransmitters.[43] Real-time monitoring of catecholamine is received attention for revealing the mechanisms and functions of chemical communications between cells. Among the various methods, electrochemical techniques based on ultramicroelectrodes have mainly used. They can detect catecholamine at the single-cell or single-vesicle level, which has several advantages; improved sensitivity, monitoring on the nanosecond scale, and the low iR drop.[44] The electrophysiological single cell recordings provide quantitative and kinetic information about exocytosis. However, this technique requires high experimental skills. Moreover, in most cases, ultramicroelectrodes should invade into the single cells for capturing the signal. Therefore, non-invasive sensor system has received much attention as alternatives for electrophysiological single cell recordings method.

1.1.2.4 Fluorescence sensor

In nanoscience, nanomaterials with fluorescence property have been of great interest in biomedical applications, such as bioimaging, drug carriers, and corresponding disease therapy.[18] Quantum dots is representative imaging agent because of wideband excitation, narrow emission, and high quantum yield.[19] However, they also have several limitations; hard to surface functionalization and high toxicity. Therefore, various alternatives for quantum dots such as metal nanocluster and polymer based fluorescence nanoparticles have been developed.

Metal nanocluster, which consists of several to tens of atoms, generates strong photoluminescence due to quantum confinement effect. Moreover, they have resistance to photobleaching like quantum dots, making metal nanocluster as one of the alternatives for quantum dots. Among the various elements, gold nanocluster is actively discussed and studied today because of unique bio-compatibility and easy to surface modification with sulfur-Au interaction.[45, 46] These advantages make gold nanocluster an attractive fluorescent agent for biological applications. However, the responsiveness of gold nanocluster to biological signaling molecules and their direct use as sensors for bioimaging remain largely unexplored.[46]

Polymer based fluorescence nanoparticles also have attention as much as

that of metal nanocluster. Polymer nanoparticles have several advantages in bioimaging over inorganic based approaches, including diverse functionality, facile surface modification and low toxicity.[23] Above all, cost effectiveness is the biggest strength for polymer nanoparticles. However, there has been relatively little research on fluorescent polymer particles because of the difficulty of fabricating precisely controlled nanostructures.[47]

As bio-analyte, copper ion and reactive oxygen species (ROS) are mainly investigated *in vitro*. Copper is an essential nutrient for all known life forms. It is used as a cofactor in nearly 20 enzymes and has multiple functions ranging from bone formation to cellular respiration.[48] However, free Cu^{2+} is known to cause toxicity to cells because it produces hydroxyl radicals.[48] The increase copper ion may induce adverse health effects such as gastrointestinal disturbance and liver or kidney damage, even Alzheimer or Parkinson disease.[49] Considering the double-edged characteristics of copper ion for human health, on-site and real-time monitoring of intracellular copper ions is important. However, in case of conventional dyes, detection of copper ion is still challenging due to its unselective paramagnetic quenching effects on common fluorophores.[49] Hence, recognition moieties should be added on fluorescence agents.

ROS, generated in metabolic processes, are play crucial roles in regulating

a wide range of physiological functions. They consist of superoxide (O_2^-),
singlet oxygen (O_2^1), hydrogen peroxide (H_2O_2), hydroxyl radical (•OH), and
hypochlorite (OCl^-) (Figure 7). The O_2^- is a one-electron reduction product of
the triplet dioxygen molecule, and first molecules that stand in a ROS
generation process.[50] Generally, O_2^- is considered as a rather unreactive
radical species.[51] However, the excess production of O_2^- can form highly
oxidizing species, causing cellular dysfunction through loss of protein function,
carbohydrate oxidation, DNA cleavage, and lipid peroxidation.[50] Among
various ROS, •OH and OCl^- are considered to be highly ROS (hROS) because
of their strong oxidant properties that can directly oxidize nucleic acids,
proteins, and lipids, leading to potentially serious damage in living cells.[46]
Therefore, probes for visualizing ROS are useful for explaining the biological
roles of ROS, and provide the capability for using medical diagnostics and
research tools.
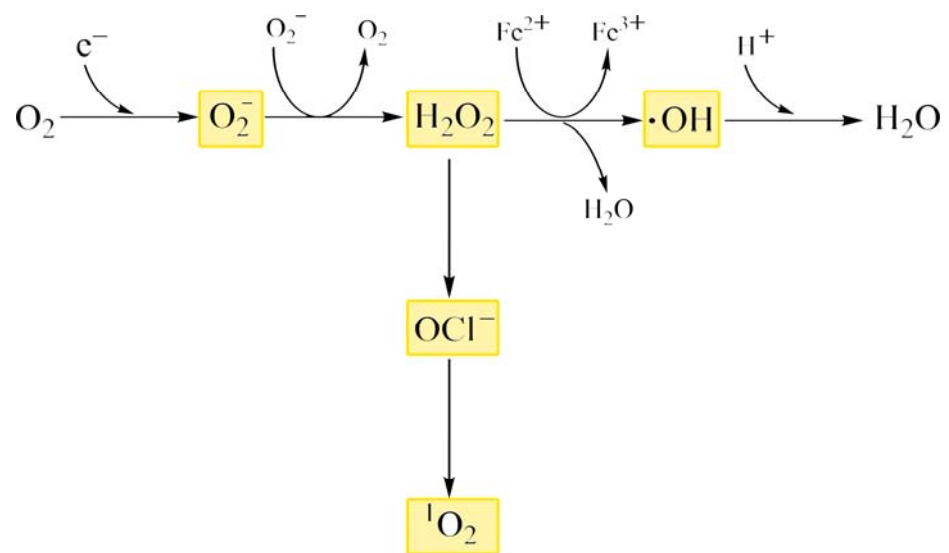
Figure 7. ROS generation process. Yellow boxes indicated ROS.

1.2. Objectives and Outline of the Study

1.2.1. Objectives

The aim of this dissertation provides fabricating multifunctional hybrid nanoparticles, evaluating their cytotoxicity, and applying them into enhancement of neuronal differentiation and specific molecule detection. In particular, three types of silica based hybrid nanoparticles are fabricated by chemical reduction, sol-gel, and sonication mediated etching/redeposition methods. They are employed for nanotoxicological assessments and neuronal differentiation enhancer. In case of polymer based hybrid nanoparticles, poly(3,4-ethylenedioxythiophene) (PEDOT) and polyacrylonitrile (PAN) nanoparticles were respectively fabricated by chemical oxidation polymerization and sonication medicated emulsion polymerization, and used as substrate. MnO_2 are decorated on the PEDOT, and then applied into both neuronal differentiation enhancer and transducer for catecholamine sensor. Gold nanoclusters are also decorated on the PAN nanoparticles for fluorescence probe for monitoring of intracellular copper ion and highly reactive oxygen species (hROS). Each hybrid nanoparticle is deliberately designed and customized for superior performance in specific applications.

1.2.2. Outline

This dissertation could be divided into three sections according to the substrate; silica based hybrid nanoparticles, PEDOT based hybrid nanoparticles, and PAN based hybrid nanoparticles. In the silica based hybrid nanoparticle part, five different metal oxides (CeO_2, CuO, Fe_2O_3, MnO_2, and ZnO) were decorated on the SiO_2 nanoparticles by chemical reduction methods for element-dependent cytotoxicity evaluation. And then, the SiO_2/TiO_2 hollow nanoparticles with five different diameters were fabricated using sol-gel method and sonication mediated etching/redeposition method for size-dependent cytotoxicity evaluation. At last, barium and strontium doped SiO_2/TiO_2 hollow nanoparticles were fabricated using above mentioned sol-gel method and sonication mediated etching/redeposition method. They were applied as neuronal differentiation enhancer.

The second part is PEDOT based hybrid nanoparticles. PEDOT nanoparticles were fabricated by oxidation polymerization in reverse microemulsion. The MnO_2 was decorated on the PEDOT nanoparticles by redox deposition, and the hybrid nanoparticles were dual-applied as neuronal differentiation enhancer and transducer for the catecholamine sensor.

The last section is PAN based hybrid nanoparticles. At first, the PAN nanoparticles, fabricated by sonication mediated emulsion polymerization,

were modified with amidine group. These amidine-PAN nanoparticles were used as fluorescence probe for detecting intracellular copper ion. And then, orange fluorescent gold nanocluster, fabricated by chemical reduction method, was decorated on the amidine-PAN nanoparticles. The Au decorated amidine-PAN nanoparticles were further applied as dual emission fluorescence probe for monitoring intracellular highly reactive oxygen species.

In the viewpoint of abovementioned topics, this dissertation involves the following subtopics;

I.   Metal oxide decorated SiO_2 nanoparticles for cytotoxicity evaluation

II. SiO_2/TiO_2 hollow nanoparticles for cytotoxicity evaluation

III. Ba/Sr doped SiO_2/TiO_2 hollow nanoparticles for neuronal differentiation

IV. MnO_2 decorated PEDOT particles for neuronal differentiation and catecholamine detection

IV. Amidine-PAN nanoparticles for Cu^{2+} detection

V.   Au decorated amidine-PAN nanoparticles for intracellular highly reactive oxygen species detection

2. EXPERIMENTAL DETAILS

2.1. SiO₂ based hybrid nanoparticles

2.1.1. Metal oxide decorated SiO₂ nanoparticles

2.1.1.1 Fabrication of metal oxide decorated SiO₂ nanoparticles

SiO₂ nanoparticles (SiO₂ NPs) were prepared by Stöber method.[52] First, 2.3 mL of tetraethyl orthosilicate (Aldrich, St. Louis, MO) was added to the mixture of ethanol (60.0 mL), ammonium hydroxide solution (3.0 mL), and water (1.0 mL). The sol-gel reaction was performed for 6 h at 55 °C. To capture the precursor ions on the surface, 160 mg of SiO₂ NPs were treated with equivalent weight of N-[3-(trimethoxysilyl)-propyl] ethylenediamine (Aldrich, St. Louis, MO) in 1:1 ethanol-water mixture for 12 h. Fabricating NPs (amine-SiO₂ NPs) were washed several times. Subsequently, 5 mg of amine-SiO₂ NPs was added to the precursor solutions with stirring for 12 h at RT. To decorate equivalent weight percentage of the metal oxides (MOx) on the SiO₂ NPs, the detailed experimental conditions were slightly different between ND types due to their properties and summarized in Table 1.

The metal ions (iron, zinc, copper, and cerium ions) were dissolved in ethanol and coordinated with the diamine species on the surface of the SiO₂ NPs. NaOH was introduced dropwise into precursor solutions, and all reactions were carried out for 12 h at RT. In case of SeO₂, they formed H_2SeO_3 solutions

after dissolving in distilled water. The SeO_3^{2-} ions were decorated on the surface of the amine-SiO_2 NP by charge-charge interactions, and reduced by ascorbic acid for 6 h at RT. In case of the MnO_2 NDs, the MnO_4^- ions, located on the surface of the SiO_2 NPs by charge-charge interactions, were reduced by formamide for 8 h at 40 °C.

The images and the crystallinity of the NDs were acquired by HRTEM (JEOL JEM-3010) and XRD (M18XHF SRA, MAC Science Co.), respectively. Size distribution and zeta potential of the MOx-SiO_2 NPs were measured by an ELS-8000 instrument (Otsuka Electronics, Japan). The amount of NDs on SiO_2 NPs was investigated using ICP-MS (JP/ICPS-7500, Shimdzu). The oxidation state of CeO_2 was confirmed by XPS (AXIS- His, KRATOS).

Dissolution of metal ions from MOx-SiO_2 NPs was measured in DI water and cell culture medium as a function of a time using ICP-MS. MOx-SiO_2 NPs were suspended in above mentioned solvents with moderate stirring (20 μg mL^{-1}). Each sample (0.5 mL) was extracted as a function of a time by centrifugation at 10000 rpm for 5 min. The supernatant was transferred to a fresh vial, diluted 10 times with appropriate solvents, and analyzed by above mentioned ICP-MS.

Table 1. Detailed experimental conditions for fabricating MOx-SiO$_2$ NPs

	Precursor and their concentration[a]	Catalyst or reducing agent and their concentration[a]
Ce-SiO$_2$	Ce(NO$_3$)$_3$·6H$_2$O, 10 mM	NaOH, 15 mM
Cu-SiO$_2$	CuCl$_2$, 12 mM	NaOH, 24 mM
Fe-SiO$_2$	FeCl$_3$·6H$_2$O, 12 mM	NaOH, 36 mM
Mn-SiO$_2$	KMnO$_4$, 10 mM	HCONH$_2$, 24 mM
Zn-SiO$_2$	ZnCl$_2$, 15 mM	NaOH, 53 mM

[a] All of them were purchased from Aldrich and used without further purification.

2.1.1.2 Cytotoxicity evaluation with element dependence

Mouse macrophage RAW264.7, rat pheochromocytoma PC12, and calf pulmonary artery endothelial CPAE cell lines were used to investigate the effects of MOx-SiO$_2$ NPs. Cells were obtained from American Type Culture Collection (ATCC, Manassas, USA). RAW264.7 were cultured in Dulbecco's modified eagle medium (DMEM) with 10% FBS, 1% penicillin-streptomycin solution. PC12 were grown in RPMI-1640 medium with 10% HS, 5% FBS, and 1% P/S solution. CPAE were maintained in RPMI-1640 with 10% FBS, and 1% P/S solution. Cells were incubated in a 5% CO$_2$ incubator at 37 °C.

For observing internalization of the MOx-SiO$_2$ NPs, cells were placed in sterile culture dishes (Nunc, Thermo Fisher Scientific, USA) for 24 h, and the MOx-SiO$_2$ NPs (25 μg mL^{-1}) were added for another 24 h. After being washed with 0.1 M PBS, cells were prefixed with Karnovsky's fixative (2% paraformaldehyde and 2% glutaraldehyde), postfixed with 1% OsO$_4$ for 2 h, and stained with 0.5% uranyl acetate for overnight. Dehydration was conducted through a gradient ethanol and propylene oxide. Then, they were infiltrated in Spurr's resin and hardened at 70 °C for 1 day. The sections were stained with 2% uranyl acetate and Raynolds' lead citrate, and observed by TEM (JEM1010, JEOL, Tokyo, Japan).

The viability of the MOx-SiO$_2$ NP-treated cells was measured using Cell-

Titer glow luminescent cell viability assay (Promega, Madison, WI, USA). This assay is a homogeneous method of estimating the number of viable cells based on amount of adenosine triphosphate (ATP) in metabolically active cells. For the assay, 1.5×10^4 cells were seeded in white opaque 96-well plates and treated with different concentrations of the MOx-SiO$_2$ NPs (10, 25, 100, 250, and 500 μg mL^{-1}) for 24 h. After incubation, supernatant was removed and following steps were carried out as supplier's instructions. Cell viability was detected by Victor^3 Multilabel Readers (Perkin Elmer, Boston, MA, USA).

In order to measure ROS production and loss of mitochondrial membrane potential (MMP), cells were plated in 6 well plates at a density of 1×10^5 cells mL^{-1} and treated with MOx-SiO$_2$ NPs (10, 25, 100, 250, and 500 μg mL^{-1}) each for 24 h. The cells were washed, trypsinized, and collected in tubes. After being resuspended in 0.1 M HBSS, the cells were incubated with MitoSOX (to measure the mitochondrial superoxide) or H$_2$DCFDA (to measure total cellular H$_2$O$_2$) (Invitrogen, Grand Island, NY, USA) at 5 μM concentration for 15 and 30 min at 37 °C, respectively. In case of MMP, cells were stained with 2.5 μg mL^{-1} JC-1 dye for 30 min at 37 °C. They were analyzed by FACS Aria I (BD Bioscience, USA).

Divalent metal transporter 1 (DMT1) in cells was calculated using flow cytometry. As described above, 1×10^5 cells were treated with MOx-SiO$_2$ NPs

33

($25~\mu\text{g mL}^{-1}$) for 24 h. Being washed with 0.1 M PBS, the cells were fixed with 4% paraformaldehyde for 20 min, permeabilized with 0.1% Triton X-100 for 15 min, and blocked with blocking solution (0.1 M PBS, 10% FBS, and 0.03% 1 M NaN_3) for 30 min. DMT1 antibodies (Santa Cruz, USA) were diluted with blocking buffer and incubated with cells for 1 h. Then, the cells were stained with FITC conjugated secondary antibodies for 1 h and analyzed with flow cytometry (FACS Aria I, BD Bioscience, USA).

As described earlier, cells were seeded and treated with $MOx\text{-}SiO_2$ NPs (10 $\mu\text{g mL}^{-1}$) for 24 h. An annexin (aV)/propidium iodide (PI) double staining (Vybrant apoptosis assay kit, Invitrogen, Grand Island, NY, USA) can visualize the apoptotic/necrotic cells, and were conducted as manufacturer's instructions. Cell images were obtained by Delta Vision RT imaging system (Applied Precision, Issaquah, WA) For quantification of apoptotic cells, $25~\mu\text{g mL}^{-1}$ $MOx\text{-}SiO_2$ NPs treated cells were stained with $MOx\text{-}SiO_2$ NPs, and analyzed using flow cytometry (FACS Aria I, BD Bioscience, USA) at an emission wavelength of 530 nm for aV and 585 nm for PI.

2.1.2 SiO$_2$/TiO$_2$ hollow nanoparticles

2.1.2.1 Fabrication of SiO$_2$/TiO$_2$ hollow nanoparticles

Silica nanoparticles (SiO$_2$ NPs) were firstly prepared according to Stöber method. For preparing silica NPs, 2.3 mL of tetraethyl orthosilicate (Aldrich, St. Louis, MO) was added to the mixture solution of ethanol (60 mL), ammonium hydroxide solution (3.0 mL), and water (1.0 mL). Especially, sol-gel reaction was performed for 6 h under various temperature conditions (55, 50, 40, 35, and 20 ^{o}C) for synthesizing silica NPs and following 25-nm, 50-nm, 75 nm-, 100-nm, and 125-nm hollow NPs. Then, 2.9 mL of titanium (IV) isopropoxide (Aldrich, St. Louis, MO) was introduced in above-mentioned solution for the titania coated layer and the resulting solution was stirred for 6 h at room temperature. The prepared SiO$_2$/TiO$_2$ core/shell NPs were redispersed in sodium hydroxide solution (1.0 M, 10 mL) and then stirred for 3 h at RT. After the reaction, synthesized hollow NPs were collected by centrifugation.

TEM images were obtained with a JEOL EM-2000 EX II microscope. The size distribution of SiO$_2$/TiO$_2$ hollow NPs (HNPs) were measured by ELS–8000 (Otsuka Electronics, Japan) utilizing an ELS.

2.1.2.2 Cytotoxicity evaluation with size dependence

Human breast cancer SK-BR-3 and mouse alveolar macrophage J774A.1 cell lines were purchased from American Type Culture Collection (ATCC, Manassas, VA). Both cells were cultured with RPMI-1640 medium, with 10% FBS and 1% penicillin-streptomycin solution. The cell lines were incubated in a 5% CO_2 incubator at 37 ^{o}C and 100% humidity.

To visualize incorporated HNPs into cells, the surfaces of the HNPs were modified using 3-aminopropyl-trimethoxysilane. And then, amino-modified HNPs with different diameters were tagged with fluorescein isothiocyanate (FITC; Sigma, St. Louis, MO). Cells were seed at a density of 3000 cells per well, in 8-well Lab-Tek^{TM} coverglass (Nunc, Thermo Fisher Scientific) and treated with FITC-tagged HNPs (FITC-HNP; 10 μg mL^{-1}). After 24 h incubating, live cell imaging were obtained by DeltaVision® RT imaging system (Applied Precision) under 37 ^{o}C and 5% CO_2 concentration. In order to measure the cellular uptake quantitatively, flow cytometric analysis was performed. Cells were seeded in a 6-well plate (Falcon, USA). After 25 μg mL^{-1} of FITC-HNPs treatments for 24 h, the medium was aspirated to eliminate floating HNPs. Cells were collected and centrifuged. The cells were then rinsed with 0.1 M PBS and resuspended in PBS. Flow cytometry analysis was performed with FACSCalibur flow cytometry.

ICP (JP/ICPS-7500, Shimdzu) measurement was used for quantifying of incorporated HNPs into cells. The cells were seeded in a 6-well plate and treated with 25 μg mL^{-1} of the HNPs for 24 h. The cells were washed and collected. The cells were resuspended in distilled water and centrifuged again. After the cells were dried overnight, 48-51 wt% HF was added to allow dissolution of HNPs. Then, 2 wt% HNO$_3$ in aqueous solution was added to allow dissolution of the cells with ultrasound. The mass of HNPs in cells was measured by detecting the titanium concentration with ICP. The weight of intracellular HNPs based on particle numbers in TEM images by following formula:

$$\text{Intracellular HNP weight} = \frac{4}{3}\pi (R^3 - r^3)\rho n$$

where R is the outside radius of the HNP, r is the inside radius, ρ is the density of the HNPs, and n is the average number of intracellular HNPs.

The cellular uptake of the HNPs into the cells was observed with TEM (JEM-2000EXII, JEOL). Sample preparations for TEM images, cell viability test, ROS measurement, and apoptosis detection were described in part 2.1.1.2.

2.1.3. Ba/Sr doped SiO$_2$/TiO$_2$ hollow nanoparticles

2.1.3.1 Fabrication of Ba/Sr doped SiO$_2$/TiO$_2$ hollow nanoparticles

Monodisperse SiO$_2$ NPs and SiO$_2$/TiO$_2$ core/shell NP were prepared and the detailed procedure was described in 2.1.2.1. To fabricate pristine, barium-doped, and strontium-doped hollow nanoparticles (p-HNPs, Ba-HNP, and Sr-HNP; HNPs), the resulting SiO$_2$/TiO$_2$ core/shell nanoparticle (CSNP) were treated with ammonia solution (0.1 M), barium hydroxide solution (0.2 M), and strontium hydroxide solution (0.15 M) for 2.5 h under sonication, respectively. The products were thoroughly washed with DI water and 0.1 M PBS solution. To load NGF into the HNPs, 4 μg NGF (Sigma, St. Louis, MO, USA) was added to the HNPs in DMSO (1 mg mL^{-1}). After being stirred for 24 h, NGF-loaded HNPs were collected by centrifugation and dried in vacuum oven to remove DMSO. The dried NGF-encapsulated HNPs were washed with 0.1 M PBS to remove absorbed NGF on the HNPs.

TEM images were acquired with a JEM-200CX (JEOL). HADDF-STEM images and STEM-EDX elemental maps were achieved using STEM (Tecnai F20, FEI) equipped with a Gatan image filter (Gatan, Inc.). Atomic percent of the elements (Si, Ti, Ba, and Sr) were calculated by FE-SEM (JSM-6701F, JEOL) equipped with an EDX facility (INCA Energy). The XPS and XRD spectra were obtained with an AXIS-His (KRATOS) and M18XHF SRA

(MAC Science Co.), respectively. The BET surface area of the HNPs was measured on ASAP2010 (Mircometrics).

Metal ion dissolved from the HNPs was measured as a function of a time. The HNPs were suspended in high ionic strength solution (0.1 M PBS, pH 7.4) and lysosomal buffer solution (pH 4.5) at a concentration of 5 μg mL^{-1}. The lysosomal buffer solution was prepared by mixing potassium acetate (24.5 mL, 0.2 M) and glacial acetic acid (25.5 mL, 0.2 M), followed by a dilution to 100 mL total volume. Then, 1 mL of each sample was extracted and centrifuged for removing the HNPs. The supernatant was transferred to a fresh vial and diluted 10 times with appropriate solvents for ICP-MS analysis (JP/ICPS–7500, Shimdzu).

2.1.3.2 Application for neuronal differentiation

Rat pheochromocytoma PC12 cell (American Type Culture Collection, Manassas, VA, USA) were cultured in RPMI-1640 medium with 10% horse serum (HS), 5% fetal bovine serum (FBS), and 1% penicillin-streptomycin solution. For differentiation of PC12 cells, cells were seeded and incubated for 24 h in serum-reduced medium (1% HS and 0.5% FBS) before treatment with the HNPs. The HNPs were inserted into the medium at concentrations ranging from 5 to 25 μg mL^{-1}. Simultaneously, 100 ng mL^{-1} of NGF and 0.1% bovine

serum albumin (BSA) were added into the medium to induce the differentiation of PC12 cells. Fresh NGF and BSA were supplied to the medium every day.

β-tubulin (III) expression is evidence for differentiation of PC12 cells. As mentioned before, differentiated cells were fixed with 4% paraformaldehyde for 10 min, permeabilized with 0.5% Triton X-100 for 5 min, and blocked with 0.1% BSA for 15 min. Then, the cells were immunostained with Alexa Fluor®488 mouse anti-β-tubulin, Class III (neuron specific; BD bioscience, San Jose, CA, USA) for overnight at 37 °C. After being washed with 0.1 M PBS, the samples were mounted using Fluoroshield™ with DAPI (4,6-diamidino-2-phenylindole dihydrochloride; Sigma, USA) and observed by Delta Vision® RT imaging system (Applied Precision, Issaquah, WA).

For clarifying the differentiation mechanism, the proteins involved in signal transduction pathways were analyzed by flow cytometry. As mentioned above, differentiated PC12 cells were fixed with 4% paraformaldehyde for 20 min, permeabilized with 0.1% Triton X-100 for 15 min, and blocked with blocking solution (0.1 M PBS, 10% FBS, and 0.03% 1 M NaN_3) for 30 min. Specific antibodies against pERK, pp38, pJNK, Trk A, and pAkt were diluted with blocking solution according to the manufacturer's instruction, and added into cells for 1 h, respectively. All antibodies were purchased from Santa Cruz Biotechnology Inc.(Santa Cruz, CA, USA). The cells were stained with FITC

conjugated secondary antibodies for another 1 h, than they were analyzed with flow cytometry (FACS Aria I, BD Bioscience, USA).

To determine release profile of NGF from NGF-HNPs, NGF-HNPs was dispersed in 1 mL PBS and 1 mL DMSO with 0.02% sodium azide in 24-well plates. They were incubated at $37\,^{\circ}C$ with shaking. Supernatant was collected at various time-points, centrifuged for removing the HNPs, and transferred to a fresh 24-well plate. The amount of NGF was measured using an enzyme-linked immunosorbent assay (ELISA) kit (human beta NGF Duoset; R&D Systems, Minneapolis, USA). The protocol of this assay followed manufacturer's instructions. Absorbance was detected at 450 nm using a Victor[3] Multilabel Readers (Perkin Elmer, Boston, MA, USA). The amount of NGF was determined from a calibration curve based on known concentrations of NGF. Experiments were performed using five replicates of each sample.

Sample preparations for TEM analysis, viability assay, and ROS assay were also the same as those described in part 2.1.1.2.

2.2. PEDOT based hybrid nanoparticles

2.2.1. MnO$_2$ decorated PEDOT nanoparticles

2.2.1.1 Fabrication of MnO$_2$ decorated PEDOT nanoparticles

PEDOT nanoparticles (PEDOT NPs) were fabricated *via* chemical oxidation polymerization using AOT micelles as the soft template. AOT was dissolved in hexane at a concentration of 3.4 x 10^{-1} M, and 7 M of aqueous FeCl$_3$ solution was added. The volume ratio of aqueous FeCl$_3$ solution to hexane was 1.1 x 10^{-2}. All reactions were carried out at 20 ^{o}C. The resulting products were washed with ethanol to remove residual impurities (residual monomers, surfactants, and oxidizing agents). More detailed experimental procedures and conditions are described in our previous paper. [5, 53] PEDOT NPs were treated with various concentrations of KMnO$_4$ (5, 10, and 25 mM) under vigorous stirring conditions. MnO$_2$/PEDOT NPs were formed by reaction between the oxidant and the reductant. Amount of MnO$_2$ domains depended on the concentration of KMnO$_4$ solution and treatment time. The more MnO$_2$ domains were loaded in the PEDOT NPs, the more cells were differentiated. However, PEDOT NPs can be overoxidized by KMnO$_4$ solution, which may cause conductivity decrease.[54] To keep balance between neuronal differentiation efficiency and conductivity for sensor application, PEDOT NPs were treated with 10 mM KMnO$_4$ solution for 10 min. The resulting products

were thoroughly washed with deionized (DI) water and 0.1 M PBS solution to remove oxidizing agent.

Photographs of TEM and HRTEM were acquired with a JEOL JEM–200CX and JEOL JEM–3010, respectively. The amount of MnO_2 domains were investigated using FE–SEM (JEOL–6700) equipped with EDX and ICP analysis (JP/ICPS–7500, Shimdzu). The XPS data were obtained with an AXIS–His X–ray photoelectron spectroscopy analyzer (KRATOS). Zeta potential of PEDOT and MnO_2/PEDOT NPs was measured by electrophoretic light scattering with an ELS–8000 instrument (Otsuka Electronics, Japan). FT–IR spectra were recorded on a Bomem MB 100 spectrometer (Quebec, Canada) in absorption modes at a resolution of 4 cm^{-1} and 64 scans. Electrical conductivity was measured by a source–meter at ambient temperature by a four–probe method.

A leaching profile of the Mn^{2+} ions from MnO_2/PEDOT NPs was measured in high ionic strength solution (0.1 M PBS) and cell culture medium as a function of a time. MnO_2/PEDOT NPs (5 μg mL^{-1}) were suspended in above mentioned solvents with moderate stirring. Each sample (1 mL) was extracted and centrifuged. The supernatant was transferred to a fresh vial and diluted 5 times with appropriate solvents for ICP–MS analysis.

2.2.1.2 Application for neural differentiation

Rat pheochromocytoma PC12 cell were used for neuronal differentiation. The culture/neuronal differentiation condition and β-tubulin (III) staining were the same as those described in part 2.1.3.2. The concentration of HNPs was ranging from 5 to 25 μg mL^{-1}. Sample preparations for TEM analysis, viability assay, and ROS assay were also the same as those described in part 2.1.1.2.

For immunocytochemistry, 1.0×10^5 cells mL^{-1} of PC12 cells were treated with MnO$_2$/PEDOT nanomaterial (5, 10, and 25 μg mL^{-1}), NGF, and BSA for 1 day. After being washed with 0.1 M PBS, the cells were fixed with 4% paraformaldehyde for 20 min, permeabilized with 0.1% Triton X–100 for 15 min, and blocked with blocking solution (0.1 M PBS, 10% FBS, 0.03% 1 M NaN$_3$) for 30 min. Specific antibodies against phosphorylated ERK1/2 (pERK) and DMT1 (Santa Cruz Biotechnology Inc., Santa Cruz, CA, USA) were diluted with blocking buffer according to the manufacturer's recommendation and incubated with cells for 1 h, respectively. Then, the cells were stained with FITC conjugated secondary antibodies for another 1 h. Cells were washed with 0.1 M PBS and analyzed with flow cytometry (FACS Aria I, BD Bioscience, USA).

2.1.1.3 Application for catecholamine detection

To construct MnO_2/PEDOT sensor, interdigitated gold electrodes in ECIS chips (8W10E+, Applied Biophysics, Troy, NY) were used as source–drain electrodes. ECIS chip has 8 wells, and each well consists of eight sets of interdigitated gold electrodes (7.5 mmX0.5 mm, rectangular shape). Culture chamber (600 μL volume, 0.8 cm^2) was used for cell culture–based measurements. For immobilization of MnO_2/PEDOT nanomaterial as a transducer, 20 μL of 0.1 wt% MnO_2/PEDOT nanomaterial was dropped on the electrodes, and immobilized onto the substrate by vacuum dehydration. The source–drain current was monitored when catecholamines were inserted to a chamber with a gradual increase in its concentration from 0.25 mM to 2.5 mM (V_{DS}=50 mV). To detect the secretion of catecholamines from living cells, PC12 cells (3000 cells) were seed on a chamber of the MnO_2/PEDOT sensor with 400 μL of serum–reduced medium (1% HS and 0.5% FBS) for 24 h. As mentioned above, PC12 cells were treated with MnO_2/PEDOT nanomaterial, NGF, and BSA for 24 h. After washing with PBS, cells were treated with calcimycin and high potassium solution (40 mM NaCl, 105 mM KCl, 6 mM $CaCl_2$, 1 mM $MgCl_2$, and 10 mM HEPES).[55, 56] The source–drain current was monitored at a voltage bias of 50 mV. All measurements were conducted with a Wonatech WBCS 3000 potentiostat.

2.3. PAN based hybrid nanoparticles

2.3.1. Amidine-PAN nanoparticles for Cu^{2+} detection

2.3.1.1 Fabrication of amidine-PAN nanoparticles

Polyacrylonitrile nanoparticles (PAN NPs) were fabricated by ultrasonic mediated emulsion polymerization.[57] Acrylonitrile monomer (1.5 mL) and sodium dodecylsulfate (0.5 g) were dissolved in distilled water (20 mL). Ultrasound (350 W) was introduced in the mixed solution for 10 min to form emulsion phase. Cerium sulphate (0.1 g) and nitroacetic acid (0.025 g), as initiators, were added into the solution. Then, PAN NPs were polymerized for 30 min under ultrasound irradiation. The resulting particles were thoroughly washed with excess methanol. In order to introduce the amine group on the surface of PAN NPs (amine-PAN NPs; APAN NPs), Pinner synthesis was used. PAN NPs (0.5 g) were dispersed in ethanol (10 mL), and they mixed with solution containing HCl (1 M, 2 mL) and diethyl ether (18 mL) at 0 °C for 72 h under N$_2$ atmosphere. The product was washed with ethanol, and treated with ammonia solution (20 mL) at RT for 3 h under a nitrogen purge. The product was washed with ethanol several times.

The transmission electron microscope (TEM) and scanning electron microscope (SEM) images were taken with a JEOL JEM-2100 and JEOL 6330F, respectively. FT-IR spectra were collected with a Thermo Scientific

Nicolet 6700 FTIR spectrophotometer. The fluorescent emission spectra of APAN NPs were obtained with a JASCO FP-6500 spectrofluorometer. The XPS data were measured by an AXIS-His X-ray photoelectron spectroscopy analyzer (KRATOS). The quantum yield of APAN NPs was obtained by comparing between the fluorescence emission of reference dye and that of APAN NPs. 7-amino-4-methylcoumarin is blue-emitting dye with high quantum yield ($\Phi = 0.88$), which is used as standard reference. The quantum yield of amidine-PAN particles was calculated by the following equation:

$$\Phi_L = \frac{F_L}{A_L} \times \frac{A_D}{F_D} \times \Phi_D$$

where Φ is the fluorescence quantum yield, F is the integrated area of emitted fluorescence spectra, and A is the absorbance at the excitation wavelength. The subscript L and D implied APAN NPs and 7-amino-4-methylcoumarin, respectively.

2.3.1.2 Application for intracellular Cu^{2+} detection

Human breast cancer SK-BR-3 cells (American Type Culture Collection, Manassas, VA, USA) were cultured in RPMI-1640 medium with 10% fetal bovine serum and 1% penicillin-streptomycin solution. They were maintained in a 75T flask at 37 °C in humidified 5% CO_2 atmosphere and passaged at 70-80% confluence.

In order to observe APAN NP-treated cells, SK-BR-3 cells were seeded at a density of 3000 cells per well, in 8-well Lab-Tek II chambered coverglass (Nunc, Thermo Fisher Scientific, USA) and inserted with 10 μg mL^{-1} of amidine-PAN NPs. After 24 h, the cells were washed twice with 0.1 M phosphate buffered solution (PBS), and treated with 10 μM CuCl$_2$ for 20 min at 37 °C. As control experiment, excess ethylenediaminetetraacetate (EDTA, 100 μM) was incubated simultaneously for 20 min to remove Cu^{2+} from the culture medium. The cells were washed again and analyzed with a Delta Vision RT imaging system (Applied Precision, Issaquah, WA, USA).

The experimental condition for cell viability assay and ROS production were the same as those described in part. 2.1.1.2

2.3.2. Au decorated amidine-PAN nanoparticles for intracellular highly reactive oxygen species detection

2.3.2.1 Fabrication of Au/amidine-PAN nanoparticles

PAN NPs were fabricated by ultrasonic mediated emulsion polymerization. Detailed fabrication method was described in part 2.3.1.1. The gold nanoclusters (AuNCs) were synthesized by reduction of $HAuCl_4$ with L-glutathione (GSH). According to the previous report, GSH aqueous solution (6 mM, 10 mL) was mixed with $HAuCl_4$ aqueous solution (4 mM, 10 mL) under stirred condition at 90 °C for 6.5 h.[58] To prepare Au-APAN NPs, AuNCs (2 mg mL^{-1}, 40 mL) were mixed with 300 mg mL^{-1} of EDC for 15 min. APAN NPs (50 mg mL^{-1}, 1 mL) aqueous solution was reacted with 300 mg mL^{-1} of NHS for 15 min. Then, APAN NPs, which are activated by N-hydroxysuccinimide, were poured into the solution containing AuNCs and 1-ethyl-3-(3-dimethylaminopropyl)-carbodiimide, and reacted with vigorous stirring for another 2 h. Resulting Au-APAN NPs were washed with distilled water and centrifugation, and redispersed in 0.1 M PBS solution for further bio-application.

Images of TEM and HRTEM were taken by a JEOL JEM-2100 and JEOL JEM-3010, respectively. FT-IR and XPS spectra were collected with a Thermo Scientific Nicolet 6700 FTIR spectrophotometer and AXIS-His X-ray

photoelectron spectroscopy analyzer (KRATOS). The fluorescent emission spectra were obtained with a JASCO FP-6500 spectrofluorometer. The amount of Au on the Au-APAN NPs was investigated using ICP-MS analysis (JP/ICPS-7500, Shimdzu).The quantum yield of Au-APAN NPs was calculated by the equation in part 2.3.1.1. As reference dye, 7-amino-4-methylcoumarin and rhodamine B were used for APANs and AuNCs, respectively.

The fluorescence intensity changes of Au-APAN NPs by response of highly reactive oxygen species (hROS; O_2-, OCl^-, and $\cdot OH$) were detected at 405 and 560 nm (λ_{ex}=290 nm). A 4-(2-hydroxyethyl)-1-piperazine-ethanesulfonic acid (HEPES, 0.1 M, pH 7) buffer solution was used in all experiments. The concentration of the Au-APAN NPs was fixed at 10 μg mL^{-1}. Various types of hROS were generated as following. (a) H_2O_2, and OCl^-, H_2O_2 and OCl^- were obtained from 35% H_2O_2 and 5% NaOCl, respectively. They were inserted to the Au-APAN NP solution, and they were analyzed after 2 h. (b) $\cdot OH$: Au-APAN NP solution was mixed with 100 μM of H_2O_2. Then, 1 mM solution of $FeCl_2$ was added for 2 h. (c) O_2^-: Xanthine oxidase and xanthine were dissolved in PBS and dimethylformamide, respectively (10 mM). Au-APAN NPs in 0.1M PBs (10 mM, pH 7.4), xanthine oxidase solution and xanthine solution (final concentration, 33 μM, containing 6.7% DMF as a co-solvent) were added.

2.3.2.2 Application for intracellular highly reactive oxygen species detection

Mouse macrophage RAW 264.7 cell lines were purchased from American Type Culture Collection (ATCC, Manassas, VA, USA), and cultured in Dulbecco's modified eagle medium with 10% fetal bovine serum and 1% penicillin/streptomycin at 37 °C under 5% CO_2 atmosphere.

RAW264.7 cells were spread at a density of 3000 cells per well, in 8-well Lab-Tek II chambered coverglass (Nunc, Thermo Fisher Scientific, USA) for 24 h. Cells were inserted with 10 μg mL^{-1} of Au-APAN NPs for 24 h, and washed with 0.1 M PBS. Three types of control experiments were conducted to explain the relationship between hROS and Au-PAN NPs. First, RAW264.7 cells were treated with 10 μg mL^{-1} of Au-APAN NPs for 24 h, and then inserted with phorbol 12-myristate 13-acetate (PMA, 1 μg mL^{-1}) for another 2 h. In second control experiment, RAW264.7 cells were co-inserted with 10 μg mL^{-1} of Au-APAN NPs and TEMPO (500 μM) for 24 h, then incubated with PMA (1 μg mL^{-1}) for another 2 h. As last control experiment, RAW264.7 cells were introduced with 10 μg mL^{-1} of Au-APAN NPs for 24 h, and treated with PMA (1 μg mL^{-1}) for 1 h. Then, uric acid (250 μM) and DMSO (0.5%) were co-inserted into the cells for 15 min. Fluorescent images were obtained by a Delta Vision RT imaging system (Applied Precision, Issaquah, WA, USA).

For quantification, cells were cultured in dishes (5×10^5 cells; Nunc, Thermo Fisher Scientific, USA) and treated with Au-APAN NPs (25 μg mL^{-1}), PMA (1 μg mL^{-1}), TEMPO (500 μM), uric acid (250 μM) and DMSO (0.5%) as mentioned above. Cells were washed, trypsinized, and collected in flow cytometry tube. Flow cytometry analysis was performed by using a FACSCalibur flow cytometer (Becton Dickinson, USA).

The experimental condition for TEM images, cell viability assay and ROS production were the same as those described in part. 2.1.1.2

3. RESULTS AND DISCUSSION

3.1. SiO$_2$ based hybrid nanoparticles

3.1.1. Metal oxide decorated SiO$_2$ nanoparticles

3.1.1.1 Fabrication of metal oxide decorated SiO$_2$ nanoparticles

Figure 8a is a schematic diagram for fabrication of the five different metal oxide-decorated SiO$_2$ NPs (MOx-SiO$_2$ NPs) used in this study: CeO$_2$ (Ce-SiO$_2$), CuO (Cu-SiO$_2$), Fe$_2$O$_3$ (Fe-SiO$_2$), MnO$_2$ (Mn-SiO$_2$), and ZnO (Zn-SiO$_2$). SiO$_2$ NPs, fabricated by the Stöber method, were modified with N-[3-(trimethoxysilyl)propyl]ethylenediamine to capture precursor ions on their surface.[52] Iron, zinc, copper and cerium ions, were coordinated with the diamine species,[59] and the NDs were formed on the surface of the SiO$_2$ NPs by sol-gel method using sodium hydroxide. The MnO$_2$ NDs were fabricated by the reaction between potassium permanganate and formamide. The MnO$_4^-$ ions were also located on the surface of the amine-SiO$_2$ NPs by charge-charge interactions, and reduced by formamide. Figure 8b and c revealed the presence of NDs on the surface of SiO$_2$ NPs. Figure 8c illustrates histograms of SiO$_2$, amine-SiO$_2$, and MOx-SiO$_2$ NPs in DI water. Diameter of the SiO$_2$ NPs increased from *ca.* 24 nm to *ca.* 30 nm after silane treatment. The MOx-SiO$_2$ NPs averaged 42 nm in diameter due to NDs on the surface of the SiO$_2$ NPs. The ELS histograms exhibited relatively narrow size distribution of the NPs

due to their uniform silica cores, which could be applicable to research for cellular toxicity of the NPs.

HRTEM images revealed the presence of NDs on the surface of SiO_2 NPs, and each metal oxide was between 4-8 nm in size (Figure 8b). The amount of ND on the SiO_2 NPs was calculated as an average 12-13 wt% by inductively coupled plasma mass spectrometer (ICP-MS). This method enabled us to evaluate and compare the precise nanotoxicity of various element NDs on the surface of silica NPs. To the best of our knowledge, this is the first attempt to compare nanomaterials as metal oxide with controlled physical properties (size: *ca.* 42 nm, shape: sphere, MOx content: 12~13 wt%) on the SiO_2 NPs for precise nanotoxicity.

The chemical composition and crystallinity were analyzed by X-ray diffraction (XRD). As shown in Figure 9, a broad peak between 20° and 30° showed the amorphous phase of SiO_2 NPs, and other sharp peaks displayed the crystalline phase of the NDs. A crystalline phase was detected without noticeable contaminants, and the chemical compositions of the NDs were determined by these sharp peaks. Further characterization of the MOx-SiO_2 NPs was provided in Table 2. The zeta potential (ζ) also provided evidence for the presence of NDs on the NP surface. Bare SiO_2 NPs were negatively charged, whereas the amine-SiO_2 NPs had a positive charge. After formation of

the NDs, the ζ of the NPs decreased due to the negative surface charge of the NDs. The dissolution of NDs was further investigated in distilled water and cell culture medium to estimate the effect of dissolved ions on cellular toxicity. About 7-9% of the NDs were leached as ions in distilled water, whereas 12.6% and 19.7% of the Cu-SiO$_2$ and Zn-SiO$_2$ NP dissolved, respectively. The dissolution of the NDs was decreased in culture medium due to the colloidal stability effects of the solvents.[60] Dissolved Cu^{2+} ions decreased from 12.6% to 1.79%, which was consistent with the other MOx-SiO$_2$ NPs except Zn-SiO$_2$ NPs. In case of Zn-SiO$_2$ NP, the released ions was still over 6% even in culture medium. Several papers reported that unlike other nanomaterials, nanosized ZnO undergoes rapid dissolution in cell culture medium, which was good agreement with our results.[61, 62]
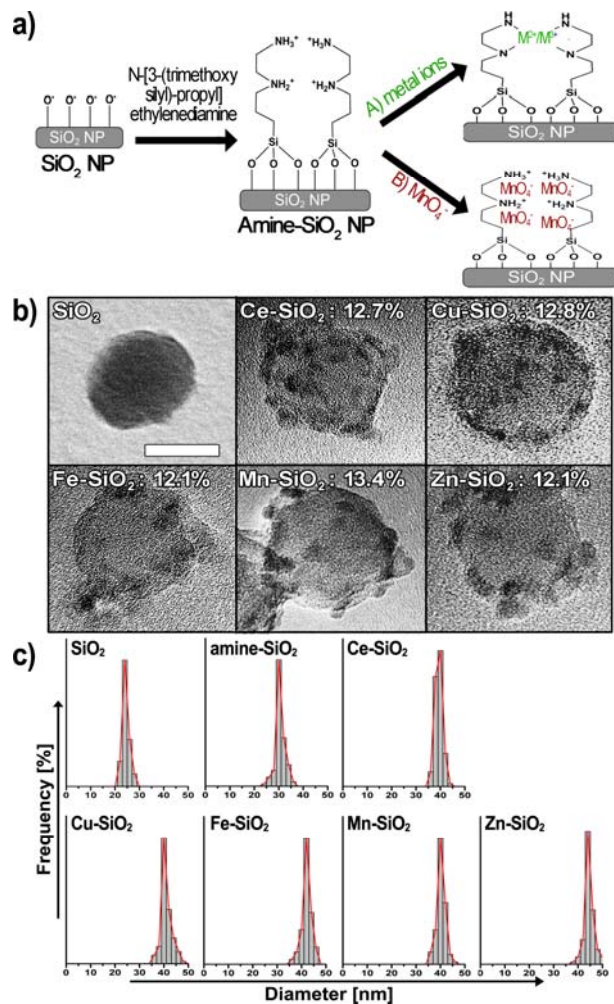
Figure 8. (a) A possible mechanism for fabrication of MOx-SiO$_2$ NPs, and (b) their HRTEM images (scale bar: 20 nm) and MOx content (ICP-MS). (c) Size distribution histograms of SiO$_2$, amine functionalized SiO$_2$, and MOx-SiO$_2$ NPs determined by ELS.
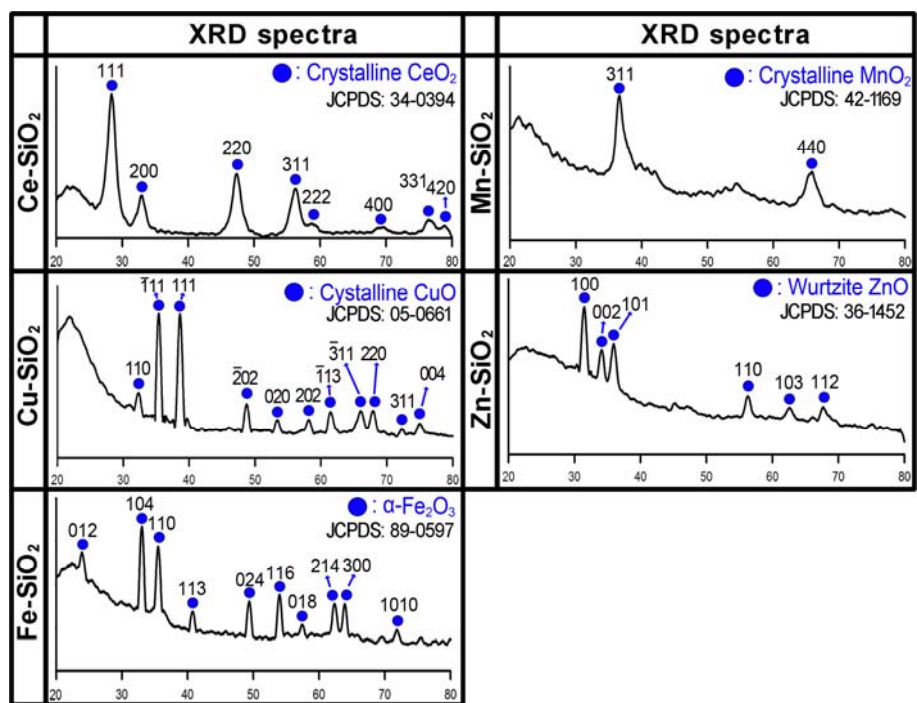
Figure 9. XRD spectra of MOx-SiO$_2$ NPs

Table 2. Characterizations of MOx-SiO$_2$ NPs

	Chemical Composition[a]	Crystallinity [unit cell][a]	ζ (mV)[b]	Dissolution (%)[d]	
				Water	Medium[e]
SiO$_2$	N/A	Amorphous	-31.5 ± 3.2	N/A	N/A
amine-SiO$_2$	N/A	Amorphous	38.1 ± 4.1	N/A	N/A
Ce-SiO$_2$	CeO$_2$	Crystalline [Cubic]	-16.2 ± 1.1	7.1	1.2
Cu-SiO$_2$	CuO	Crystalline [Monoclinic]	23.0 ± 3.9	12.6	1.8
Fe-SiO$_2$	Fe$_2$O$_3$	Alpha type [Rhombohedral]	-14.4 ± 3.5	7.3	3.8
Mn-SiO$_2$	MnO$_2$	Crystalline	-11.0 ± 2.2	6.9	0.8
Zn-SiO$_2$	ZnO	Wurtzite [Hexagonal]	13.7 ± 1.2	19.7	6.4

[a] The crystallinity of ND was determined by XRD spectrum. [b] ζ of the MOx-SiO$_2$ NPs in aqueous solution was measured by ELS-8000. [c] The weight ratio of ND in MOx-SiO$_2$ NPs were analyzed by ICP-MS. [d] Dissolution of the NDs was evaluated using ICP-MS at 37 °C in supernatant of the water and culture mediums for 24 h. [e] DMEM with 10% fetal bovine serum, and 1% penicillin-streptomycin solution was used as culture medium.

3.1.1.1 Cytotoxicity evaluation with element dependence

Three cell lines were used for a comprehensive assessment of the toxic effects of MOx-SiO$_2$ NPs on various organs. Mouse macrophage RAW264.7, rat pheochromocytoma PC12, and calf pulmonary artery endothelial CPAE cell lines were used to investigate the effects of MOx-SiO$_2$ NPs. Macrophages are involved in the first-line immune defense and act as scavengers of foreign agents *via* phagocytosis.[63] PC12 serve as a model system for primary neuronal cells because of their ability to differentiate in response to nerve growth factors.[64] CPAE are used as blood vessel model system given their origin and ability to respond to vasicular endothelial growth factor.[15] A nanotoxicological evaluation using these three cell lines can provide a comprehensive assessment of the toxic effects of MOx-SiO$_2$ NPs on various organs.

The cellular uptake of MOx-SiO$_2$ NPs was observed by TEM (Figure 10a). Most of the endocytosed MOx-SiO$_2$ NPs were transported to lysosome *via* the endosome-network.[65] Some of the NPs dissolved at the low pH inside the lysosomes, which are induced lysosomal rupture (Figure 10c).[66, 67] When NPs were released from the lysosome to the cytoplasm through the ruptured membrane, the released MOx-SiO$_2$ NPs were partially moved to the mitochondria (Figure 10d).[66, 67] Compared with the mitochondria distant

from the NPs (Figure 10b), the mitochondria near the NPs appeared to be damaged (Figure 10d), suggesting that released NPs might have affected mitochondria function. Therefore, we focused on the mitochondrial dysfunction affected by MOx-SiO$_2$ NPs.

Figure 10e illustrates the ATP concentrations in MOx-SiO$_2$ NP-treated cells as a function of the concentration and the ND-type. From the viewpoint of cell lines, the viability of MOx-SiO$_2$ NPs-treated RAW264.7 was lower than that of other cells, mainly because RAW264.7 scavenges foreign agents. These findings are corroborated by previous reports.[2] Compared with SiO$_2$ NPs, Ce-SiO$_2$ NPs caused a significant increase in ATP content, whereas Fe-, Mn-, and Zn-SiO$_2$ NPs induced different toxic responses according to the cell lines. For example, Mn-SiO$_2$ NPs were toxic to PC12 and CPAE, but not to RAW264.7. Based on these data, they were classified into three groups according to toxic responses (Table 3): Group I (less toxic than SiO$_2$ NPs, red), Group II (similar toxicity to SiO$_2$ NPs, no color), and Group III (more toxic than SiO$_2$ NPs, blue). Toxicity of the MOx-SiO$_2$ NP depended on the element as well as the cell type.
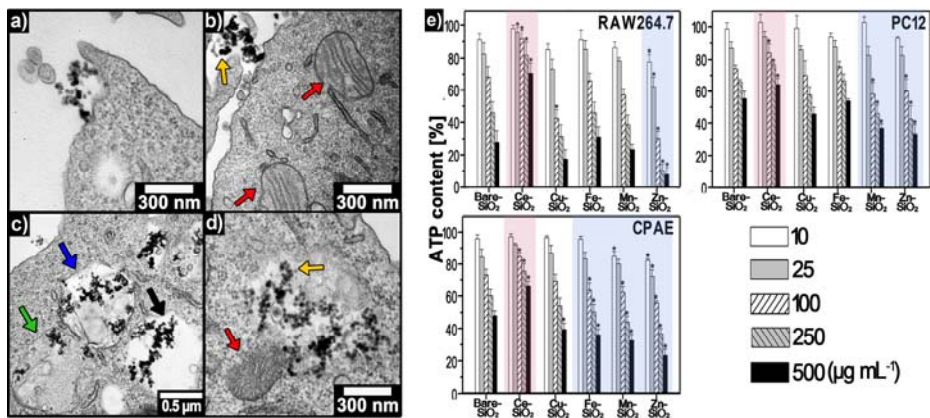
Figure 10. (a-d) TEM images of the Fe-SiO$_2$ NP treated RAW264.7 cells. The yellow and red arrows indicated Fe-SiO$_2$ NPs and mitochondria, respectively. The green, blue, and black arrows implied lysosomes, swelled lysosomes, and ruptured lysosomes, respectively. (e) Viability of the cells treated with MOx-SiO$_2$ NPs for 24 h, calculated relative to untreated cells. The red and blue means Group I and III, respectively.

Table 3. Classification of the MOx-SiO$_2$ NPs according to their toxicity

	Species	Origin	Group I[a]	Group II[b]	Group III[c]
RAW264.7	Mouse	Macrophage	Ce-SiO$_2$	Cu-SiO$_2$ Fe-SiO$_2$ Mn-SiO$_2$	Zn-SiO$_2$
PC12	Rat	pheochromocytoma	Ce-SiO$_2$	Cu-SiO$_2$ Fe-SiO$_2$	Mn-SiO$_2$ Zn-SiO$_2$
CPAE	Calf	pulmonary artery endothelial	Ce-SiO$_2$	Cu-SiO$_2$	Fe-SiO$_2$ Mn-SiO$_2$ Zn-SiO$_2$

[a] The Group I is less cytotoxic than that of bare SiO$_2$ NPs. [b] The Group II shows similar toxicity to bare SiO$_2$ NPs. [c] The Group III is more toxic than that of bare SiO$_2$ NPs.

ROS generations and the induction of oxidative stress are key toxicological paradigm for nanotoxicity. Excess ROS cause oxidative injury to DNA and stimulate apoptotic cell signaling.[61] H_2DCFDA was used to measure intracellular ROS production (Figure 11). Compared with ROS levels in bare-SiO_2 NP-incubated cells, ROS levels decreased in Ce-SiO_2 NP-treated cells (Group I). Cells treated with Ce-SiO_2 NPs produced more ATP and less ROS than those treated with SiO_2 NPs. We hypothesized that CeO_2 on the SiO_2 NPs could also protect cells against oxidative damages from an exogenous ROS source. To verify this hypothesis, cells were pretreated with 25 μg mL^{-1} of Ce-SiO_2 NPs for 24 h, followed by treatment with phorbol 12-myristate 13-acetate (PMA; 1 μg mL^{-1}) for 0, 2, and 12 h. A previous work has shown that PMA are inducing intracellular ROS generation.[68] In Figure 12a-c, ROS production was greater in the Ce-SiO_2 NP-treated cells than in the control at 0 h of PMA treatment. However, treatment with PMA decreased ROS generation in the Ce-SiO_2 NP-incubated cells. When the Ce-SiO_2 NPs and PMA were added simultaneously to the cells in a control experiment, no particular protective effect was observed (data not shown). Therefore, the Ce-SiO_2 NPs had to be internalization prior to the addition of PMA to achieve a protective effect. These results suggest that CeO_2 NDs SiO_2 NPs can reduce not only SiO_2 own toxicity but also ROS production in the presence of an exogenous ROS sources.

Several studies have demonstrated that CeO_2 can scavenge free radicals, resulting in an antioxidant effect in cells.[69] This property is attributable primarily to the reversible Ce^{3+}/Ce^{4+} redox couple, not the oxygen vacancies.[69] Possible reactions involving radical quenching and redox coupling reaction between Ce^{3+} and Ce^{4+} are shown below. These equations explained how the Ce^{3+}/Ce^{4+} mixed oxidation state are required for radical scavenging.

$$Ce^{3+} + O_2^{\cdot -} + 2H^+ (aq) \rightarrow Ce^{4+} + 2H_2O_2 \qquad (1)$$

$$2\,Ce^{4+} + 2H_2O_2 \rightarrow 2\,Ce^{3+} + 2H^+ + O_2^{\cdot} \qquad (2)$$
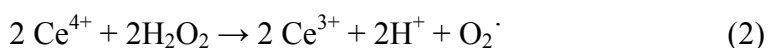
To explain the antioxidant effects of CeO_2 NDs on SiO_2 NPs, the oxidation state of CeO_2 was confirmed using XPS analysis (Figure 12d). The Ce 3d spectra were based on prior research; two sets of spin-orbital multiplets, corresponding to $3d_{3/2}$ and $3d_{5/2}$, were labeled as u and v, respectively.[70] The Ce 3d spectra of the Ce-SiO_2 NPs were deconvoluted as myriad peaks, indicating that the CeO_2 NDs consisted of a mixture of Ce^{3+} and Ce^{4+} oxidation states. CeO_2 undergoes easy, fast, and reversible reduction and can readily take up and release oxygen, alternating between CeO_2 and CeO_{2-X}.[71] Thus, the protective effects of CeO_2 NDs on SiO_2 NPs originate from its mixed

Ce^{3+}/Ce^{4+} oxidation states, in accordance with reported data. As contrasted with Ce-SiO$_2$ NPs, other MOx-SiO$_2$ NP had no scavenging ability for free radicals.

In case of Group III, they evoked a more noticeable increase in ROS unlike the Group I, and this was associated with the viability results. Among various pathways, numerous research results have been reported that intracellular ROS were mainly generated by mitochondrial dysfunction.[60] As mentioned earlier, some free MOx-SiO$_2$ NPs released from lysosomes moved to mitochondria, which can induce mitochondrial ROS generation. Mitochondrial ROS production was measured using MitoSOX Red. Mitochondrial ROS values were almost equal to intracellular ROS levels and were dependent on the ND element and cell type, indicating that the production of intracellular ROS was related primarily to the mitochondria. In addition to free MOx-SiO$_2$ NPs, metal ions also contributed to mitochondrial ROS generation. They were formed by acidification of the MOx-SiO$_2$ NPs in lysosomes (pH 4.7) and endosomes (pH 5.5-6.3), released into cytosol, and interacted with the mitochondria.[60]
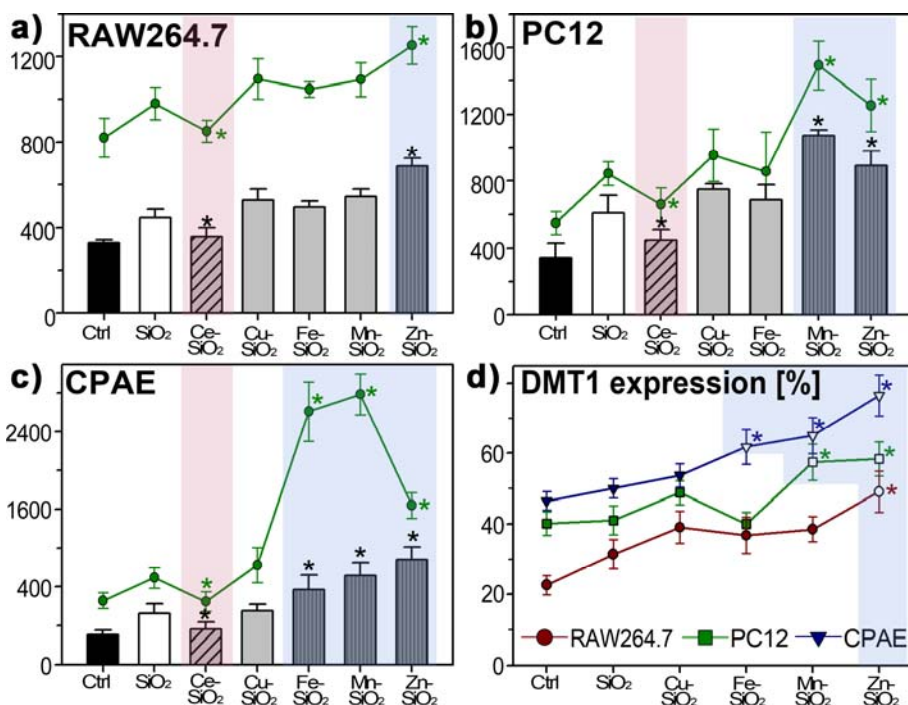
Figure 11. (a-c) Effect of MOx-SiO$_2$ NPs on intracellular (bars) and mitochondrial ROS (green circles) production (Y axis: mean fluorescence intensity). (d) Effect of MOx-SiO$_2$ NPs on DMT1 expression. Among graphs, cells were treated with 25 μg mL^{-1} MOx-SiO$_2$ NPs for 24 h. Free of NPs in the cells was used as a control (Ctrl). The red and blue means Group I and III.
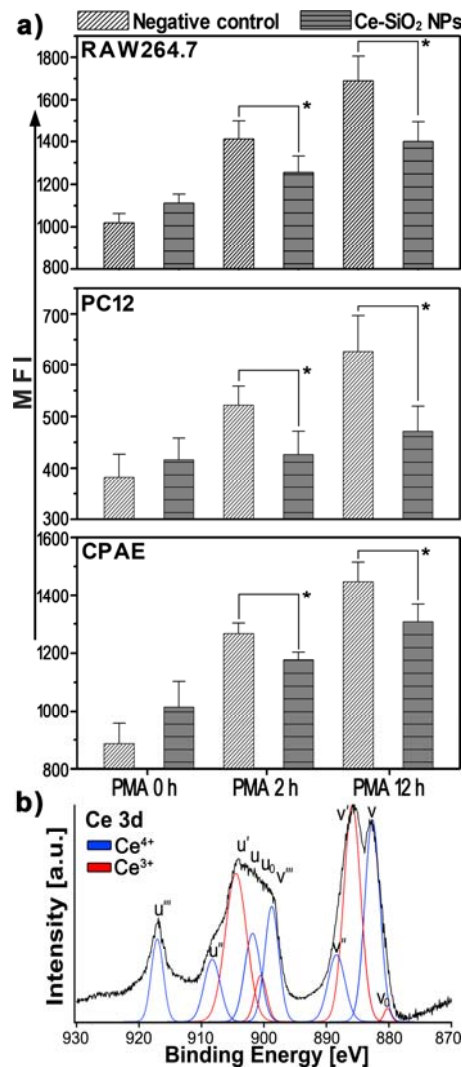
Figure 12. (a) Protective effect of the Ce-SiO$_2$ NPs on PMA induced ROS in the cells. The cells were pretreated with 25 μg mL^{-1} Ce-SiO$_2$ NPs for 24 h, followed by addition of 1 μg mL^{-1} of PMA for 0, 2, and 12 h. The PMA plays a role as ROS inducer in cells. Among graphs, free of NPs in the cells was used as a negative control. (b) XPS spectrum of Ce-SiO$_2$ NP. Two sets of spin-orbital multiplets, corresponding to the 3d$_{3/2}$ and 3d$_{5/2}$, were labeled as u and v, respectively.

A salient feature of mitochondrial damage is the collapse of the mitochondrial membrane potential (MMP), which are monitored with JC-1 dye. The red to green fluorescence intensity ratio indicate the degree of MMP collapse and compromised mitochondrial function (Figure 13). Cells exposed to Group II showed no significant change in MMP, and MMP was not disrupted in the Group I. When cells were treated with Group III, a remarkable loss of MMP was observed. Disruption of the MMP causes mitochondrial permeability transition pore opening and the release of cytochrome c from the mitochondria, leading to cell death.[19] Moreover, the loss of MMP is known to be an early event in apoptosis.[19] For these reasons, it is necessary to further investigate the cell death mechanism in MOx-SiO$_2$ NP-treated cells.

Cells death mechanism can be verified using Alexa Fluor[®] 488 conjugated annexin V (green) and propidium iodide (red) double staining (Figure 14a-c). The number of green and red dots was in order of Group III > SiO$_2$ NP & Group II > Group I. In Group I, the red dots diminished and green dots also decreased, suggesting that early apoptosis was dominant. Some green dots were found at blebs on the plasma membrane, which is one of the characteristics of apoptosis. However, these images were insufficient to determine whether late apoptosis or necrosis was the cause of cell death. Therefore, we further conducted flow cytometric analysis using double stained

cells to quantify cell death (Figure 14d-f). Cell viability based on this assay was similar to that based on ATP assay. The decreased viability of SiO_2 NP-incubated cells was mainly due to an increase in early apoptotic cells. The sum of early and late apoptotic cells was similar between Group II- and Group III-treated cells, but was lower for Group I-treated cells. Early apoptosis was diminished by the protective effects of Ce NDs, accounting for the increased viability of Group I-treated cells. Though Group III- and SiO_2 NP-treated cells had a comparable sum of early and late apoptotic cells, the percentage of viable Group III-treated cells were remarkably lower by below 10%. Mitochondria-dependent apoptosis has been reported to occur in response silver and TiO_2 NPs.[72, 73] The reduced viability of Group III-treated cells was associated with an increased number of necrotic cells. Based on the hierarchical stress model, Foldbjerg suggested that the necrosis will be favored over apoptosis when NPs generate more ROS at a level above the threshold value.[61, 74] Considering this models, amount of ROS induced by Group III reached the threshold level, thereby leading to necrosis instead of apoptosis.

Figure 13. Effect of MOx-SiO$_2$ NPs on MMP. Cells were treated with the MOx-SiO$_2$ NPs for 24 h (25 µg mL^{-1}). Free of NPs in the cells was used as a control (Ctrl). The red and blue area means Group I and Group III, respectively.

Figure 14. Cell death mechanism determined by fluorescence images and flow cytometric analysis. Unstained and dual-stained cells were presented viable and late apoptotic cells. The green/red fluorescent labels represent as early apoptotic/ necrotic cells (scale: 20 μm). Among the experiments, cells were treated with the MOx-SiO$_2$ NPs for 24 h (25 μg mL^{-1}). Free of NPs in the cells was used as a control (Ctrl). The red and blue area means Group I and Group III, respectively.

3.1.2 SiO$_2$/TiO$_2$ hollow nanoparticles

3.1.2.1 Fabrication of SiO$_2$/TiO$_2$ hollow nanoparticles

Fabrication of SiO$_2$/TiO$_2$ Hollow nanoparticles (HNPs) were stated in 3.3.2. In this part, we fabricated HNPs with various diameters from 25 nm to 125 nm for evaluating cytotoxicity of the HNPs with size dependence. HNPs were evolved from silica/titania core/shell nanoparticles (CSNPs) as starting materials prepared by dissolution and re-deposition of silica. The diameter of HNP was determined by silica core size. First, silica NP was synthesized by sol-gel reaction. As the reaction temperature increased, the diameter of silica NPs decreased due to burst nucleation (55, 50, 40, 35, and 20 ^{o}C for 25 nm, 50 nm, 75 nm, 100 nm, and 125 nm). Then, CSNPs were obtained from introduction of titania layer onto the surface of silica NPs. Ammonium ions played a role in providing electrostatic interaction between titania precursor (titanium tetraisopropoxide; TTIP) and the surface of silica NPs as well as offering a catalyst for the synthesis. Under basic solution, the hollow nanostructures were transformed from the as-prepared core/shell nanostructures through the reversible process of dissolution of silica (core part) and re-deposition on the surface of the NPs. This morphological change is mainly due to the fact that hydroxide ion of the basic sodium hydroxide solution can dissolve silica by coordinating to silicon atoms and weakening siloxane bonds.[75]

Figure 15 illustrates representative TEM images of HNPs with controllable diameter and Electrophoretic Light Scattering Spectrophotometer (ELS) curves of the HNPs with different diameter. Remarkably, the TEM images of HNPs revealed uniform diameters of 25, 50, 75, 100, and 125 nm (denoted HNP25, HNP50, HNP75, HNP100, and HNP125, respectively). The ELS curves exhibited narrow size distribution that could be applicable to research for size dependent toxicity. The dispersibility of the HNPs was validated by well-dispersed solution with HNPs at 200 mg mL^{-1} after one year and this result was considered to be favorable in biomedical applications. Furthermore, these properties can provide the clear understanding of cellular response with nanoparticles with different physical parameter.
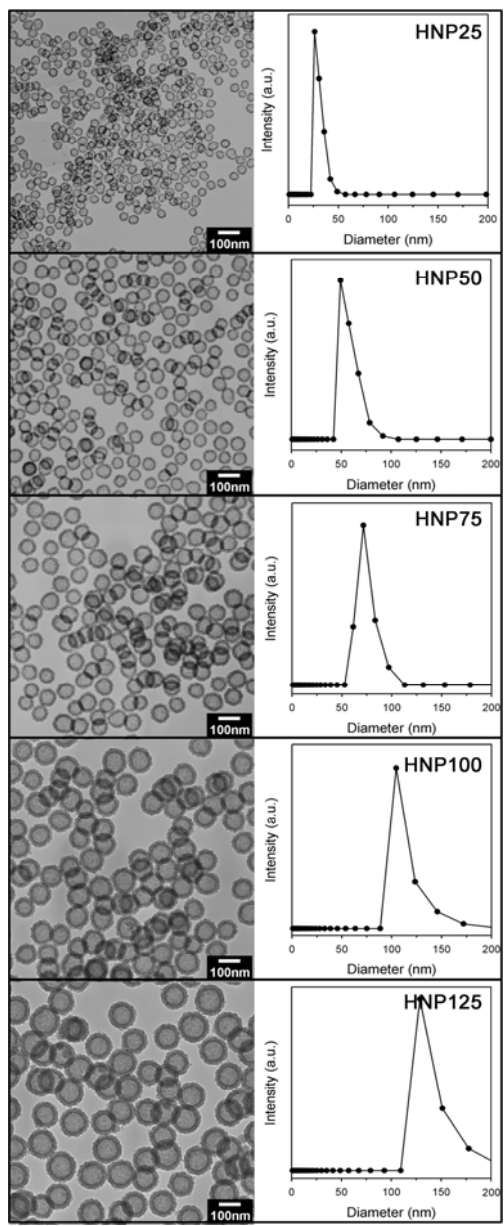
Figure 15. TEM images of HNPs of five different diameters and their corresponding size distribution by using ELS: HNP25, HNP50, HNP75, HNP100, and HNP125.

3.1.2.2 Cytotoxicity evaluation with size dependence

In order to quantify the internalized HNPs into the human breast cancer SK-BR-3 and mouse alveolar macrophage J774A.1 cells, fluorescein isothiocyanate (FITC) labeling on the HNPs (termed FITC-HNP) was performed *via* covalent linking between FITC and the HNPs. Figure 16 represents the flow cytometry analysis of SK-BR-3 and J774A.1 cells incubated with 25 μg mL^{-1} FITC-HNPs for 24 h. About 4-6 fold increase in the fluorescent intensity of HNP50-internalized SK-BR-3 and J774A.1 was observed distinct from that of HNP125-internalized SK-BR-3 and J774A.1. Distinct peaks of high fluorescent intensity were observed with HNP50- and HNP75-internalized cells, but lower fluorescent intensity from cells incubated with HNP25-, HNP100-, and HNP125-internalized cells. These latter cells had an emission spectrum near the control. Generally, the median value is considered to be the number of particles associated with the cells and show the cellular uptake.[76] Therefore, the cellular uptake was in order of HNP50>HNP75>HNP25, HNP100>HNP125.

The fluorescence images of the cells incubated with 10 μg mL^{-1} FITC-HNPs are shown in Figure 17. Both cell lines with HNPs had no considerable change in cell shape. Green fluorescence was observed inside and outside of the both cell lines. From the intensity and distribution of the FITC-HNPs, it is

considered that the number of the HNPs was taken up into cells. Among different sizes of the HNPs, HNP50 and HNP75 exhibited higher uptake ratio than other HNPs in both cell lines, which were consistent with flow cytometry result. Moreover, this result was consistent with the findings of Huang *et al.* that 70-nm SiO_2 NPs could translocate into the nucleoplasm of HepG2 cells.[77] In the case of J774A.1, the quantity of cellular HNPs was larger than the HNPs in SK-BR-3 due to phagocytosis.

Figure 18a exhibits TEM images of SK-BR-3 cells incubated with 10 μg mL^{-1} HNPs with different diameter. From the images, it could be considered that the cells ingested a relatively large amount of particles and cells retained cellular morphology without damage. The majority of particles seem to be confined inside cell that are distributed across the cytoplasm, but which did not cross into the nucleus. Within the cytoplasm, the NPs appeared to be located in vesicles. In the case of J774A.1, similar results were observed that intercellular HNPs spread in the cytoplasm and demonstrated size-dependent uptake. From the images, the intercellular HNPs retained their shapes in the both cells. The flow cytometry analyses (Figure 16) did not distinguish between NPs in the cell and those attached outside to the cell membrane. Therefore, we calculated the number of the HNPs in the cells using software based on 10 cells in the TEM images. The calculated values were summarized in Figure 18b.

Intracellular HNPs increased with decreasing the size of HNPs. The number of the intracellular HNP25 was more than 15-47 times bigger than that of the intracellular HNP125. It was considered that the diameter of NPs was an important factor of the uptake into cells.

To compare the uptake efficiency of the HNPs quantitatively, HNP-treated cells was also measured by the titanium amount *via* ICP. The HNP-treated cells were dealt with HF and HNO_3 in aqueous solution to allow dissolution of titanium. The results show that the mass of titanium per cell is related to the size of HNPs (Figure 18c). Cellular uptake ratio is particle-size-dependent in the order $50 \geq 75 > 100 > 125 > 25$ nm. The uptake of HNP50 was approximately 1.3-1.7 times than that of HNP125. The optimal sizes, 50 and 75 nm, for cell uptake are consistent with the cell uptake of other particles recently reported, which demonstrated that 50-nm glycovirus entered cells *via* receptor-mediated endocytosis more efficiently than smaller NPs.[78] As shown in Figure 18b, the highest rank at the 'number' was HNP25, but the lowest rank was HNP125. The number of internalized HNPs was inverse proportion of particle size. The highest value of 'macromolecule carrying capacity' (MFI value per cell) was the HNP50 in Figure 16. These results may provide the information about the best uptake size for bio-applications such as drug delivery and bioimaging.
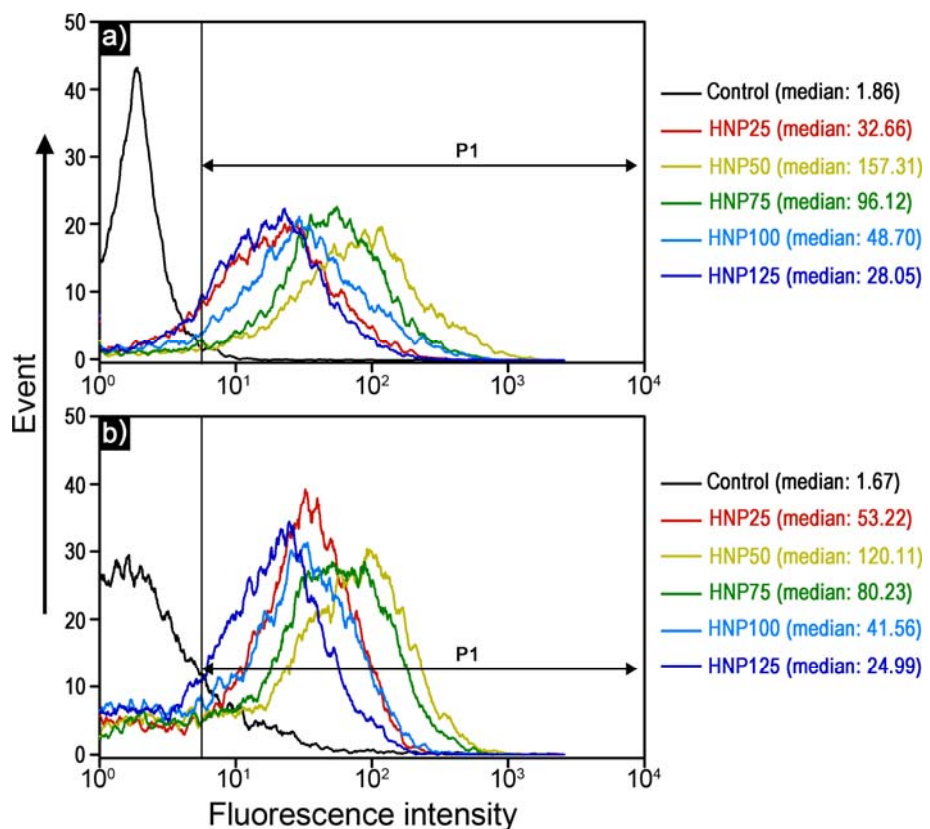
Figure 16. Flow cytometric analysis of (a) SK-BR-3 and (b) J774A.1 cells treated with FITC-HNPs for 24 h.
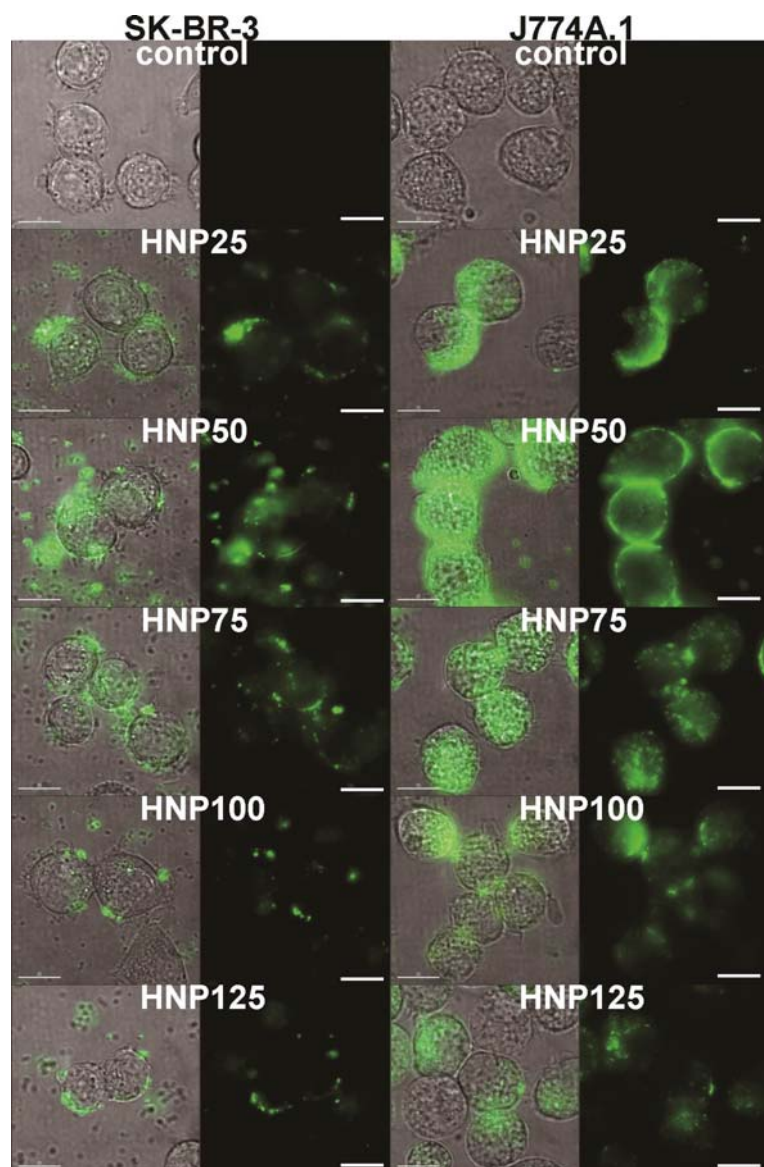
Figure 17. Live cell DIC and fluorescent images of FITC-HNP-treated SK-BR-3/J774A.1 cells (10 µg mL^{-1}); control, HNP25, HNP50, HNP75, HNP100, and HNP125. Scale bars =15 µm.
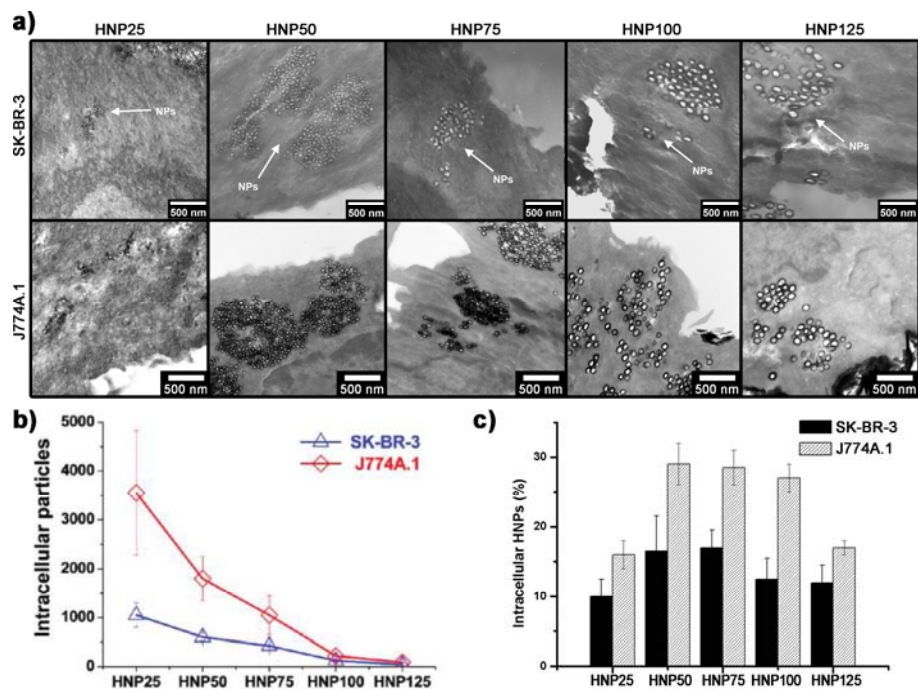
Figure 18. (a) TEM images of HNP-internalized SK-BR-3 and J774A.1 cells. (b) Based on the TEM images, the number of intracellular HNPs was calculated. (c) Quantification histogram of HNP-internalized SK-BR-3 and J774A.1 cells determined by ICP measurement.

The viability with the HNPs was determined using alveolar macrophage J774A.1 cells (Figure 19a). Alveolar macrophages protect the body *via* phagocytosis against airborne nanomaterials through a respiratory route.[79] As a result, nanotoxicity investigation of alveolar macrophage cells could be suitable for comprehending pulmonary nanotoxicology. To evaluate the number of viable cells, the high sensitivity of luminescence-based assay was performed based on the quantification of the ATP concentration. The ATP production of the HNPs represented a size- and concentration-dependent decrease on macrophages. Interestingly, the ATP contents of HNP25-treated cells were slightly larger than that of HNP50, which was correlated to the uptake efficiency of the HNPs. It can be considered that the cell viability of the HNPs was related to their cellular uptake. This was consistent with the findings of Y. Yuan *et al.* that discovered the adverse effect of hydroxyapatite NPs was in order of 45-nm > 26-nm > 78-nm > 175-nm.[80] The viabilities of the HNPs showed over 70% at a loading amount of 100 μg mL^{-1}. There was no significant drop in the viability to macrophages. These cell viability results are related to more immediate NP effects involving ROS production such as photo-activation and electronically active surfaces.[81] Consequently, it is necessary for evaluating the ROS generation of the HNPs toward macrophages compared with cellular viability.

It is known that a small size and large surface area could generate ROS. The nanomaterial characteristics can culminate in ROS generation, which is currently the best-developed paradigm for NP toxicity. H_2DCF-DA staining methods were conducted for 24 h to investigate the role of ROS in cells with the HNPs. In Figure 19b, ROS values were size- and concentration-dependent. Remarkably, the ROS production of the HNP50 on cells was more pronounced than that of other HNPs, and this result was corraborated by cellular uptake and viability results. The ROS production induced by nanomaterials can damage external (membrane) or internal (after nanomaterial uptake) cells and can also attribute to inflammation.[82] In addition, It is known that ROS production and following oxidative stress cause mitochondrial dysfunction, and this could attribute to initiate apoptosis. [83] Therefore, apoptosis in the HNP-treated cells should be evaluated to establish a relationship between oxidative stress and apoptosis.

Apoptosis and necrosis are considered as the most preferred response among various mechanisms for investigating cell death.[65] Figure 65 displays fluorescent images of cells treated with the HNPs in which the cells were stained with aV and PI. Unstained cells define viable cells, and green fluorescent labels/red fluorescent labels are classified as early apoptotic cells/necrotic cells. Dual stained cells are categorized as late apoptotic cells. In

Figure 20, green and red fluorescent dots increased in inverse proportion to the size of HNPs. Some cells treated with HNPs were altered with their own shapes mainly due to disorders in cytoskeletal functions. Taking these facts into account, the apoptosis and necrosis in HNP-internalized macrophages were induced with size-dependent. To quantify apoptotic and necrotic cell death, flow cytometric analysis was conducted. The above-mentioned results were summarized in Figure 21. Viability decreased from 83 (control) to 80, 79, 79, 76 and 76 was observed for and J774A.1 treated with HNP125, HNP100, HNP75, HNP50, and HNP25, respectively, where the decreased viability mainly involved early apoptosis. These data is accordance with other experimental results. It is considered that the toxicity of NPs is related with their cellular internalization efficiency. Although *in vitro* toxicity research cannot exhibit accurate toxicological analysis linked with *in vivo* toxicity, these studies may be expanded to allow the investigation of cellular nanotoxicity pathways as well as the interaction between nanomaterials and cells.
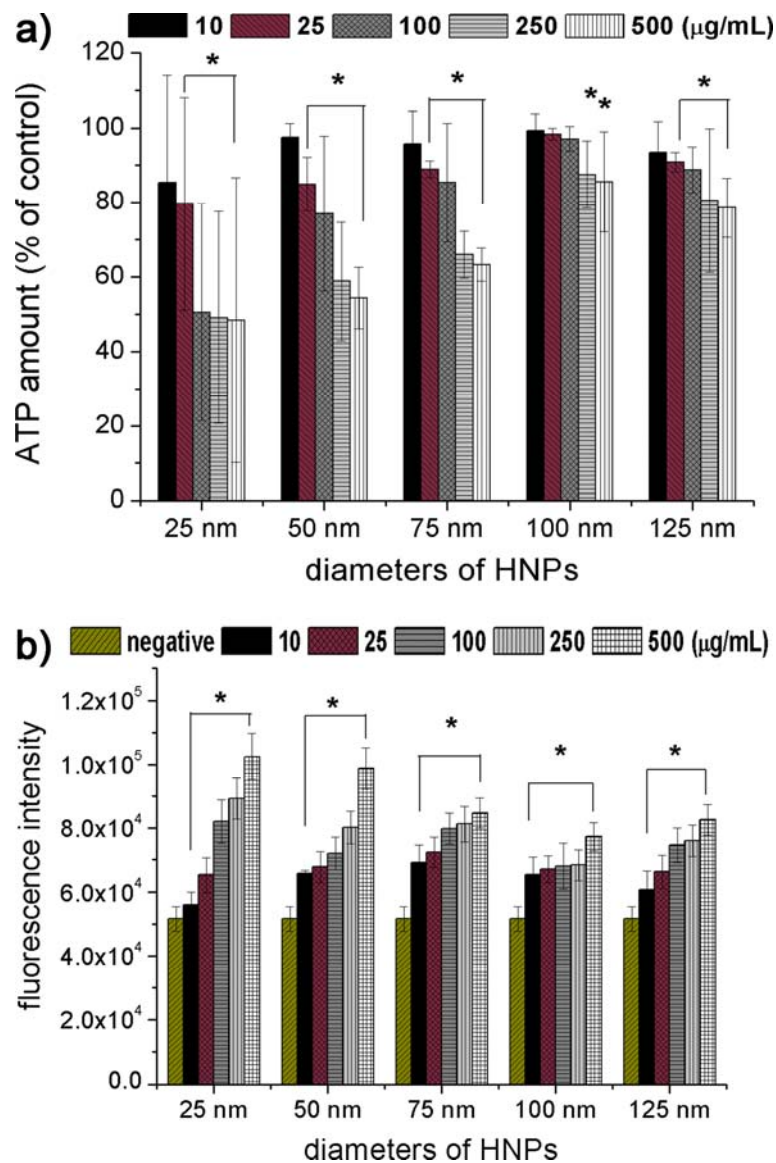
Figure 19. (a) ATP based cell viability of and (b) ROS production by J774A.1 treated with HNPs. J774A.1 was incubated with HNPs as a function of diameters for 24 h. H_2O_2 (0.02%) was used as positive control.
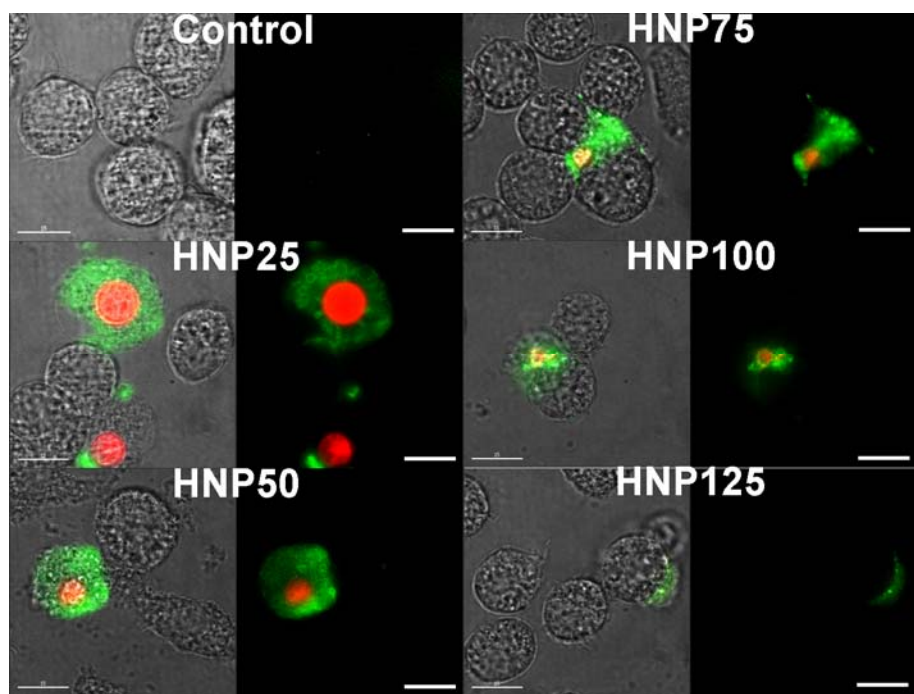
Figure 20. Live cell DIC and fluorescent images of HNP-treated J774A.1 cells (25 μg mL^{-1}). Green (aV) means apoptosis, red (PI) means necrosis. Scale bars: 15 μm.
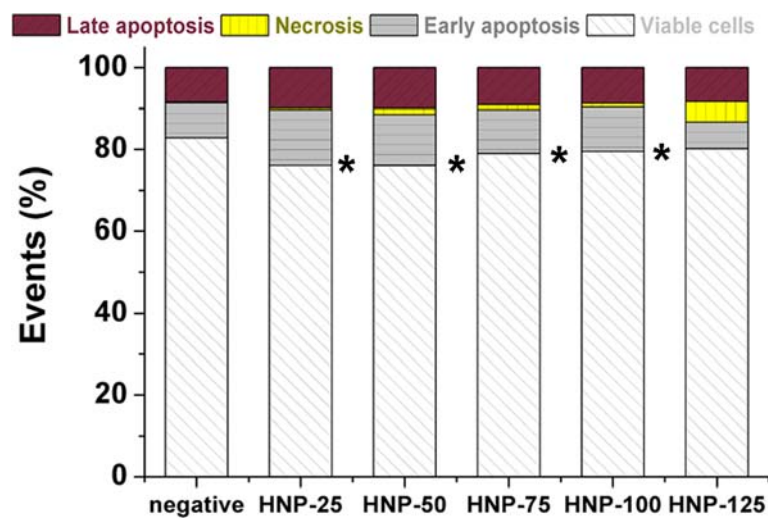
Figure 21. Apoptosis and necrosis ratio obtained from annexin V and PI staining. J774A.1 was incubated with HNPs (25 μg mL^{-1}) for 24 h.

3.1.3. Ba/Sr doped SiO$_2$/TiO$_2$ hollow nanoparticles

3.1.3.1 Fabrication of Ba/Sr doped SiO$_2$/TiO$_2$ hollow nanoparticles

Ba- and Sr-doped silica/titania hollow nanoparticles were prepared by experimental procedures as shown in Figure 22. Silica NPs, prepared by the Stöber method, were first coated with titanium (IV) isopropoxide by sol-gel method.[52] TEM images displayed uniform and monodispersed silica/titania core/shell nanoparticles (CSNP) approximately *ca.* 50 nm in diameter (Si:Ti atomic ratio = 6:4). Resulting CSNPs were treated with hydroxide solutions (0.1 M NH$_4$OH for pristine hollow nanoparticles, 0.2 M Ba(OH)$_2$ for Ba-doped hollow nanoparticles, and 0.15 M Sr(OH)$_2$ for Sr-doped hollow nanoparticles) with sonication for 2.5 h.

We propose a facile fabrication method for alkaline earth metal-doped HNPs by introducing metal hydroxide solutions such as Ba(OH)$_2$ and Sr(OH)$_2$. It is known that metal hydroxide can be doped to silica and titania under the sonication.[84-86] Ba(OH)$_2$ and Sr(OH)$_2$ solutions were used under sonication, resulting in Ba- and Sr-doped HNPs termed Ba-HNP and Sr-HNP, respectively.

Treatment time and the concentration of hydroxide solution are key factors for minimizing particle aggregation. Figure 23 showed the conformational change from CSNP to HNPs as a function of time. After hydroxide solution treatments for 1.5 h, the reduced silica core was observed and the cavity between the core and shell was generated, but unetched silica cores remained.

In the 5 h treatments, the HNPs became aggregated, which may have been due to over-redeposition of etched SiO_2 or TiO_2 on the TiO_2 shell. Therefore, we determined that 2.5 h is the appropriate time for fabricating Ba- and Sr-HNPs without further aggregation. Figure 24a showed TEM images of CSNP treated with diluted hydroxide solutions for 2.5 h. Treated with 10 times diluted $Ba(OH)_2$ and $Sr(OH)_2$, the CSNPs were aggregated and partially etched. The 100 times diluted $Ba(OH)_2$ and $Sr(OH)_2$ were insufficient for etching the silica core and induced bridges between particles. Then, we fabricated HNPs without sonication. Without sonication, the CSNPs were partially etched and formed non-uniform structure (Figure 24b). Therefore, the concentration of hydroxide solution is a key factor for the fabrication of HNPs.

After hydroxide solution treatments, HNPs still exhibited monodisperse hollow structures and uniform diameters of approximately 60 nm. The increased diameter was due to the SiO_2 redeposition process.[52, 75] Although the atomic ratio of p-HNP was 50:50 for Si:Ti, the atomic ratio of Ba- and Sr-HNP was approximately 34:33:33 for Si:Ti:Ba(Sr), respectively, indicating a large amount of Ba and Sr was successfully doped into the Ba- and Sr-HNPs. The combination of the above-mentioned elements can be expected to have significant effect on cell differentiation because each element is known for inducing the differentiation of many cell lines, resulting in a synergetic effect.

Our previous studies showed that the p-HNP has a large inner cavity (diameter: *ca.* 29.2 nm) with a mesoporous shell (porosity: 0.3, diameter of intrawall pore: 3.5 nm).[87] In Figure 25, the nitrogen adsorption isotherm plots of Ba-HNP and Sr-HNP exhibited a type IV hysteresis loop similar to p-HNP. Based on the plots, BET surface area of the p-HNP, Ba-HNP and Sr-HNP were calculated as 310.56 m^2 g^{-1}, 286.74 m^2 g^{-1}, and 228.29 m^2 g^{-1}, respectively. The pore volume of the p-HNP, Ba-HNP and Sr-HNP were 0.83 cm^3 g^{-1}, 0.73 cm^3 g^{-1}, and 0.86 cm^3 g^{-1}, respectively. Regarding the pore size distribution, the large inner cavity was found to be centered on *ca.* 23 nm and the diameter of intrawall pore was *ca.* 3 nm among the three graphs. The pore size (large inner cavity and intrawall pore) of Ba-HNP and Sr-HNP decreased compared to p-HNP, which induced the reduction of BET surface area. However, the characteristic structure of HNP (large inner cavity with mesoporous shell) was retained regardless of hydroxide solution type. These HNP properties offer the potential probability to encapsulate various molecules into the cavity for drug delivery application.
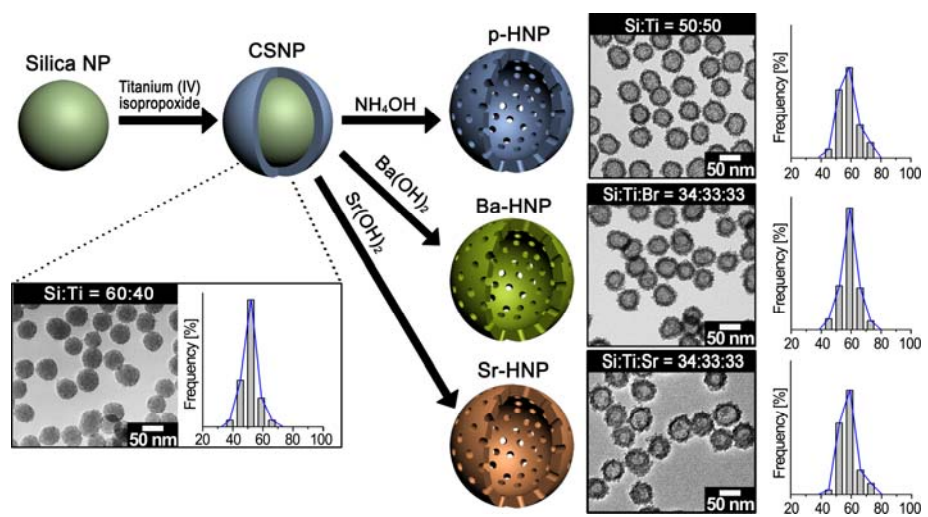
Figure 22. Schematic diagram of fabrication of p-HNP, Ba-HNP, and Sr-HNP and corresponding TEM images and atomic ratios determined by EDX analysis, respectively.
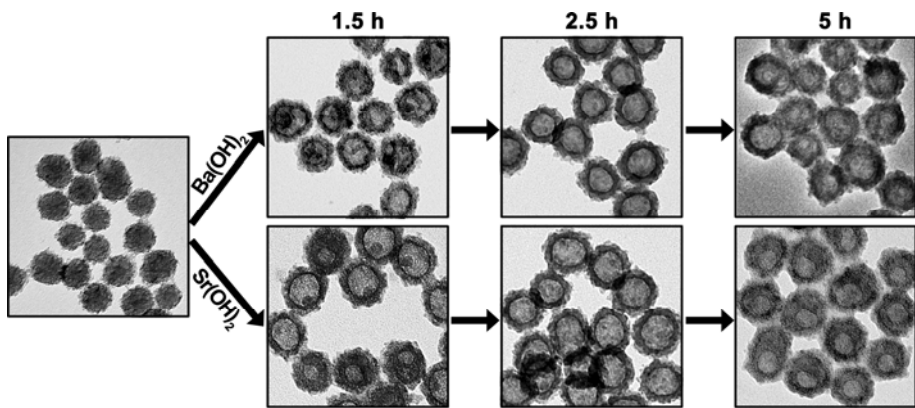
Figure 23. Doping and etching of Ba-HNPs and Sr-HNPs as a function of treatment time. Under sonication, barium hydroxide and strontium hydroxide etched silica core as well as deposited on the shell.
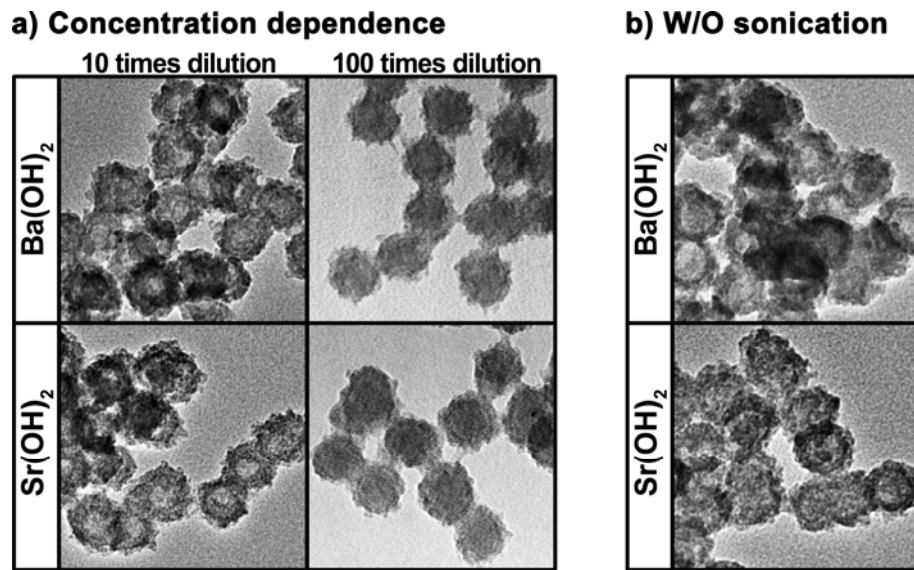
Figure 24. (a) Doping and etching of Ba-HNPs and Sr-HNPs as a function of hydroxide solution concentration. (b) Fabrication of Ba-HNP and Sr-HNP without sonication.
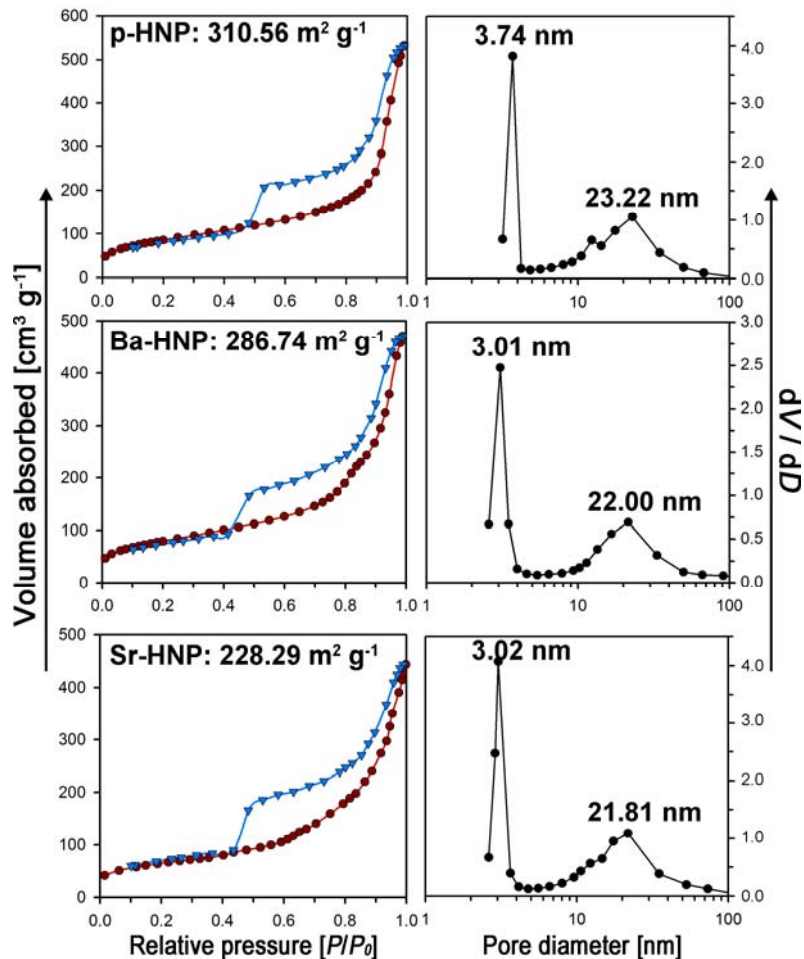
Figure 25. Nitrogen adsorption isotherm plots and the pore-size distribution of the HNPs. The surface area and pore size were calculated by BET methods and BJH methods, respectively.

Figure 26 represents STEM elemental mapping images of HNPs showing the actual distribution of O, Si, Ti, Ba, and Sr in the HNPs. The mapping images indicated Ba and Sr were successfully doped on the hollow NPs as well as silicon and titanium were doped on the hollow NPs. Based on these results, it could be concluded that Si, Ti, O, and Ba/Sr formed a hybrid structure in the HNPs. In X-ray diffraction patterns, the HNPs had no obvious peaks due to their low reaction temperature, indicating an amorphous nature of HNPs (Figure 27). X-ray photoelectron spectroscopy (XPS) was conducted to further clarify the molecular structure of the HNPs (Figure 28). Si 2p spectrum of the p-HNP had a SiO_2 signal at 103.6 eV, while Ba- and Sr-HNP displayed both silica (103.6 eV; green) and silicate (102.6 eV; blue) signals. The Ti 2p spectra in Ba- and Sr-HNPs were deconvoluted into titania (459.1 eV and 465.14 eV; green) and titanate (458.4 eV and 463.9 eV; red) unlike p-HNP. The silicate (blue) and titanate (red) were also confirmed by Ba 3d and Sr 3d curves. Therefore, the HNPs were composed of silica, titania, silicate, and titanate; p-HNP (SiO_2 and TiO_2), Ba-HNP (SiO_2, TiO_2, $BaSiO_3$, and $BaTiO_3$), and Sr-HNP (SiO_2, TiO_2, $SrSiO_3$, and $SrTiO_3$). Barium and strontium hydroxide treatments contributed to the doping of these elements (Ba and Sr) on p-HNP as a form of silicate ($BaSiO_3$/$SrSiO_3$) and titanate ($BaTiO_3$/$SrTiO_3$).
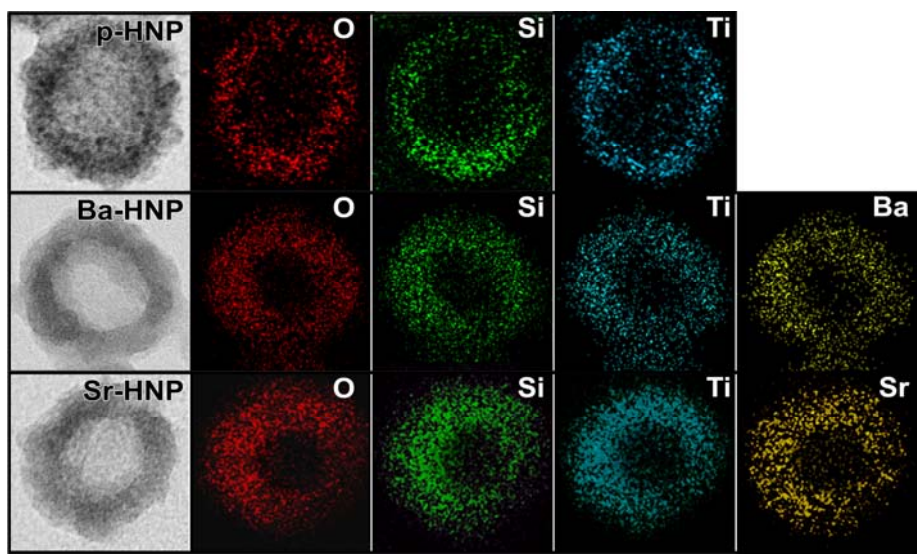
Figure 26. STEM elemental mapping images of p-HNP, Ba-HNP, and Sr-HNPs.
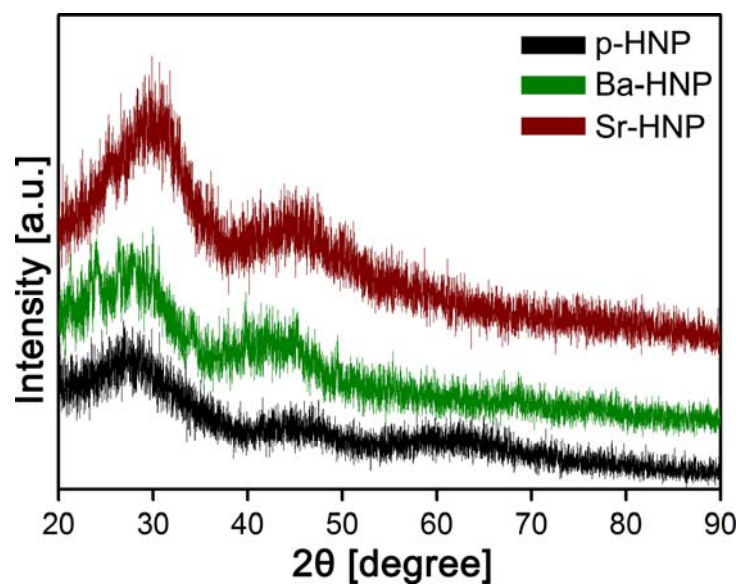
Figure 27. XRD spectra of HNPs
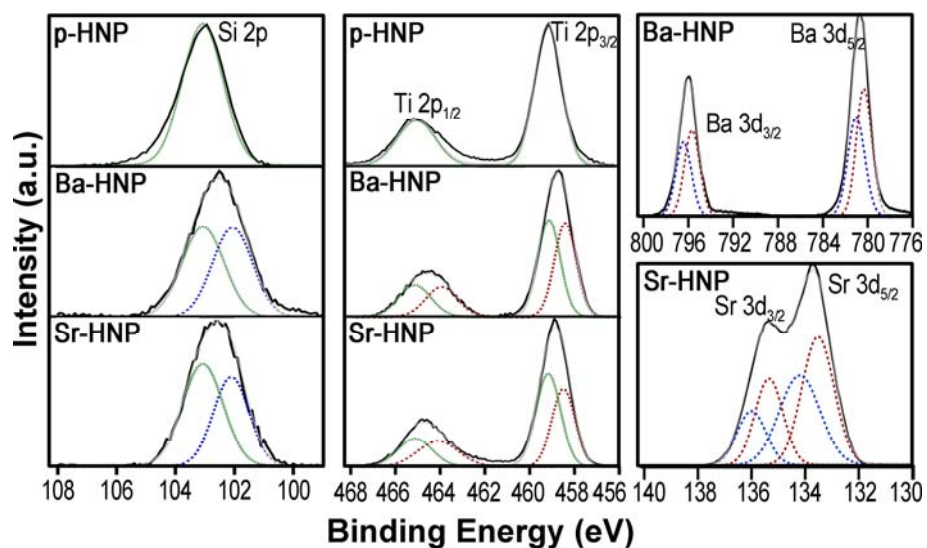
Figure 28. XPS spectra of p-HNP, Ba-HNP, and Sr-HNPs (from left to right: Si 2p, Ti 2p, Ba 3d, and Sr 3d spectra; deconvoluted components-green: SiO_2 or TiO_2; blue: $BaSiO_3$ or $SrSiO_3$; red: $BaTiO_3$ or $SrTiO_3$).

On the basis of experimental data, we proposed a possible fabrication mechanism of the metal-doped HNPs using a metal hydroxide solution (Figure 29). When the metal hydroxide solution was mixed in the CSNP solution, metal ions diffused to the CSNPs though the porous TiO_2 shell as well as OH^- ions. Under the basic condition, SiO_2 core was dissolved by weakening the siloxane bonds and generated $[Si(OH)_6]^{2-}$ by coordination to OH^- ions.[75] The resulting $[Si(OH)_6]^{2-}$ encountered the metal ions and was redeposited on the surface of the porous TiO_2 shell as a form of M_xSiO_3 under the high temperature and pressure generated by sonication.[84] The TiO_2 also reacted with OH^- ions and metal ions and formed $[Ti(OH)_6]^{2-}$ and M_xTiO_3 during the sonication process.[37, 85, 86] However, the reactivity of SiO_2 was much higher than TiO_2, resulting in a SiO_2/TiO_2 hollow nanostructure.[75] Formation energy of M_xSiO_3 and M_xTiO_3 was supplied by sonication irradiation that induced a concentrated local heating in the collapsing bubble and acoustic cavitation.[75] Using these methods, alkali-earth-metal-doped hollow NPs could be readily fabricated without further treatment.
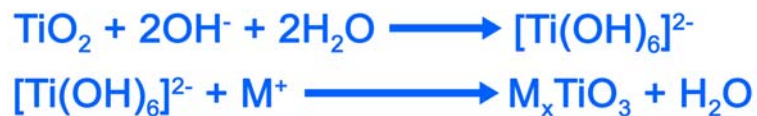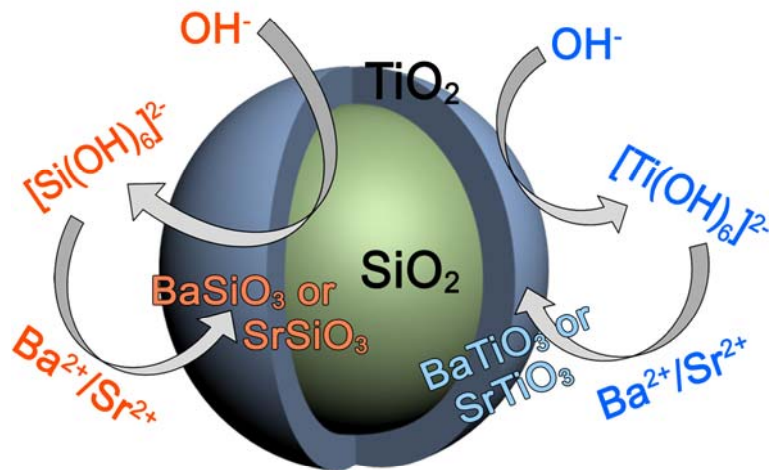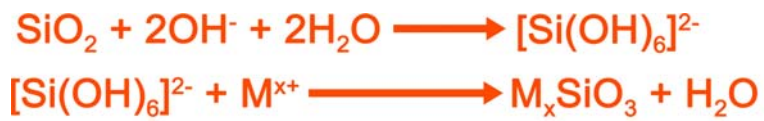
Figure 29. Proposed mechanism of Ba-HNP and Sr-HNPs using metal hydroxide solution.

3.1.3.2 Application for neuronal differentiation

Using PC12 cells as a model cell, the effect of HNPs on mammalian neuronal differentiation was investigated. Figure 30a-c shows enhanced neuronal differentiation by NGF+HNPs (cells were treated with HNPs and NGF) compared with NGF-only-treated cells. Morphological changes in PC12 cells were facilitated by increasing the treatment time and the concentration of HNPs. The neurites were the most extended when the highest dose of Sr-HNP was introduced into PC12 cells in cooperation with NGF at day 3.

Based on the immunofluorescent images, the number of neurite-bearing cells (differentiation efficiency) and average neurite length were calculated using ImageJ software. Differentiation efficiency and neurite lengths were in proportion to the HNP concentration as well as treatment time (Figure 30d). HNPs exhibited almost identical differentiation efficiency within the margin of error, which was 1.5 times higher than that of NGF-only-treated cells. Although improved by HNPs compared to NGF-only-treated cells, the differentiation efficiency of PC12 cells was independent of the HNP type. Notably, the average neurite length was affected by HNP type, unlike differentiation efficiency. The average neurite length was in the order of Sr-HNP+NGF > Ba-HNP+NGF > p-HNP+NGF > NGF in all ranges of particle concentrations. Average neurite length of p-HNP, Ba-HNP, and Sr-HNP (25 μg

mL^{-1}) treated cells for day 1 increased 2, 2.5, and 3.1 times higher, respectively, than NGF-treated cells. After 3 days of treatment, neurites still extended 1.94, 2.46, and 2.78 times longer in p-HNP, Ba-HNP, and Sr-HNP treated cells, respectively. The differentiation efficiency was also two times higher than treatment with NGF alone. Previous studies indicated that strontium, BaTiO$_3$, and silicate nanoplate facilitated the differentiation of osteoblasts.[34, 37, 38, 88] Furthermore, TiO$_2$ enhanced neuronal differentiation.[89] Judging from these data, doped Sr/Ba and SiO$_2$/TiO$_2$ in the NPs played different roles in facilitating neuronal differentiation. While SiO$_2$/TiO$_2$ increasingly affected both the differentiation efficiency and neurite length, doped Sr/Ba influenced on the additional elongation of average neurite length. Collectively, the synergetic effects of doped Sr/Ba, TiO$_2$/SiO$_2$ may elevate the neuronal differentiation, and HNPs exerted a significant impact on the differentiation not only at the early stage but at the mature stage of differentiation. To the best of our knowledge, this is the first investigation on the promoting effects on neuronal differentiation by Ba and Sr doped nanomaterials. Additionally, these synergetic effects of doped Sr/ Ba and TiO$_2$/SiO$_2$ have not been reported before.
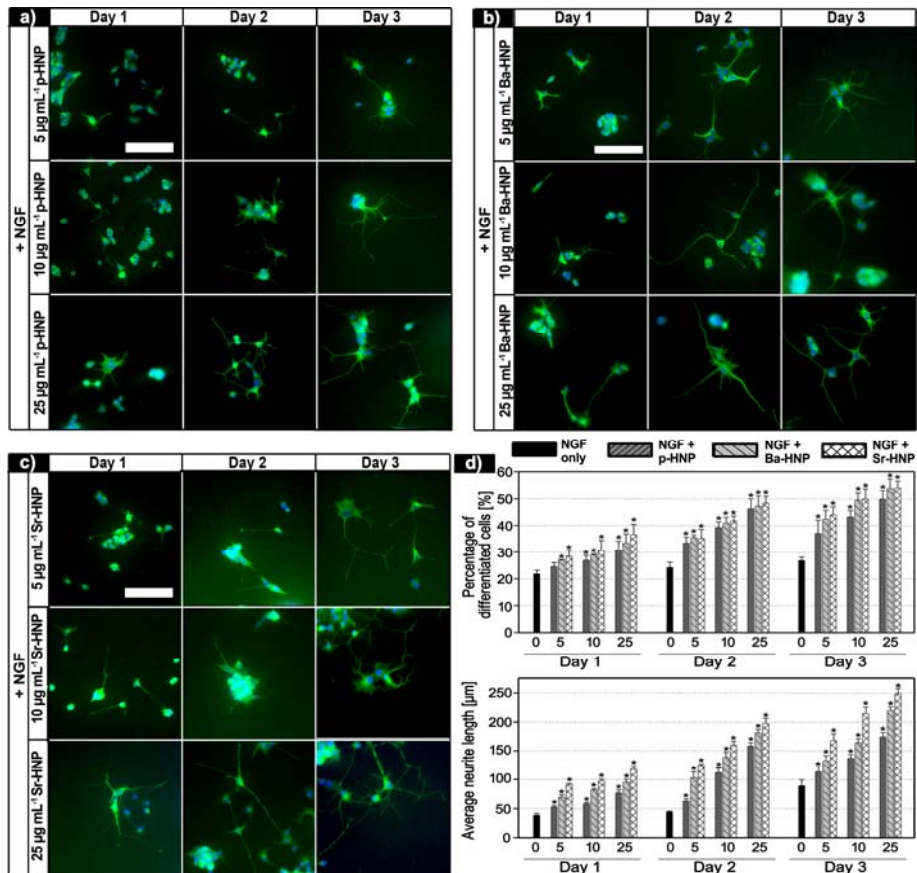
Figure 30. Neuronal response to HNPs on PC12 cells. (a-c) Immunofluorescent images of cells treated with NGF (100 ng mL^{-1}), 0.1% BSA, and the HNPs. The cells were stained with β-tubulin (green) and DAPI (blue). (d) Differentiation efficiency of and average neurite length of the cells. The X axis indicates the concentration of the HNPs.

To compare stimulating ability for neurite outgrowth, control experiments were conducted in PC12 cells (Figure 31). In the absence of NGF, neither neurites nor morphological changes were observed with any HNP treatment. Additionally, β-tubulin in the NGF-absent samples was less expressed than in NGF-treated samples. Therefore, HNPs could not activate directly, but could promote the differentiation pathway in cooperation with NGF.

Figure 32 shows that HNPs were localized in endosomes and lysosomes without aggregation. The local pHs inside the endosomes and lysosomes were pH 5.5 and pH 4.5, respectively, which may have induced partial ionization of HNPs and released metal ions into the cytosol.[43] To confirm this hypothesis, leached metal ions were quantified by inductively coupled plasma mass spectrometry (ICP-MS) in a lysosomal buffer solution (Figure 33). Approximately 25% of barium and 26% of strontium were leached from the Ba-HNP and Sr-HNP on day 1, respectively. In contrast to lysosomal buffer solutions, less than 0.2% of the barium and strontium ions were dissolved in phosphate buffered solution (PBS) (pH 7.4) on day 3. In the case of titanium, no ions were dissolved in either solution. The dissolved Ba and Sr ions induced the differentiation and simultaneously potentially caused reactive oxygen species (ROS) production.[89] Figure 34a represents the ROS generated in proportion to the concentration of HNPs and treatment time. Regarding HNP

type, the amount of intracellular ROS was in the order of Sr-HNP+NGF > Ba-HNP+NGF > p-HNP+NGF > NGF, which was corroborated by the above-mentioned differentiation results. Therefore, the intracellular ROS caused by HNPs, at least in part, contributed to facilitating the neuronal differentiation as messenger molecules.

Although ROS act as messenger molecules, excessive ROS can stimulate inflammation as well as initiate apoptotic cell signaling.[81] The viability of HNP-treated cells should be assessed for further applications (Figure 34b). At 25 μg mL^{-1} for 1 day, viabilities of the PC12 cells were 97.7%, 95.6%, and 93.0% for p-HNP, Ba-HNP, and Sr-HNP, respectively. A previous report demonstrated the viability of SK-BR-3 cells treated with 25 μg mL^{-1} p-HNP was 95% for 1 day, which implies no significant effect of HNPs on viability.[90] In addition, the lowest viability was 89.0% when the PC12 cells were treated with 25 μg mL^{-1} Sr-HNP for 3 days. Hence, HNPs can be considered as low toxic materials and are appropriate for biomedical applications.
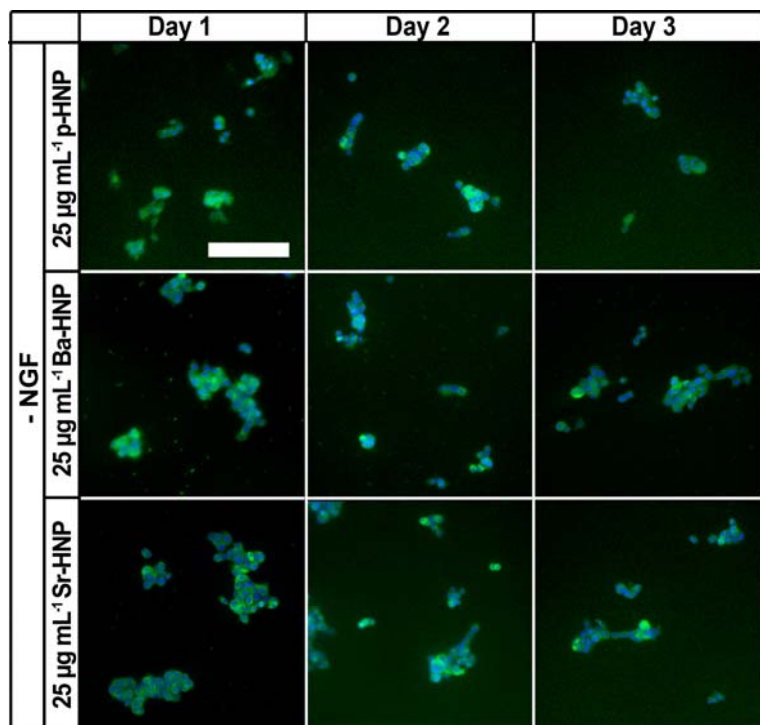
Figure 31. Control experiments as a function of time. Immunofluorescent images of cells treated with 0.1% BSA and the HNPs (25 µg mL^{-1}). The differentiated PC12 were immunostained with β-tubulin (class III; neural specific marker; green) and DAPI (nucleus; blue).
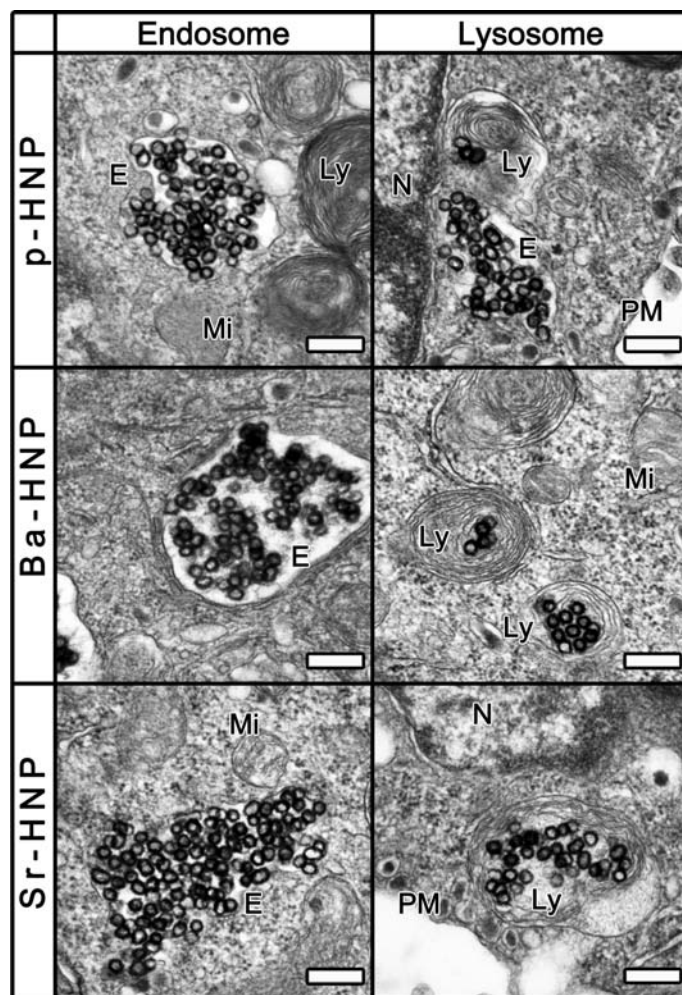
Figure 32. TEM images of HNP-treated PC12 for 24 h. Abbreviations: N as nucleus; PM as plasma membrane; Mi as mitochondria; E as endosome; Ly as lysosome.
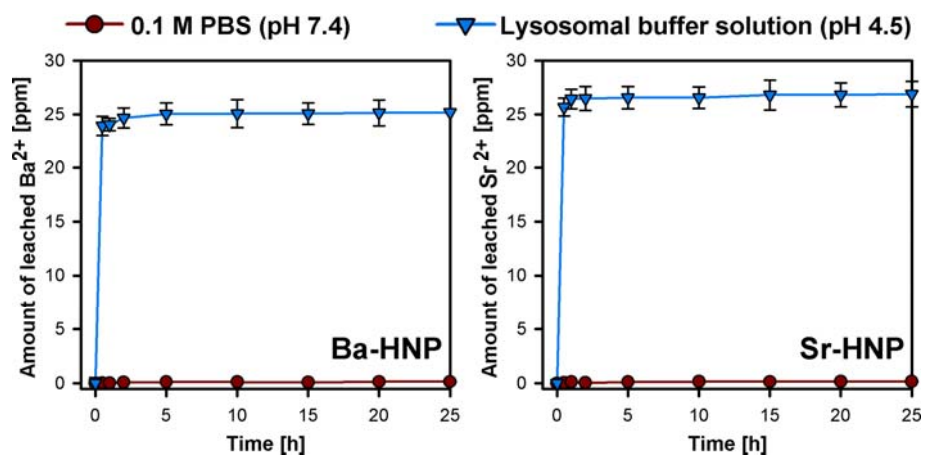
Figure 33. Leaching profile of Ba^{2+}, and Sr^{2+} ions from Ba-HNPs and Sr-HNPs in high ionic strength solution (0.1 M PBS, pH 7.4) and lysosomal buffer solution (pH 4.5).
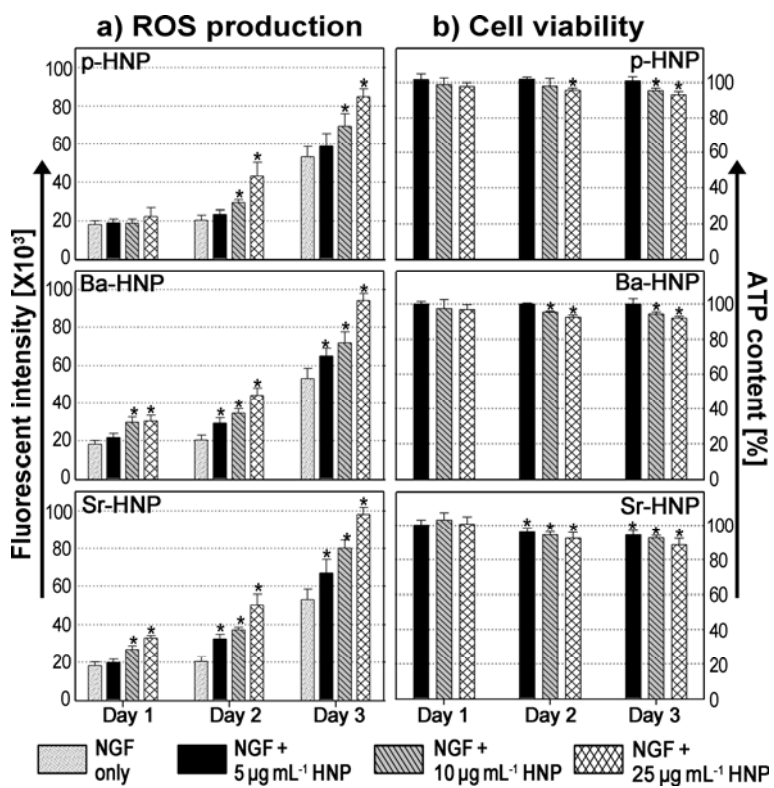
Figure 34. (a) ROS production of and (b) viability of the PC12 cells treated with HNPs. The experiments were conducted with dose dependence and time dependence.

To elucidate the signal transduction pathways stimulated by resulting ROS from HNPs, we first focused on mitogen-activated protein kinase (MAPK) signaling cascades including c-Jun N-terminal kinases (JNK), protein kinase 38 (p38), and extracellular-signal-regulated kinases (ERK1/2). Excessive ROS may activate JNK, p38, and ERK1/2 *via* phosphorylation.[91] Phosphorylated proteins can translocate into the nucleus and then turn on specific genes regulating cell differentiation.[43] The expression levels of phosphorylated p38 (pp38), phosphorylated JNK (pJNK), and phosphorylated ERK1/2 (pERK) were measured using flow cytometry (Figure 35a). Compared to NGF-only-treated cells, JNK were more phosphorylated by *ca.* 4.4% in NGF+HNP treated cells, regardless of HNP type. Contrary to pJNK, in pp38 and pERK, the apex of both graphs shifted to the right in the order of NGF, p-HNP+NGF, Ba-HNP+NGF, and Sr-HNP+NGF. These results were respectively consistent with the above-mentioned data; pJNK results for differentiation efficiency with HNP type independence, and pp38/pERK results for average neurite length with HNP type dependence. Considering these data, p-HNP induced three types of MAPK signaling cascades, and the Ba-HNP and Sr-HNP influenced additional ERK and p38 MAPK signaling relevant to neurite outgrowth, which explains why the average neurite lengths were different among HNPs even though the differentiation efficiency was similar. (Figure 35b)

Other signaling pathways, such as activated phosphatidylinositol 3-kinase (PI3K)/Akt, can also be involved in neurite outgrowth but to varying degrees dependent on the cell type and other factors.[92] In PC12 cells, NGF binds to NGF-specific receptor TrkA, which then activates PI3K/Akt signal transduction *via* phosphorylation.[92] The expressions of TrkA and phosphorylated Akt (pAkt) were also analyzed, but no substantial improvement was observed after HNP treatments (Figure 35a). Collectively, this finding reveals that enhanced neuronal differentiation by HNPs was originated from MAPK signaling cascades, but not the TrkA/Akt pathway.

To induce neuronal differentiation *in vitro*, periodic NGF addition is necessary. However, even if a large amount of NGF is inserted, only a small fraction reaches the cell due to Brownian movement.[93] HNPs has a large inner cavity with a mesoporous shell, offering the possibility to encapsulate molecules into the cavity for drug delivery application. Hence, to deliver NGF into cells efficiently, HNPs were further applied to load NGF. To separate from the case that cells were treated with HNPs and NGF, these abbreviations were used; NGF+HNP means that cells were treated with HNPs and NGF, and NGF-HNPs implies that cells were treated with NGF encapsulated HNPs (NGF-p-HNP, NGF-Ba-HNP, and NGF-Sr-HNP, respectively). These NGF-HNPs makes PC12 cells differentiate directly without NGF daily insertion.

For precise comparison, 100 ng mL^{-1} NGF was loaded in 25 µg mL^{-1} NGF-HNP, which is the same concentration used in the experiments in Figure 30 (100 ng mL^{-1} NGF were daily injected). Release profile of NGF from NGF-HNPs, analyzed in Figure 36, was dependent on the solvent type. In 0.1 M PBS, NGF was released only *ca.* 5 and 10% after 1 h and 24 h, respectively, due to the hydrophobicity of NGF.[93] However, in DMSO, about 83 and 91% NGF was released after 1 h and 24 h incubation, respectively. This result demonstrated that HNP could effectively load NGF inside of the HNP, deliver them without leakage, and release them after cellular internalization.

Figure 37 illustrates that the neurites were more generated and extended in NGF-HNP treated cells than NGF-only-treated or HNP+NGF treated cells. Additionally, NGF-HNPs directly induced neuronal differentiation of PC12 cells without additives. Based on the images, differentiation efficiency and their average neurite lengths were calculated. Differentiation efficiency and their neurite lengths were in proportion to the NGF-HNP concentration as well as treatment time, showing the same tendency as in HNP-treated cells (Figure 30). The NGF-HNPs showed increased differentiation effectiveness compared to HNP+NGF. When the cells were treated with NGF-Sr-HNP for 3 days, differentiation efficiency was 67.47 ± 4.88%. In case of treatment with HNP+NGF, the highest differentiation efficiency was 54.05 ± 2.54%.

Differentiation efficiency in NGF-HNP treated cells were enhanced on average 2.53 times more than NGF-only-treated cells, an average of 1.15 times higher than HNP+NGF treated cells. In case of average neurite length, the highest values were 339.14 ± 26.64 and 248.95 ± 8.88 for NGF-Sr-HNP and Sr-HNP+NGF, respectively. NGF-HNPs facilitated the neurite extension by *ca.* 1.26 times compared to HNP+NGF. Even without daily addition of NGFs, neuronal differentiation was promoted more by NGF-HNP than HNP with a daily addition of NGFs. These results suggested that NGF were successfully delivered into cells using HNPs; hence NGF encapsulated HNPs were highly effective for inducing neuronal differentiation *in vitro.*

Chen and colleagues reported that the differentiation efficiency was 50% in PC12 cells treated with NGF+10 µg mL^{-1} short multiwall carbon nanotubes for 7 days.[94] At an even shorter treatment time (3 day), the cells were 1.3 times more differentiated under NGF-Sr-HNP treatments. When the cells were treated with NGF+25 µg mL^{-1} MnO$_2$/PEDOT NP for day 3, 60% of cells were differentiated and average neurite length was 128 µm (Figure 43 and 44). The differentiation efficiency and average neurite length from NGF-Sr-HNP treated cells were approximately 1.1 and 2.7 times higher, than cells treated with NGF+MnO$_2$/PEDOT NPs. Thus, NGF loaded HNPs were significantly efficient for promoting neuronal differentiation compared to previous systems.
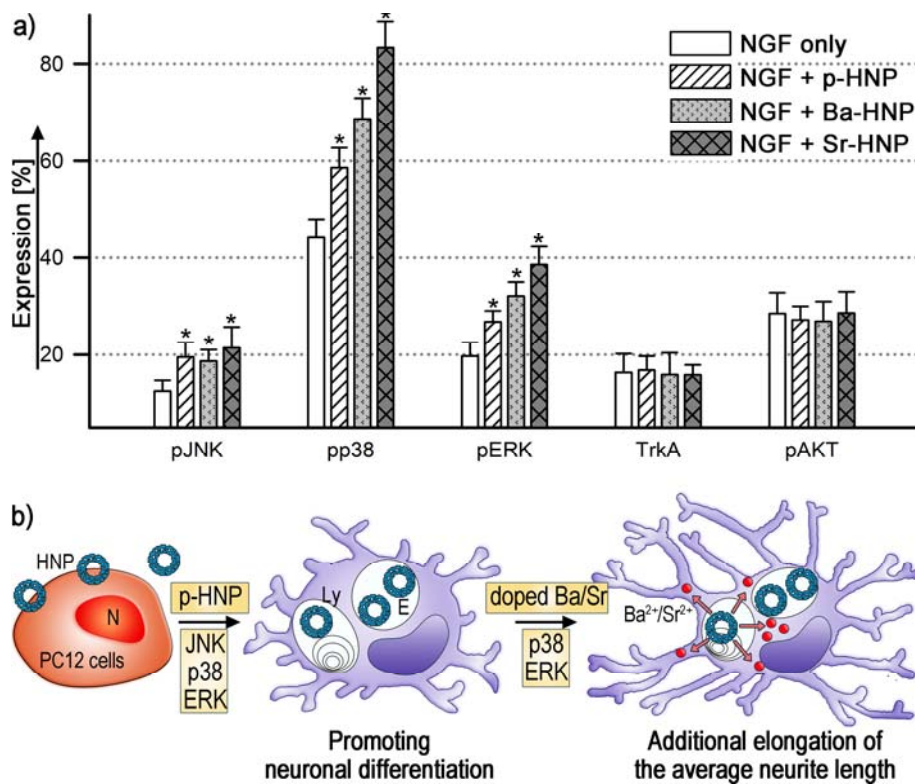
Figure 35. (a) Effects of HNPs on the signaling pathway of PC12 for day 3. For all experiments, cells were treated with NGF (100 ng mL^{-1}), 0.1% BSA, and 25 μg mL^{-1} HNPs. (b) Proposed mechanism of promoting effects of HNPs on the neuronal differentiation. Abbreviations: N as nucleus; E as endosome; Ly as lysosome.
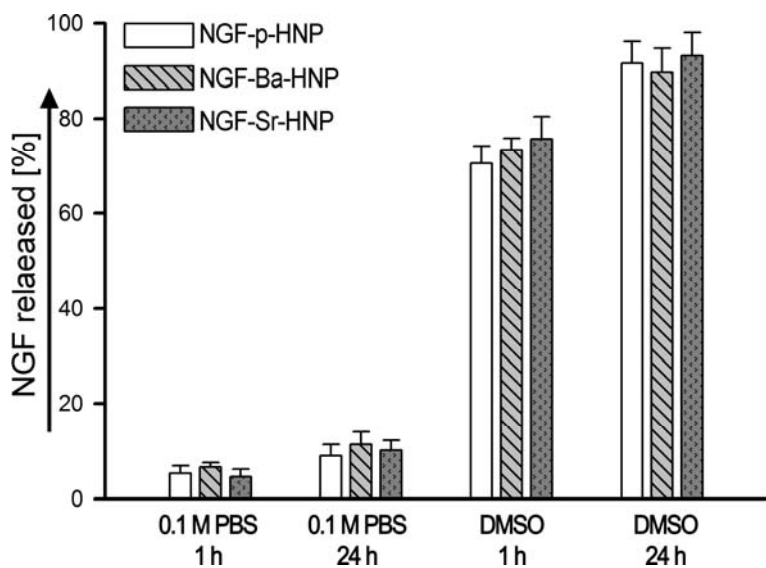
Figure 36. Time-dependent release profile of NGF from NGF-HNPs into 0.1 M PBS and DMSO.
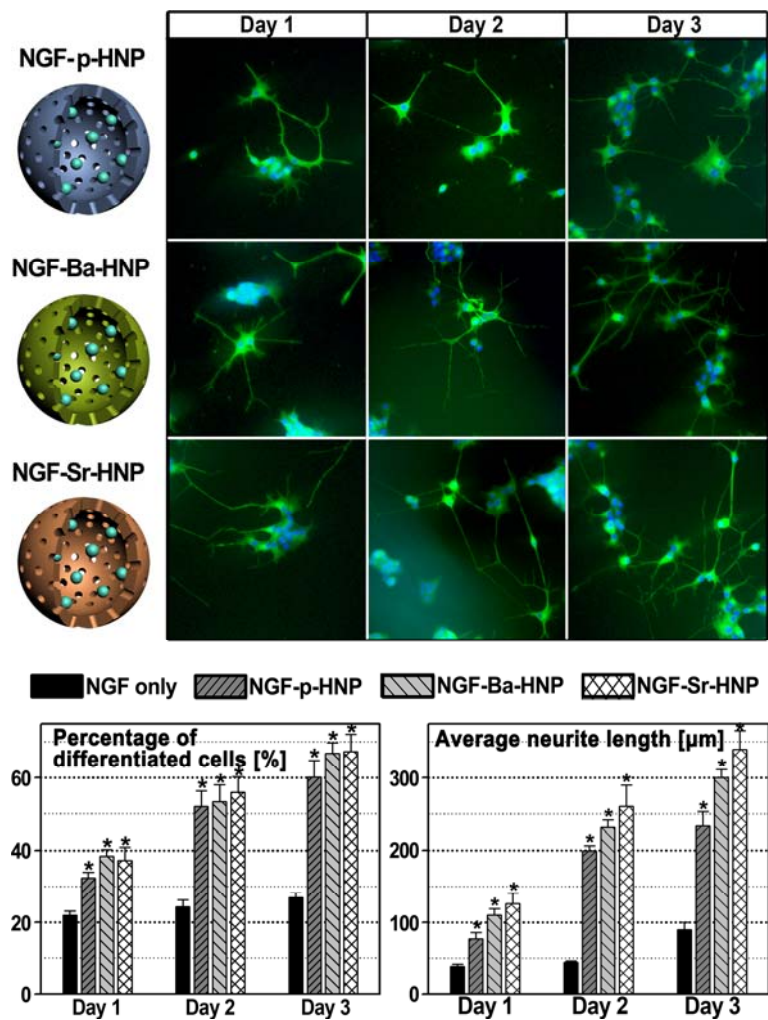
Figure 37. Neuronal response to NGF-HNPs on PC12 cells. Immunofluorescent images of cells treated with 0.1% BSA and 25 μg mL^{-1} NGF-HNPs. The cells were stained with β-tubulin (class III; neural specific marker; green) and DAPI (nucleus; blue).

3.2. PEDOT based hybrid nanoparticles

3.2.1. MnO$_2$ decorated PEDOT nanoparticles

3.2.1.1 Fabrication of MnO$_2$ decorated PEDOT nanoparticles

Figure 38 shows a schematic diagram of the experimental procedure. PEDOT nanoparticles (PEDOT NPs) were synthesized in reverse cylindrical micelle phases by chemical oxidation polymerization.[5, 53] Briefly, sodium bis(2–ethylhexyl) sulfosuccinate (AOT) formed reverse micelles in hexane, and FeCl$_3$ solution was introduced into the AOT/hexane system. Iron cations were adsorbed on the head groups of AOT and acted as oxidizing agents for the chemical polymerization of 3,4–ethylenedioxythiophene (EDOT) monomers at the cylindrical AOT/water interface. The PEDOT NPs were washed with ethanol and resuspended in water. TEM images revealed uniform, ellipsoidal shaped, and dispersed PEDOT NPs of almost 55–nm–width and 160–nm–length (Figure 38, inset). Subsequently, the PEDOT NPs were treated with 10 mM potassium permanganate solution (KMnO$_4$) under stirring conditions. MnO$_2$–decorated PEDOT (MnO$_2$/PEDOT) NPs were formed by reaction between the oxidant and the reductant.[54, 95] Afterward, the MnO$_2$/PEDOT NPs were washed with deionized water, resuspended in 0.1 M PBS solution, and applied to PC12 cells to promote neuronal differentiation. Energy–dispersive X–ray (EDX) map of the MnO$_2$/PEDOT NPs indicated successful

incorporation of MnO_2 on the surface of the PEDOT NPs (Figure 38a, inset; red, S; green, Mn). The green dots were mixed with red dots, indicating that the MnO_2 and PEDOT formed a hybrid structure on the surface of PEDOT NPs. The color of the $KMnO_4$–treated PEDOT NPs was changed from pale blue to yellowish green as a function of time due to the formation of the brownish–colored MnO_2 (Figure 39).[54] Upon adding the purple $KMnO_4$, the solution immediately changed from blue to purple due to the MnO_4^- ions.[96] As MnO_2 domains grew, MnO_4^- ions in the solution were consumed, and the purple color became completely bleached, resulting in the brown color.

To confirm the presence of MnO_2 domains on the PEDOT, HRTEM analysis was conducted. In Figure 40a, MnO_2/PEDOT NPs retained their shape. The dark spots in Figure 40a and b imply the presence of MnO_2 domains and show that each domain was less than 5 nm in size. The MnO_2 domains had no lattice fringes because of the low reaction temperature,[54] indicating the nature of the MnO_2 is amorphous. The amount of decorated MnO_2 domains on the PEDOT was calculated as 8.8 wt% by ICP analysis. To further clarify the oxidation state of the MnO_2 domain, XPS analysis was conducted (Figure 40c). The peaks of Mn $2p_{3/2}$ and Mn $2p_{1/2}$ were centered at 642.0 and 653.3 eV, respectively, which is considered that most of the MnO_4^- ions in the solution were reduced to MnO_2 domains on the surface of the PEDOT matrix.[54, 95]

117
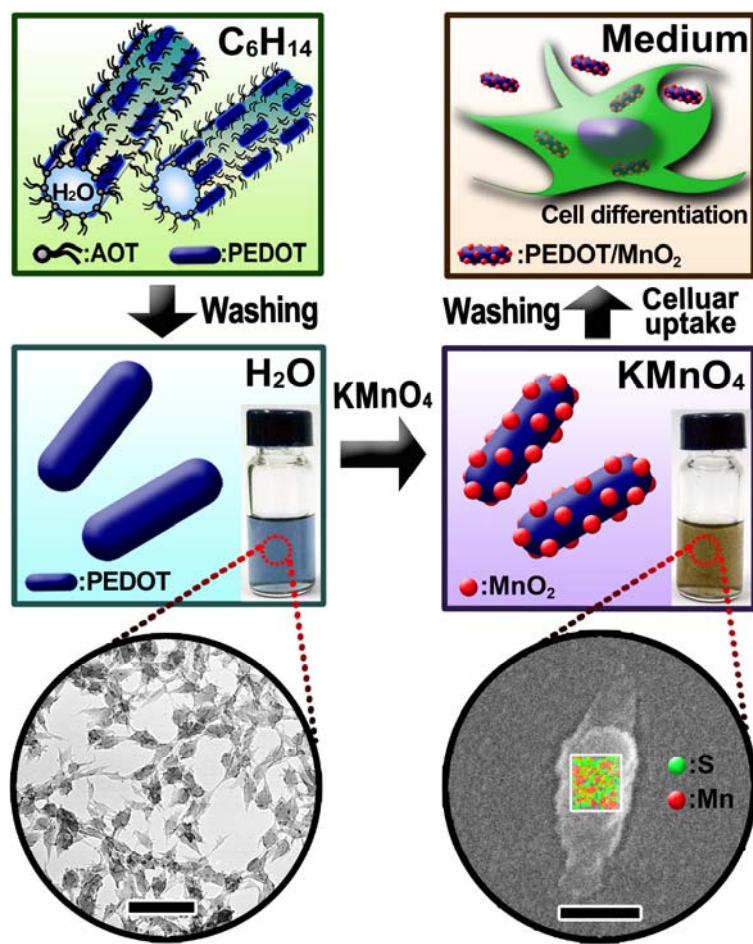
Figure 38. Schematic diagram of fabrication of the MnO_2/PEDOT NPs (left inset: enlarged TEM image of the PEDOT NPs, Scale bar: 200 nm; right inset: enlarged FE–SEM image of MnO_2/PEDOT NPs with EDX mapping, Scale bar: 50 nm).
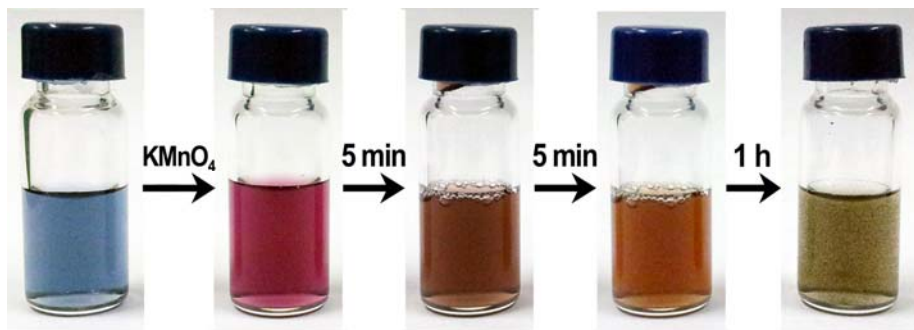
Figure 39. Photographs of time–dependent color alteration of 10 mM KMnO$_4$–treated PEDOT NPs.
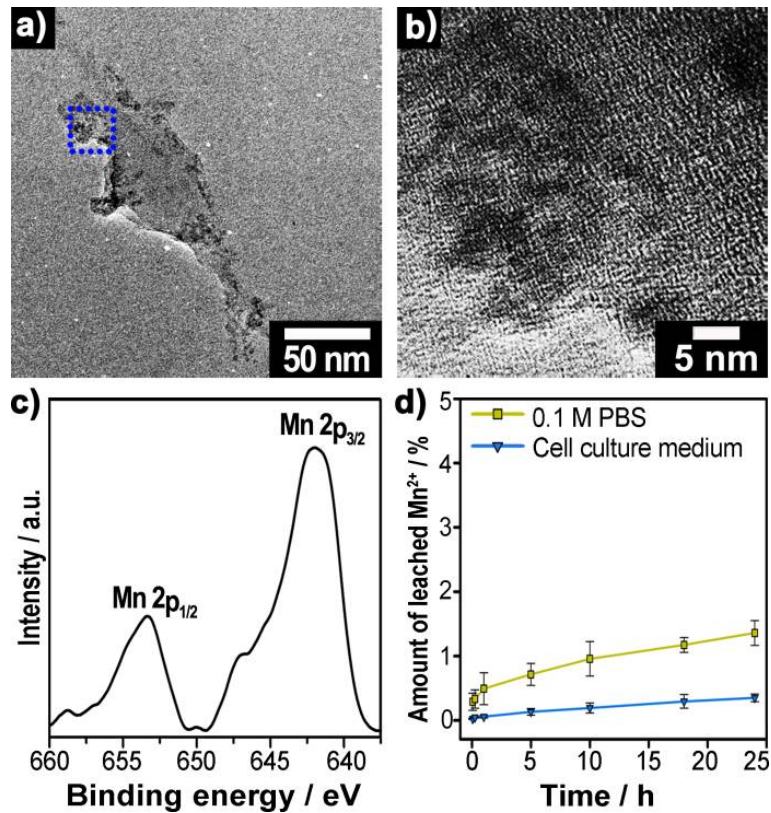
Figure 40. (a) HRTEM image of MnO$_2$/PEDOT NPs and (b) magnified image of boxed area in (a). (c) XPS spectrum of MnO$_2$/PEDOT NPs. The PEDOT NPs were treated with 10 mM KMnO$_4$ for 10 min. (d) Leaching profile of Mn^{2+} ions from MnO$_2$/PEDOT NPs in high ionic strength solution (0.1 M PBS) and cell culture medium.

After the formation of MnO$_2$ domains, the zeta potential of the MnO2/PEDOT NPs increased from -27.48 ± 1.85 to -30.9 ± 1.02 mV in aqueous solution because the negative surface charge of the MnO$_2$ domains affected on the zeta potential of the MnO$_2$/PEDOT NPs.[97] Dissolution of the Mn^{2+} ions was evaluated in 0.1 M PBS and cell culture medium as a function of a time (Figure 40d). A small amount of Mn^{2+} ions (0.34%) was leached in cell culture medium during 24 h incubation due to colloidal stability effects of solvents.[60]

To investigate MnO$_2$ formation on the PEDOT NPs, the molecular structure of PEDOT NPs was analyzed by XPS. The XPS spectra of S 2p can be deconvoluted into three components: sulfide (164.1 eV; blue), sulfoxide (165.1 eV; red), and sulfone bonds (168.2 eV; green) (Figure 41a and b).[53, 54] The sulfoxide and sulfone bonds in pristine PEDOT NPs were attributed to the incorporation of the sulfonate anionic head group of residual AOT surfactant, as the PEDOT nanomaterial was fabricated on the surface of AOT micelle templates.[53] After KMnO$_4$ treatment, the sulfoxide and sulfone bonds in MnO$_2$/PEDOT NPs increased compared with those in PEDOT NPs. It is considered that the sulfide bonds in PEDOT NPs were transformed into sulfoxide and sulfone bonds during the KMnO$_4$ treatment.

These results were confirmed by FT–IR spectra of PEDOT NPs treated

with different concentrations of KMnO$_4$ (Figure 41c). Characteristic peaks, including S=O stretching bond at 1054 cm^{-1} and O=S=O scissoring vibration at 570 cm^{-1}, appeared and became obvious as the concentration of KMnO$_4$ increased.[54, 98] These results indicated that the sulfide bonds of the PEDOT NPs became oxidized into sulfoxide or sulfone as the treatment time and concentration increased. Furthermore, sulfur on the thiophene ring served as a site for KMnO$_4$ reduction, and MnO$_2$ domains were generated simultaneously (Figure 42).[54] We analyzed the atomic ratio of Mn to S of the PEDOT and MnO$_2$/PEDOT NPs (Table 4). The atomic ratio of Mn/S increased with escalating concentration and treatment time of KMnO$_4$. It is believed that the direct–contact reaction between MnO$_4^-$ and PEDOT NPs leads to initial formation of the first nuclei on the PEDOT surface. Subsequently, these seeds accelerated the water reduction of MnO$_4^-$ and allowed further growth of the MnO$_2$ domains.[54, 96]
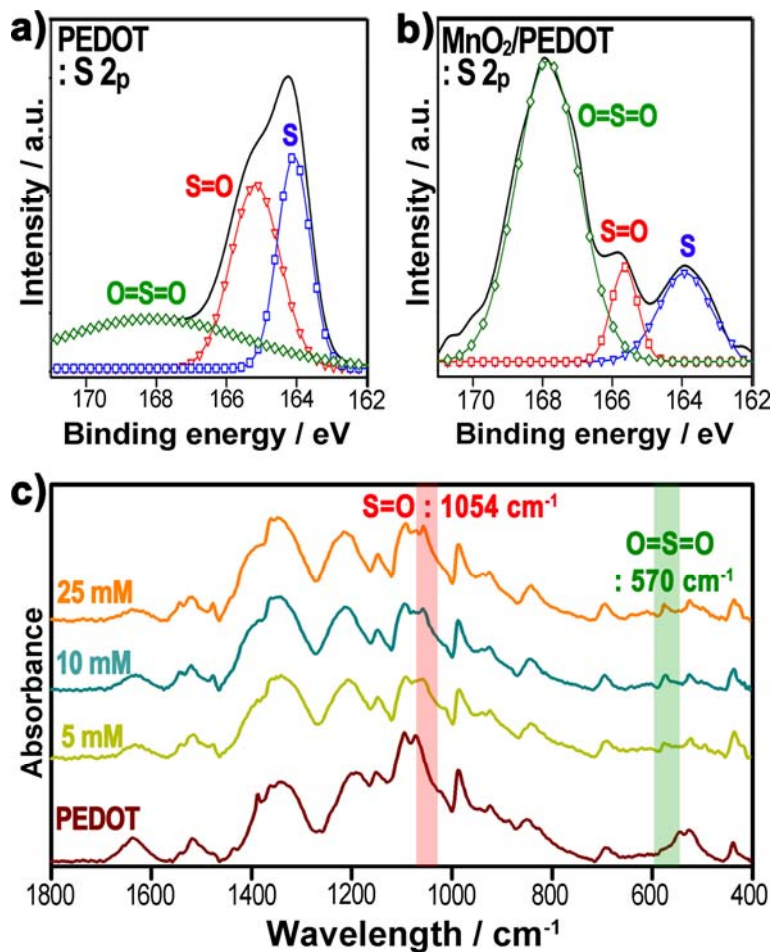
Figure 41. XPS spectra for S 2p of (a) PEDOT NPs (b) after KMnO$_4$ treatment (green, sulfone; red, sulfoxide; blue, sulfide). (c) FT–IR spectra of PEDOT and PEDOT NPs treated with KMnO$_4$ for 10 min.
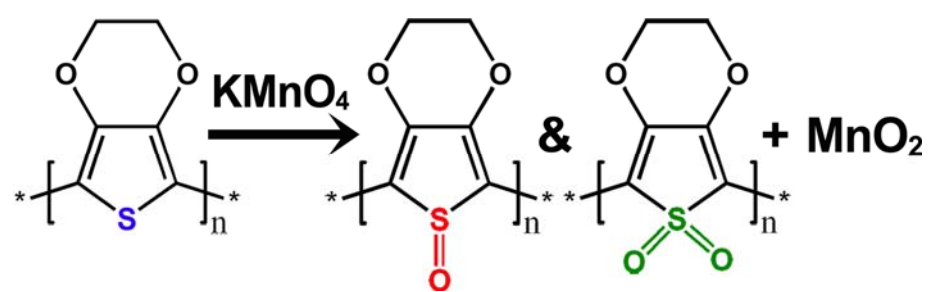
Figure 42. Proposed mechanism of reduction of PEDOT NPs and formation of MnO$_2$ domains.

Table 4. Atomic percent of Mn, S, and Mn/S ratio of MnO_2/PEDOT NPs with KMnO$_4$ concentration dependance and treatment time dependence[a]

| | KMnO$_4$ concentration[b] | | | Treatment time[c] | | | |
| | [mM] | | | [min] | | | |
	5	10	25	5	10	20	25
Mn	4.51	6.20	9.97	5.20	6.20	9.97	12.31
S	4.21	4.75	4.41	4.38	4.75	4.43	4.89
Mn/S	1.07	1.30	2.26	1.18	1.30	2.25	2.87

[a] The atomic percent of Mn and S in MnO_2/PEDOT NPs was measured by EDX, respectively. Based on these data, the atomic ratio of Mn/S was calculated. [b] The PEDOT NPs were treated with 5, 10, and 25 mM of KMnO$_4$ for 10 min. [c] The PEDOT NPs were treated with 10 mM KMnO$_4$ for 5, 10, 20, and 25 min.

3.2.1.2 Application for neuronal differentiation

To investigate the effect of MnO_2/PEDOT NPs on mammalian neuron differentiation, PC12 cells, derived from the pheochromocytoma of a rat adrenal medulla, were used as a model cell line. These cells sprout neurites and differentiate like sympathetic neuron cells in response to neurotropic molecules, such as NGF.[99] In past decades, MnO_2 NPs have received attention as MRI imaging agents [100, 101]; however, little is known about the influence of MnO_2 NPs on neuronal differentiation. To the best of our knowledge, this is the first investigation of the facilitation of neurite outgrowth by MnO_2 NPs. Figure 43 shows immunofluorescent images of PC12 cells treated with NGF and MnO_2/PEDOT NPs and stained with antibodies against β–tubulin (III) (anti–β–tubulin). The β–tubulin (III) is a neuronal–specific intermediate filament protein and so serves as a neuronal marker.[41] The protein is expressed in PC12 cells when they are exposed to neurotropic molecules, which is the evidence for the differentiation of PC12 cells. The MnO_2/PEDOT NPs facilitated the differentiation of PC12 cells in cooperation with NGF compared with treatment with NGF alone. Morphological changes in the cells were accelerated by increasing the treatment time and concentration of MnO_2/PEDOT NPs. The number of differentiated cells and the average length of neurites also increased in proportion to the dose of MnO_2/PEDOT NPs.

Neurite outgrowth was the most obvious when the highest dose of MnO$_2$/PEDOT NPs was applied to NGF–treated cells at day 3 compared with NGF–treated cells.

Statistical results of the immunofluorescent images were acquired using Image J software (Figure 44). MnO$_2$/PEDOT NPs affected the cell differentiation efficiency and average neurite length. The number of neurite–bearing cells (cell differentiation efficiency) and their lengths were in proportion to the dose of MnO$_2$/PEDOT NPs as well as treatment time. At 25 μg mL^{-1} MnO$_2$/PEDOT NPs for day 1, cell differentiation efficiency and average neurite length were 2 times and 2.3 times higher than those of NGF–treated cells, respectively. In addition, after cells were treated with 25 μg mL^{-1} MnO$_2$/PEDOT NPs for 3 days, 60% of cells were differentiated and average neurite length was 128 μm. Both data were approximately 1.5 times higher than those of treatment with NGF alone, which represented long–term stimulus to neurite outgrowth. These results indicated that MnO$_2$/PEDOT NPs gave huge impact on the neuronal differentiation not only at early stage of differentiation and but also at mature stage of differentiation.
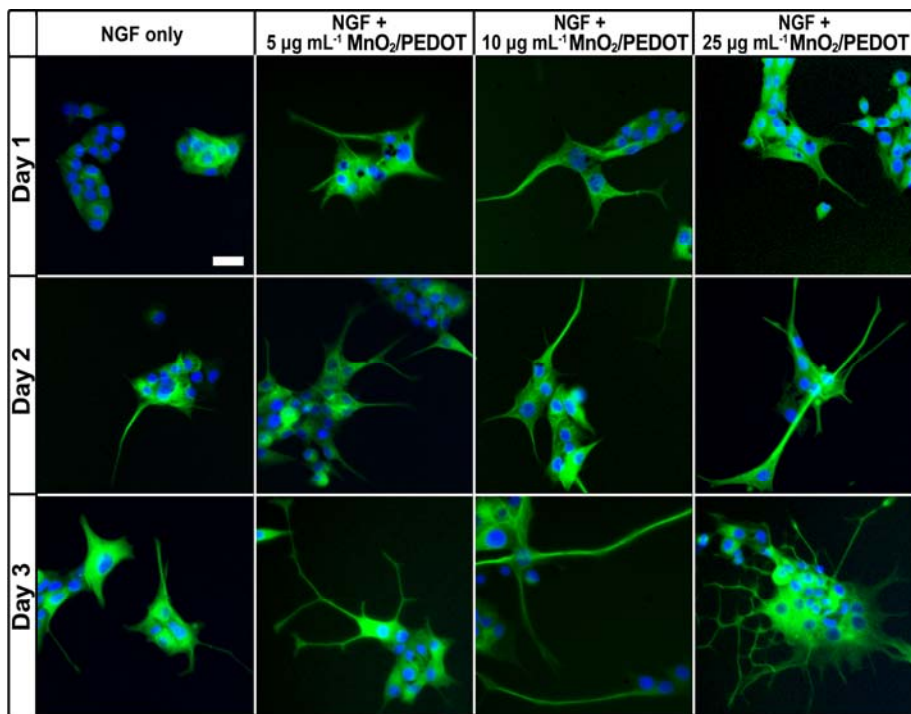
Figure 43. Neuronal response to MnO$_2$/PEDOT NPs. PC12 cells were stained with anti–β–tubulin (class III; neural specific marker; green) and DAPI (nucleus; blue). The cells were incubated with NGF (100 ng mL^{-1}), 0.1% BSA, and different concentrations of MnO$_2$/PEDOT NPs for 1–3 days (Scale bar: 25 μm).
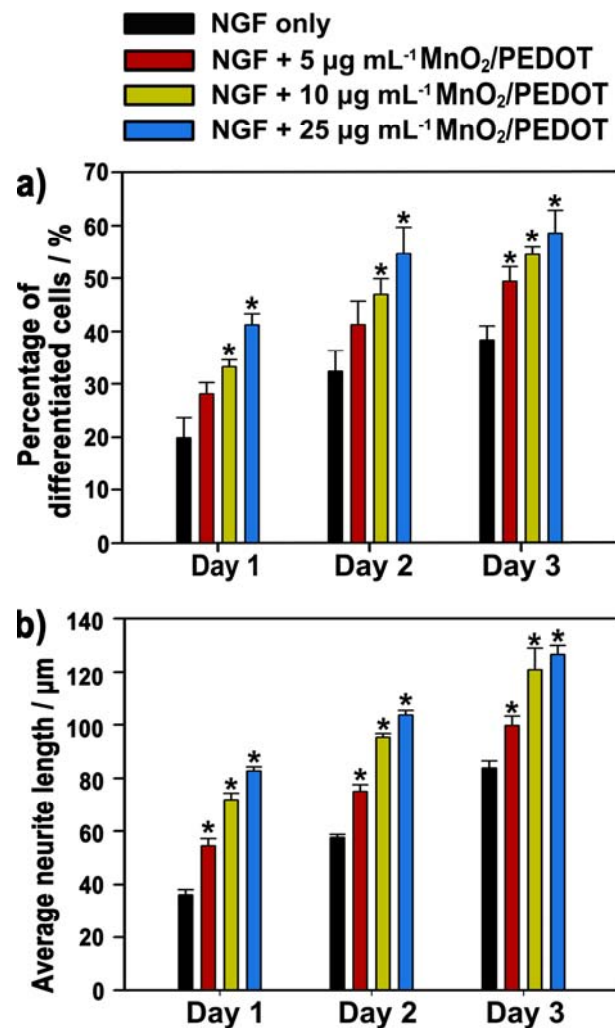
Figure 44. (a) Differentiation efficiency of and (b) average neurite length of PC12 cells as a function of the dose and time.

To compare capability of stimulating neurite outgrowth, control experiments were conducted in PC12 cells. In case of pristine PEDOT NPs and NGF (Figure 45), the cells were differentiated, but no synergetic effect was observed on neurite outgrowth compared with the case of NGF+MnO$_2$/PEDOT NPs. In the case of MnO$_2$/PEDOT NPs without NGF, the cells were not differentiated, indicating that the NPs did not activate the differentiation pathway directly, but facilitated the signaling effect when cooperated with NGF (Figure 46a). To investigate the influence of nanostructured MnO$_2$ toward neurite outgrowth, bulk MnO$_2$ was treated on the cells (Figure 46b-c). Bulk MnO$_2$–treated cells and bulk MnO$_2$+NGF–treated cells showed no extension, mostly damaged shapes, and many floating dead cells due to neurotoxicity of manganese.[102] Considering these data, bulk MnO$_2$ was harmful to the cells and not effective on neurite outgrowth, but the MnO$_2$/PEDOT NPs seemed to be safe and effective on differentiation owing to biocompatibility of PEDOT NPs.[2]

PEDOT matrix could lead to the internalization of MnO$_2$ domains and release Mn^{2+} ions inside the cells. The sharp increase in neurite outgrowth is mainly due to an inherent feature of manganese. Roth *et al.* studied the effects of various divalent metal salts on the morphology of PC12 cells.[32] They found that Mn^{2+} had the greatest facilitation effect on neurite outgrowth

compared with other divalent cations at maximal nontoxic concentrations. Furthermore, Mn^{2+} initiated differentiation within several hours after treatment, whereas the process of cell differentiation induced by NGF occurred relatively slowly after several days of treatment.[31, 32] Judging from these data, MnO_2/PEDOT NPs with NGF facilitated neurite outgrowth, and the MnO_2 domains played a crucial role in facilitating PC12 differentiation.

Because a small amount of Mn^{2+} was leached from MnO_2/PEDOT NPs in cell culture medium, we hypothesized that internalized MnO_2/PEDOT NPs could release Mn^{2+} into the cytosol and activate cell differentiation in cooperation with NGF. To verify this hypothesis, the cellular uptake of MnO_2/PEDOT NPs was visualized by TEM (Figure 47). As displayed in Figure 47a-c, most of the NPs were internalized and localized to endosomes (green arrows) and lysosomes (red arrows). MnO_2/PEDOT NPs were reached the plasma membrane without aggregation, and they were taken up as a single nanomaterial (Figure 47d). In general, the local pH inside the endosomes and lysosomes is pH 5.5–6.3 and pH 4.7, respectively.[103] Under acidic conditions, MnO_2 domains can be partially ionized and released Mn^{2+} ions into the cytosol.[104, 105] The MnO_2 domains were still remained on the MnO_2/PEDOT NPs after acidification (data not shown).
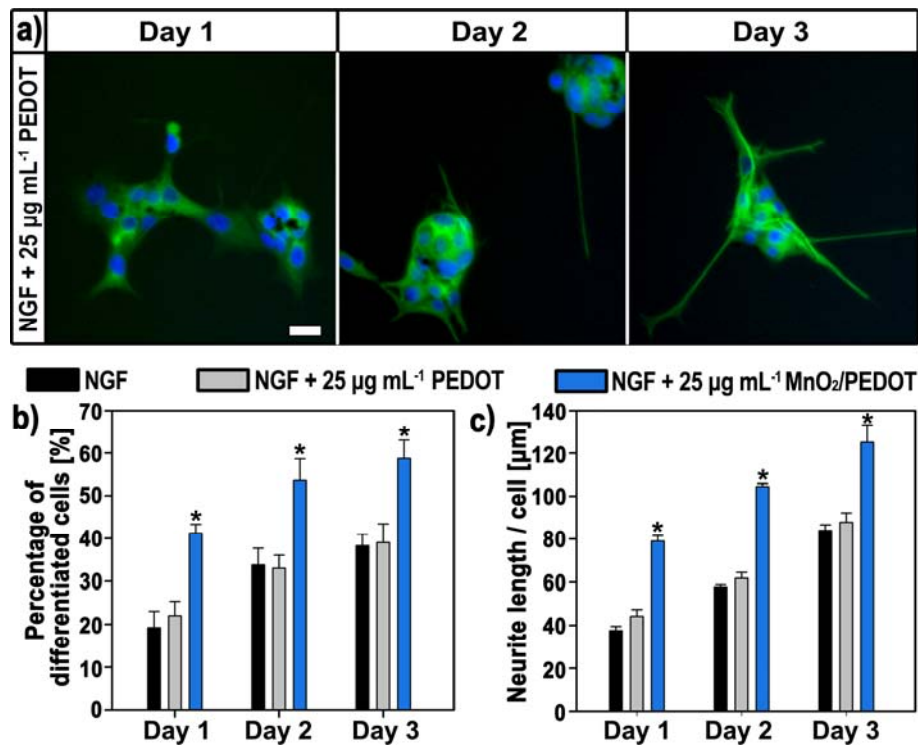
Figure 45. The effect of MnO_2 domains on PC12 cell differentiation. (a) The cells were incubated with NGF (100 ng mL^{-1}), 0.1% BSA, and pristine PEDOT NPs (25 μg mL^{-1}). These cells were stained with antibodies against β–tubulin III (green), and DAPI for nucleus (blue). (Scale bar: 25 μm). (b) Using these images, differentiation efficiency and average neurite length were calculated.
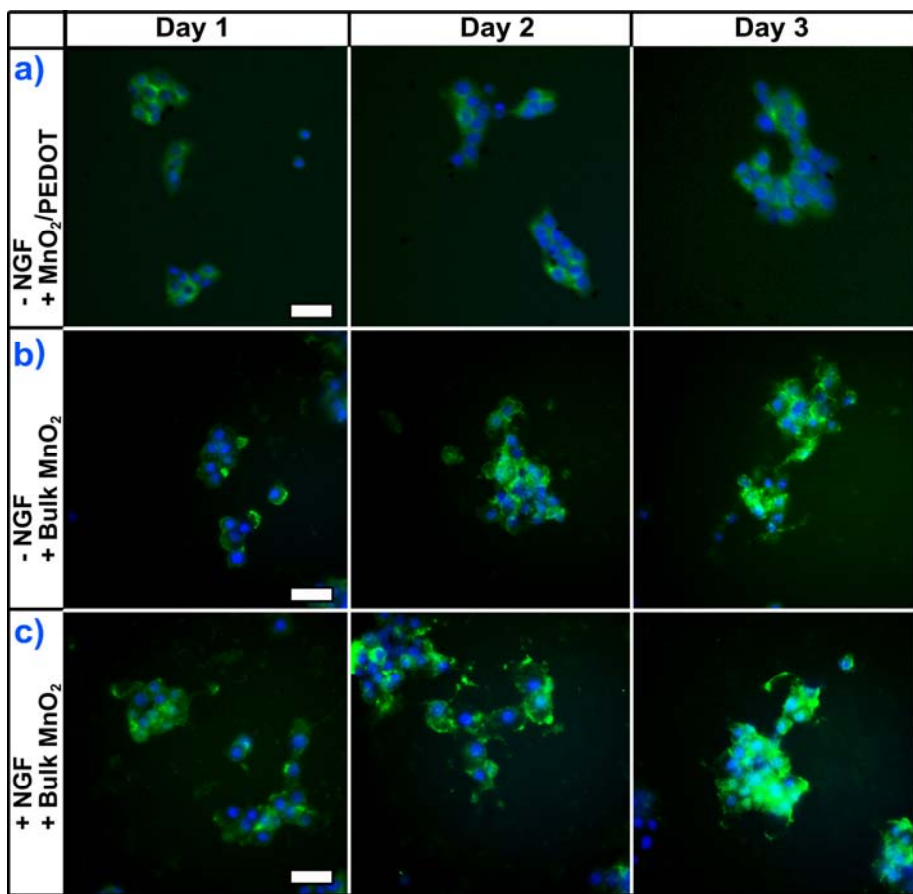
Figure 46. Control experiments as a function of time: (a) no NGF and MnO₂/PEDOT NPs, (b) no NGF and bulk MnO₂, (c) NGF+bulk MnO₂. These cells were stained against β–tubulin III (neural specific marker; green), and DAPI for nucleus (blue). (Scale bar: 25 μm).
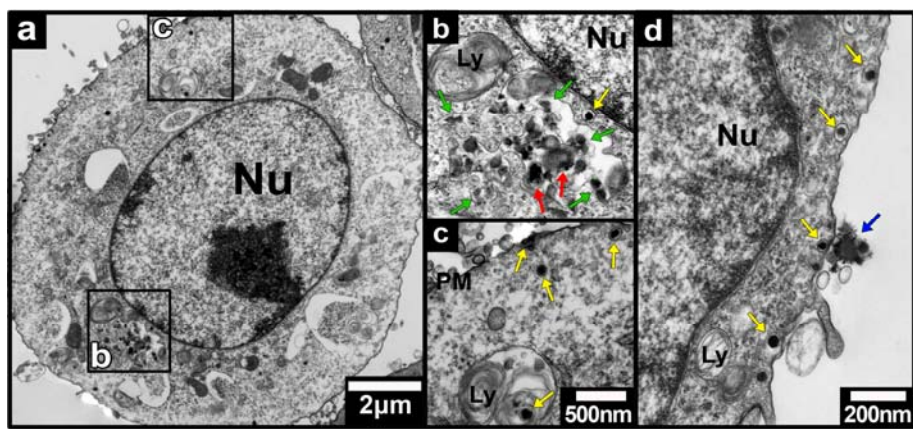
Figure 47. TEM images of PC12 cells incubated with MnO$_2$/PEDOT NPs (25 μg mL^{-1}) for 24 h. (a) Overall PC12 cell morphology and (b–d) magnified images. Blue arrow indicates MnO$_2$/PEDOT NPs seem to be taken up. Green and red arrows denote MnO$_2$/PEDOT NPs in endosomes and lysosomes, respectively. Yellow arrows show the catecholamines in vesicles. Abbreviations: Nu as nucleus; PM as plasma membrane; Ly as lysosome.

Divalent metal transporter 1 (DMT1) is known as a key protein responsible for the uptake and transport of Mn^{2+} into PC12 cells.[106] DMT1 consists of two isoforms produced by alternate splicing, +IRE and –IRE. Both present at the plasma membrane, the difference in the subcellular localization appears to be dependent upon cation needs. The +IRE and -IRE isoforms are found at the late endosomes/lysosomes and early endosome/recycling endosomes, respectively.[106] The expression level of the DMT1 was quantified using flow cytometric measurement. Figure 48a represented the expression of DMT1 in the PC12 cells incubated with MnO_2/PEDOT NPs and NGF for 1 day. The expression of DMT1 was in proportion of the concentration of MnO2/PEDOT NPs. In case of 25 μg mL^{-1} MnO_2/PEDOT NPs, the amount of expressed DMT1 increased 2 times higher than that of NGF–treated cells. It is considered that dissolved Mn^{2+} ion from internalized MnO_2/PEDOT NPs affect the expression of DMT1.

Transported Mn^{2+} ions using DMT1 activated extracellular–signal–regulated kinases 1/2 (ERK1/2) *via* phosphorylation.[106] The mitogen–activated protein kinase (MAPK)/ERK signaling cascade is activated by a wide variety of receptors involved in differentiation. ERK1/2, a central component in the MAPK cascade, has been played a role as a major participant in the regulation of cell differentiation. Upon phosphorylation, ERK1/2 moves to the

nucleus, and then turns on specific genes initiating cell differentiation and neurite outgrowth. NGF also uses MAPK/ERK signaling pathway.[107, 108] As shown in Figure 48b, the apex of the graph moved to the right, which means the level of phosphorylated ERK1/2 (pERK) increased with an increase in the dose of MnO_2/PEDOT NPs. On the basis of these data, it can conclude that released Mn^{2+} from MnO_2/PEDOT NPs was transported to the mitochondria using DMT1, which activated ERK1/2 pathway in cooperation with NGF. The resulting changes in gene expression cause cell differentiation, which is in good agreement with the above–mentioned hypothesis.[28] However, a high concentration of Mn^{2+} ions within mitochondria not only promoted neurite outgrowth but also acted as a neurotoxin in PC12 cells. Mn^{2+} ion, as a neurotoxin, induce the production of reactive oxygen species (ROS) and lead to disruption of mitochondrial function.[102]   Therefore, the viability of MnO_2/PEDOT–treated cells should be further evaluated for biological applications.
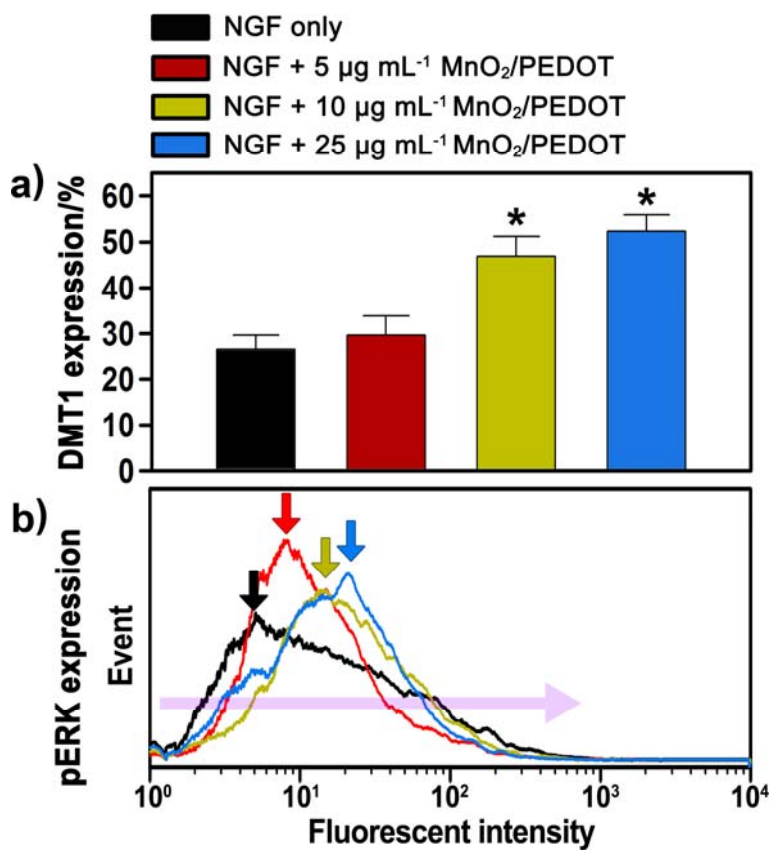
Figure 48. (a) DMT1 expression and (b) pERK expression in PC12 cells treated with NGF and NGF+MnO$_2$/PEDOT NPs. The arrows indicated that the apex of the graph.

The viability of PC12 cells incubated with MnO_2/PEDOT NPs was determined *in vitro* (Figure 49a). To evaluate the number of viable cells, a highly sensitive luminescence assay was conducted based on the determination of the ATP concentration. Viability after a 24 h treatment with 25 μg mL^{-1} MnO_2/PEDOT NPs was 91%. After 2 and 3 days, viability dropped to 87% and 81%, respectively. In a previous report, the viability of human fibroblast cells (IMR 90) treated with 25 μg mL^{-1} PEDOT NPs was 92% at day 1, and that of PEDOT nanomaterial–treated J774A.1 cells was 85%, which indicated no significant effect of MnO_2 domains on viability.[2] Furthermore, the number of live cells after 3 days was over 80% in the case of 25 μg mL^{-1} MnO_2/PEDOT NPs. These results were comparable with those of other precedent reports.[109, 110] In case of bulk MnO_2+NGF treatment (Figure 49b), the viability was decreased from 82% to 57% during 3 days, which is in good agreement with immunofluorescence images (Figure 46c). Considering these data, PEDOT NPs reduced toxicity of MnO_2, resulted in enhancement of viability in MnO_2/PEDOT nanomaterial-treated cells. Collectively, MnO_2/PEDOT NPs can be considered low toxic materials and are suitable for bio–applications.
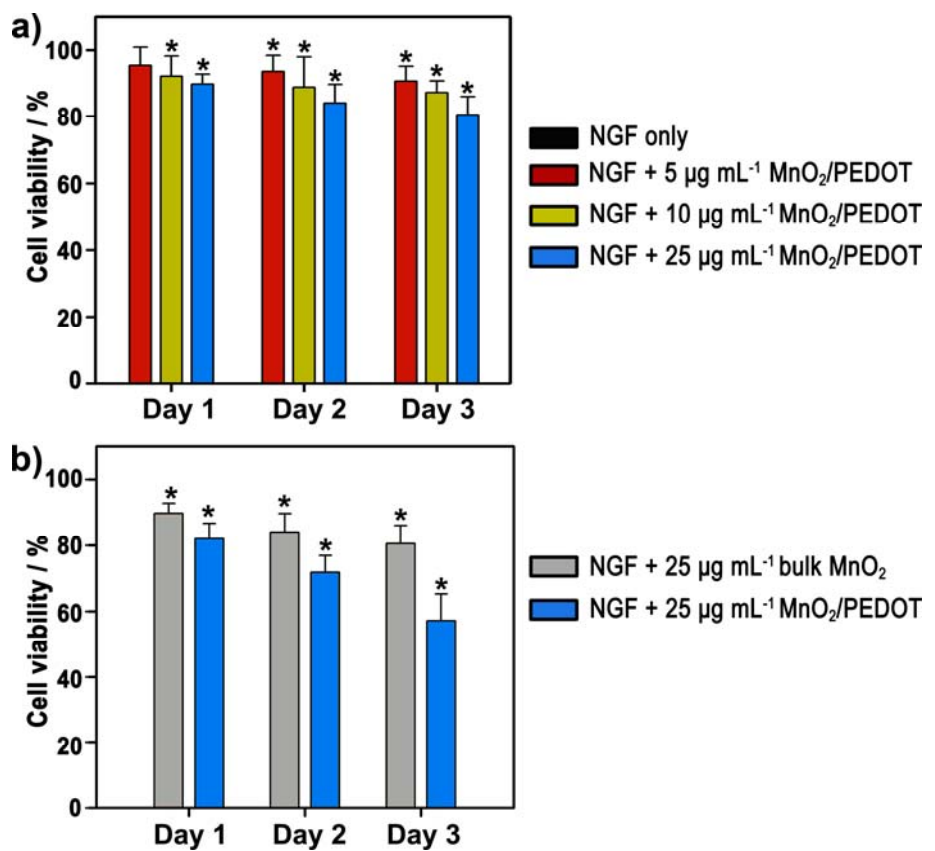
Figure 49. Viability of (a) NGF+MnO$_2$/PEDOT NPs and (b) NGF+bulk MnO$_2$ treated PC12 cells.

3.2.1.3 Application for catecholamine detection

Due to their biocompatibility and conductivity, MnO_2/PEDOT NPs could be used as a platform for label–free real–time monitoring of catecholamine secretion from PC12 cells. PC12 cells were used as a model to investigate neurotransmitter secretion from neurons as well as to study neuronal differentiation due to process similarity between sympathetic neurons and PC12 cells.[111] Chemical communication between cells is predominantly accomplished by the release of neurotransmitters *via* an 'exocytosis' process.[112] Among various chemical messenger molecules, catecholamine molecules (*e.g.*, dopamine, epinephrine, and norepinephrine) are major neurotransmitters. These are initially stored in the secretory vesicles with large dense core (Figure 47, yellow arrows).[113] When the intracellular potential increases, the voltage–gated Ca^{2+} channels open following cell depolarization. The influx of Ca^{2+} ions through these channels provokes translocation of secretory vesicles to the plasma membrane. The translocated secretory vesicles fused with the plasma membrane, leading to the release of catecholamines into the extracellular space. In Figure 47c and d, secretory vesicles containing catecholamines can be seen localized near the plasma membrane. Additionally, the release of catecholamines into the extracellular space was also presented in Figure 47c. Once catecholamines were released into the narrow gap between

the cell and the MnO_2/PEDOT NPs, they diffused quickly onto the MnO_2/PEDOT NPs and interacted with them by π–π interactions.[42, 55, 56] Interactions between MnO_2/PEDOT NPs and catecholamines affect the charge–carrier density of the MnO_2/PEDOT NPs, and thus allow for label–free monitoring of catecholamine secretion from neurons. A schematic diagram of the system is displayed in Figure 50. The MnO_2/PEDOT NPs were immobilized onto the substrate by vacuum dehydration. This method allows for the delivery of a few NPs into cells, while maintaining most of the NPs immobilized on the substrate.[114]

The properties of the PEDOT/MnO_2 device can be demonstrated by I-V characterization (Figure 51). The linear I–V plots over a voltage range from -0.1 to +0.1 V confirmed the ohmic behavior of the PEDOT and MnO_2/PEDOT NPs on the gold electrodes. The ohmic behavior is important to the sensing properties, because the sensitivity is affected by contact resistance. After MnO_2 were decorated on the PEDOT NPs, the contact resistance decreased from 0.83 KΩ to 0.56 KΩ. The lower resistance of MnO_2/PEDOT NPs was mainly due to enhanced conductivity.[53] The conductivity of the MnO_2/PEDOT NPs was 45 S cm^{-1}, which was higher than PEDOT NPs (35 S cm^{-1}).
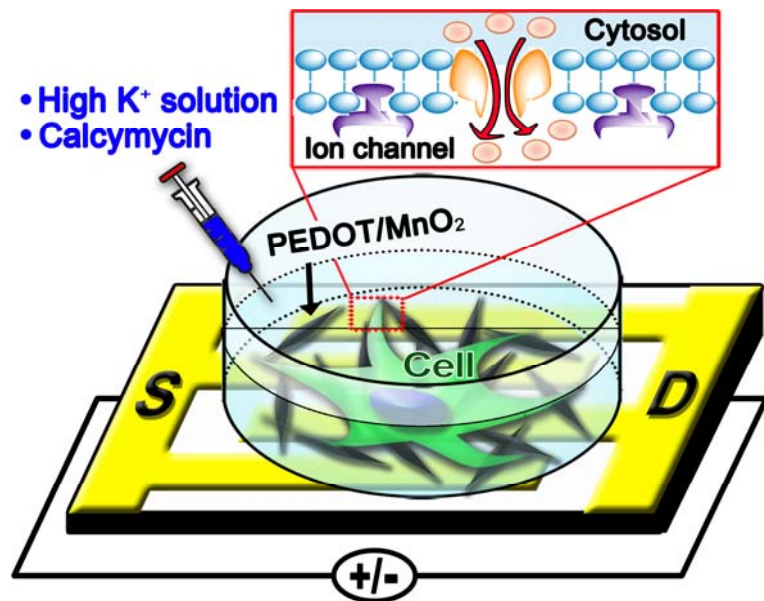
Figure 50. A schematic illustration of the experimental setup of sensor application.
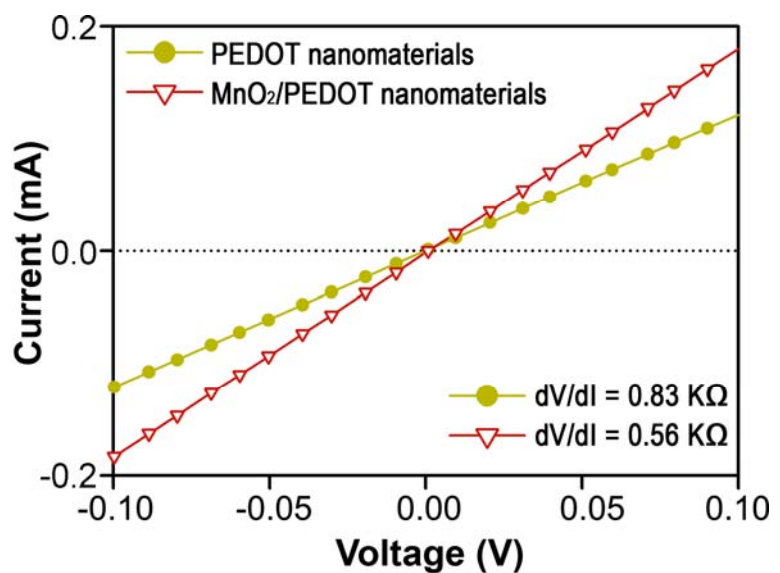
Figure 51. I–V curves of PEDOT nanoellipsoids and MnO$_2$/PEDOT NPs deposited on gold interdigitated microelectrodes at a scan rate of 10 mV s^{-1}.

To explore the sensing capability of MnO$_2$/PEDOT NPs, catecholamines were inserted onto a recording chamber without cells (Figure 52a). All three catecholamines tested induced a sharp current spike due to their aromatic ring, indicating that the discharge of catecholamines caused a transient increase in the MnO$_2$/PEDOT current. High potassium solution and calcimycin, as representative secretagogues, were also introduced into a chamber for control experiments. These molecules, unlike catecholamines, induced a broad and relatively small signal in the absence of cells (Figure 52b). Considering these results, PEDOT/MnO$_2$ sensors were suitable for label–free real–time monitoring of catecholamine secretion from PC12 cells when secretagogues are introduced.

Figure 53 displays the responses of dopamine, epinephrine, and norepinephrine after gradual addition of catecholamines, increasing their concentration from 0.25 to 2.5 mm. The MnO$_2$/PEDOT NPs, as a sensor transducer, showed a concentration–dependent increase in current upon exposure to the catecholamines. After removing the catecholamines by washing with 0.1 m PBS, the current returned to its initial level.

MnO$_2$/PEDOT NPs were used for real–time monitoring of PC12 cells. To investigate the sensor capability of the MnO$_2$/PEDOT materials, the current was monitored in real time at $V_{SD} = 50$ mV, a low operating voltage. The low

V_{SD} is advantageous in terms of minimizing possible disturbances to the living cells and avoiding the instability of devices due to the induced electrochemical or charging effects.[55]

Two secretagogues, high potassium solution and calcimycin, were utilized to induce secretion of catecholamines from PC12 cells. High potassium solution and calcimycin triggered exocytosis *via* plasma membrane depolarization and formation of Ca^{2+} selective ion channels, respectively. As shown in Figure 54, a train of current spikes was detected after the secretagogues were inserted. Each spike corresponded to Ca^{2+}–dependent exocytosis of catecholamines from PC12 cells.[55, 112, 113] The signals generated by these secretagogues can be distinguished from constitutively secreted molecules by their rapid secretion speed. Compared with electrophysiological single–cell recordings,[115, 116] this nanoelectronic approach is non–invasive and does not require high experimental skills.[42] Therefore, the PEDOT/MnO$_2$ sensor provides an alternative approach for detecting the dynamic biosensing activities of living cells.

145
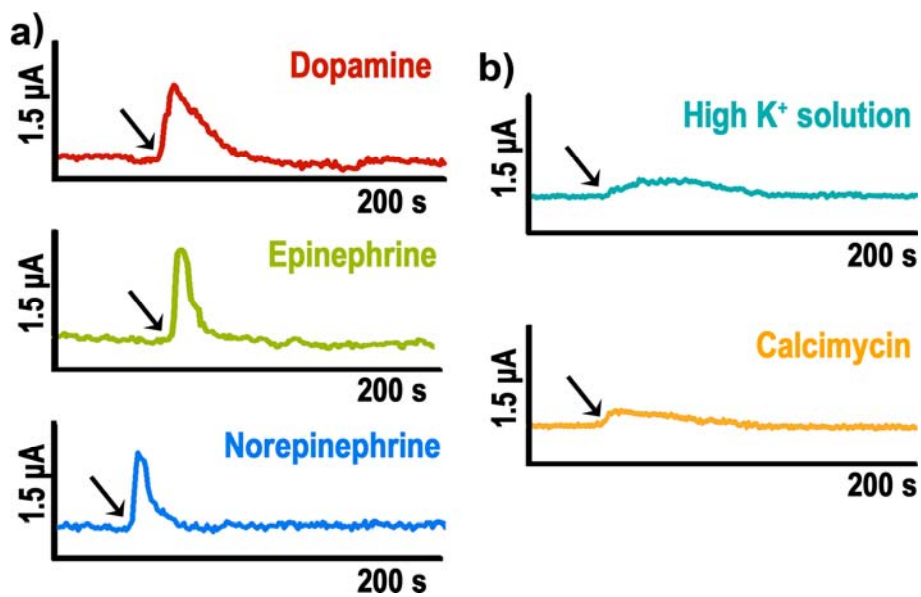
Figure 52. (a) Response of MnO_2/PEDOT sensor upon exposure of 0.25 mM catecholamines and (b) response of MnO_2/PEDOT sensor toward high potassium solution and calcimycin (V_{SD}=50 mV). The black arrows indicate where the stimulations were applied.
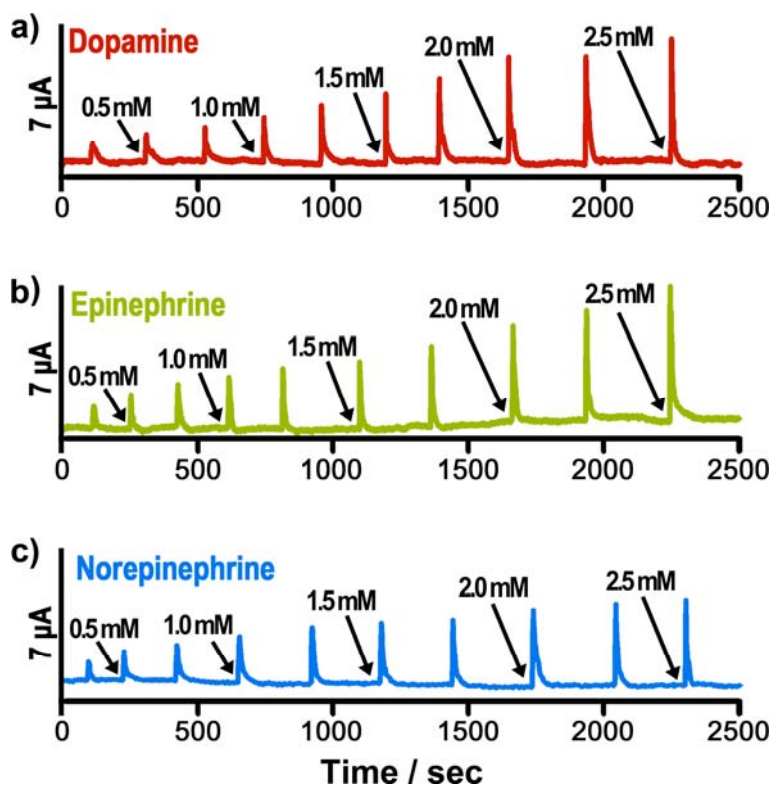
Figure 53. Detection of (a) dopamine, (b) epinephrine, and (c) norepinephrine by MnO$_2$/PEDOT sensor (V$_{SD}$ = 50 mV). Each step represents the gradual addition of catecholamines with concentration increasing.
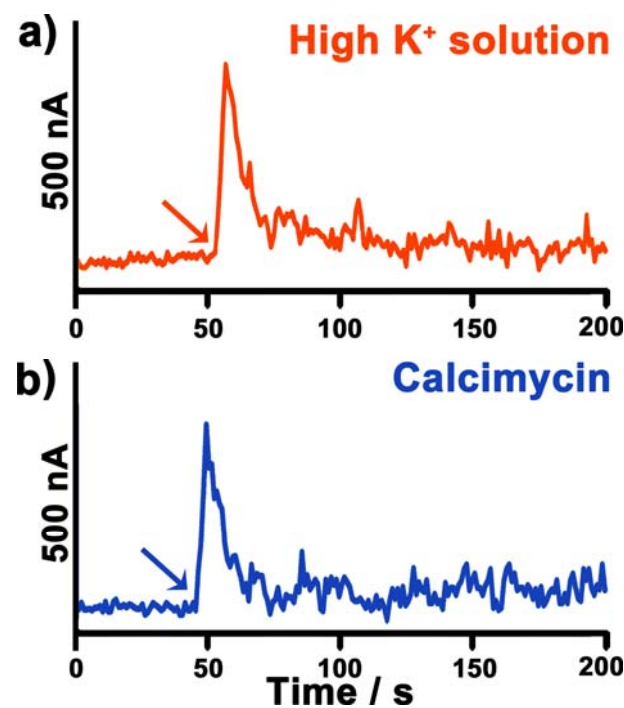
Figure 54. Live cell responses of MnO$_2$/PEDOT sensor measured at V$_{SD}$=50 mV upon addition of (a) high potassium solution and (b) calcimycin (arrows signify inserting time).

3.3. PAN based hybrid nanoparticles

3.3.1. Amidine-PAN nanoparticles

3.3.1.1 Fabrication of amidine-PAN nanoparticles

Amidine-modified PAN nanoparticles (APAN NPs) are prepared as shown in Figure 55. Polyacrylonitrile nanoparticles (PAN NPs) were synthesized by ultrasonic mediated emulsion polymerization, as previously described.[57] Sodium dodecylsulfate and acrylonitrile monomer were dissolved in distilled water, followed by ultrasonic irradiation to form emulsion phase. Cerium sulphate and nitroacetic acid, as co-initiators, were introduced into the solution, and then additional ultrasound was administered for polymerization of acrylonitrile monomer. In order to introduce amidine group on the PAN NPs, modified Pinner method was employed.[47, 117] The APAN NPs were produced by treatment of hydrogen chloride and ammonia on the PAN NPs under nitrogen atmosphere. APANs exhibited strong blue fluorescence compared to PAN NPs due to change of the surface functional group. The PAN and APAN NPs had a narrow size distribution, mostly in the range of 40-50 nm as determined by SEM and TEM images. Nanoparticle shape and size were still maintained after the surface modification with amidine group. The PAN and APAN had a narrow size distribution.
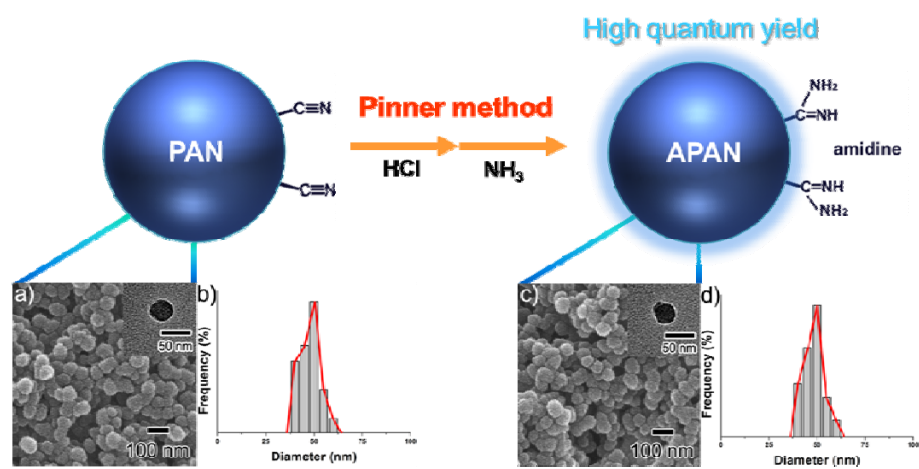
Figure 55. Schematic diagram of fabrication of APAN NPs, and their TEM and size distribution histograms determined by TEM images.

The formation of PAN and APAN NPs was confirmed by Fourier-transform infrared (FT-IR) spectrometry (Figure 56). The FT-IR spectrum of the PAN NPs shows characteristic PAN peaks, including the C≡N stretching bands at 2244 cm^{-1}, the C-H stretching peak at 2948 cm^{-1}, and C-H deformation peak at 1451 cm^{-1}. These peaks reveal the successful polymerization of PAN by ultrasonic mediated emulsion polymerization. For the APAN NPs, new double peaks related to primary amine group appeared, including peak at 3593 and 3654 cm^{-1}. On the basis of these data, amidine group were successfully introduced on the PAN NP surfaces.

The optical properties of PAN NPs and APAN NPs were studied by UV-vis absorption and photoluminescence (PL) spectroscopy. The UV-vis absorption spectrum of APAN (red line) had absorption enhancement in the UV region (200–300 nm) with a peak at 260 nm (Figure 57a) compared to that of PAN (black line). These 260 nm band peak represented a π-π* transition of the C=N group, which is accordance with other evidences for amidine group on the surface of APAN NPs (FT-IR).[118] Inset images in Figure 57a depicted the fluorescence photographs of the PAN and APAN NP taken under 365 nm UV light. The fluorescence color was changed from blue (PAN NP) to bright blue (APAN NP) by surface modification. Excitation dependent emission of APAN NP was observed as the excitation wavelength varied from 260 to 320 nm, and

the maximum emission intensity of APAN NPs was achieved at 410 nm (λ_{ex}=290 nm) (Figure 57b). Their fluorescence quantum yield was calculated as ca. 0.19 using the standard reference 7-amino-4-methylcoumarin, which is 11 times higher than that of the previously reported PAN nanoparticles.[47, 117, 119] Therefore, enhanced PL properties of APAN NP can be used as intracellular fluorescence sensing probe with high sensitivity and sensitivity.

In order to identify the capability of APAN NPs as "turn-off" sensor for copper ion, the selectivity of APAN NPs was evaluated by screening various metal ions at a concentration of 10 μM (Figure 58a). The fluorescence of APAN NPs was quenched by addition of Cu^{2+} (26% quenching upon addition of 10 μM Cu^{2+}), while no significant quenching effect was observed in other metal ions (Ag^+, Al^{3+}, Ca^{2+}, Cd^{2+}, Co^{2+}, Fe^{2+}, Fe^{3+}, Hg^{2+}, K^+, Mg^{2+}, Mn^{2+}, Na^+, Ni^+, Pb^{2+}, and Zn^{2+}). In general, metal ions have a tendency to bind to and be coordinated with the amidine group of the APAN NPs due to their negative charge and unshared electron of the nitrogen atom on the amidine group (inset image in Figure 58a).[120, 121] In contrast with other metal ions, because of its paramagnetic property and unfilled d shell, copper ions could strongly quench the fluorescence of the APAN NPs through electron transfer processes.[48, 122] As displayed in Figure 58b, the added copper ion induced a marked decrease in fluorescence intensity of the APAN NPs (10 μg mL^{-1}) and

the peak was blue-shifted from 410 to 370 nm (λ_{ex}=290 nm). Based on the Figure 58b, fluorescence intensity change of the APAN NPs was calculated *versus* copper ion concentration (Figure 58c). The fluorescence intensity remarkably decreased with increasing copper ion concentration. The inset graph showed a linear correlation between the emission intensities and the concentration of Cu^{2+} (0-100 nM; adjusted R^2 = 0.991). The limit of detection was 10 nM (3σ of the reagent blank signal), which is better than or at least comparable to previous reports.[48, 123, 124] Additionally, in the physiological concentrations, the minimum concentration of intracellular copper ion is 10 μM, suggesting the potential of APAN NPs as sensitive detection probe for copper ions under the physiological conditions.[123] As a control experiment, ethylenediaminetetraacetate (EDTA) was inserted into the solution containing copper ion and APAN NPs (Figure 58d). EDTA can chelate with metal ions in a 1:1 ratio, which induces removal of the metal ions from the solution.[124] As expected, the quenched fluorescence of the APAN NPs in the presence of Cu^{2+} ion was recovered into strong fluorescence by treatment with EDTA. This fluorescence recovery of the APAN NPs also confirmed by inset images in Figure 58d. Taking these facts into account, APAN NPs are suitable for copper ion detection with high sensitivity and selectivity against other metal ions.
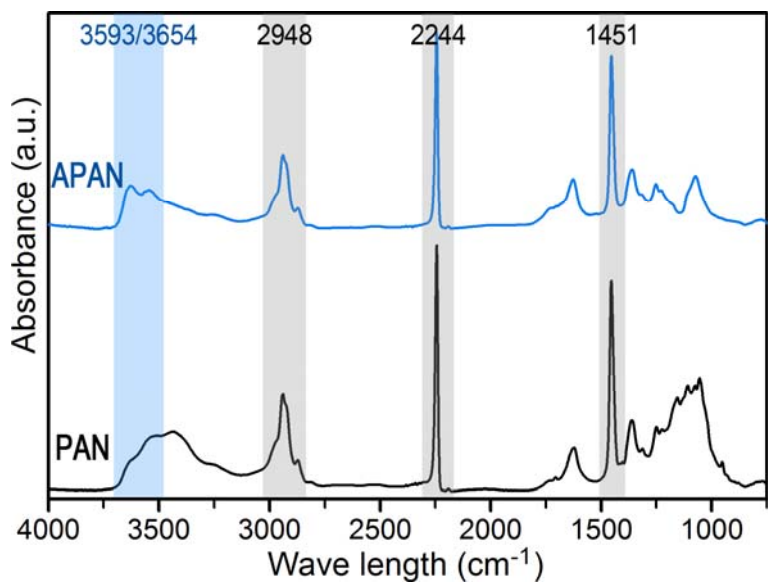
Figure 56. FT-IR spectra of PAN (black) and APAN (blue) NPs.
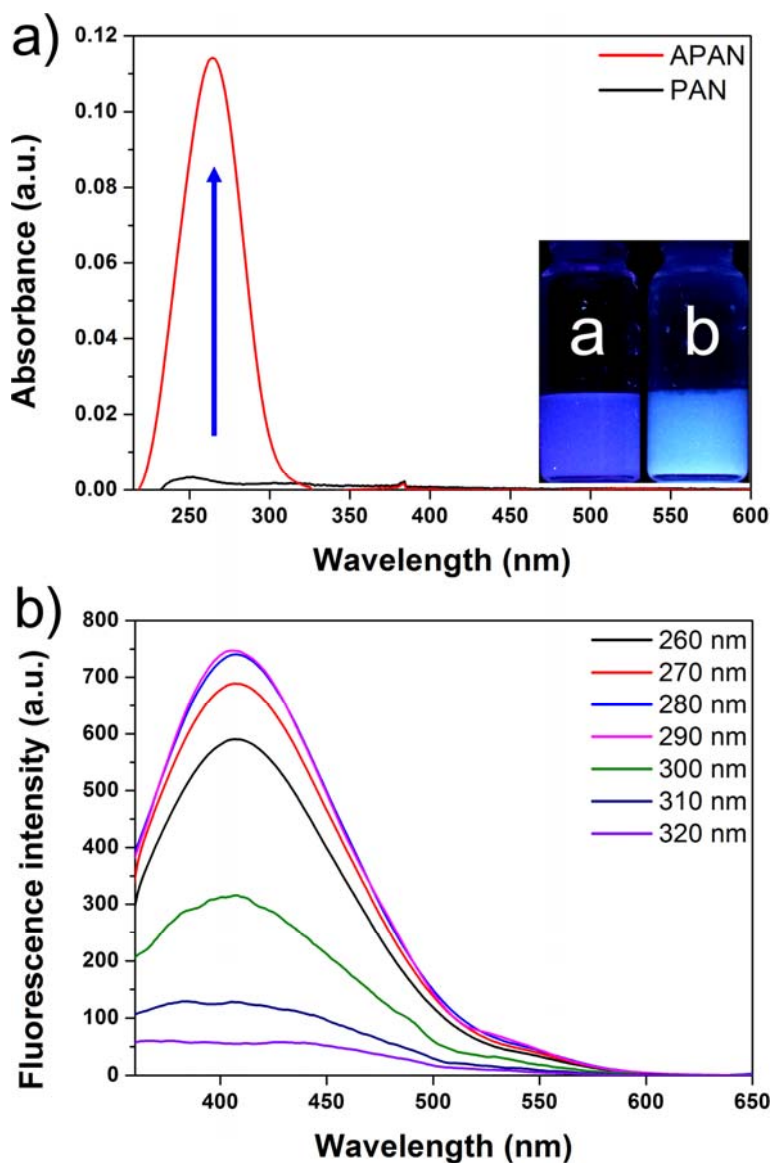
Figure 57. (a) UV- vis absorption spectra of PAN NP and APAN NPs. The inset shows the photograph of (a) PAN and NPs and (b) APAN NPs under UV light (365 nm). (b) Fluorescence spectra of APAN NPs under different excitation wavelength.

Figure 58. (a) Selectivity of APAN NPs (10 μg mL^{-1}) for different metal ions (10 μM). Inset represents the possible sensing mechanism of APAN NP for Cu^{2+}. (b) Fluorescence emission spectra of APAN NPs in the presence of Cu^{2+} at different concentrations (0-100 μM). (c) Based on the Figure 4b, the relationship between emission fluorescence intensity of APAN NPs and concentrations of Cu^{2+} was calculated. I and I$_0$ are the emission fluorescence intensities of the APAN NPs at 290 nm in the presence and absence of Cu^{2+}, respectively. Inset is the linear region. (d) Representative fluorescence spectra with the addition of Cu^{2+} and EDTA in the quenching recovering. The inset shows the fluorescence photograph of (a) APAN NPs, (b) APAN NPs + Cu^{2+}, and (c) APAN NPs+Cu^{2+}+EDTA under UV light (365 nm).

3.3.1.2 Application for intracellular Cu²⁺ detection

In order to apply APAN NPs as fluorescence sensor for intracellular Cu^{2+}, SK-BR-3 cells were incubated with 10 μg mL^{-1} APAN for 24 h (Figure 59a). Amidine group of the APAN NPs possess positive surface charge, leading to adhesion between APAN and the plasma membrane. Internalized APAN exhibited blue fluorescence around the nuclei, making APAN possible to detect copper ions in cells. Then, the copper ions were inserted into the culture medium for 20 min, and the blue fluorescence of APAN NPs was turned off in the presence of Cu^{2+} (Figure 59b). As control experiment, excess EDTA was also added to copper ion containing culture medium to eliminate copper ions. The strong fluorescence of APAN NPs re-appears as shown in Figure 59c. These data implies that APAN NPs is easily introduced into cells and can be used as a fluorescence sensor for copper ions in living cells.

For using APAN as intracellular sensor probe, low cytotoxicity of the APAN NPs is required. Cytotoxicity of the APAN NPs was determined by two methods (Figure 60); adenosine triphosphate (ATP) based viability test and generation of reactive oxygen species (ROS) by APAN NP treatment. First, ATP concentrations of APAN NP treated SK-BR-3 cells were measured by transformation of luciferin to oxyluciferin. Until a concentration of 10 μg mL^{-1}, the viability of APAN NPs incubated cells showed no decrease than negative

control (0 μg mL^{-1}). The viability was over 80% even at a high concentration of APAN (100 μg m L^{-1}) for 24 h incubation. We also evaluate production of ROS in APAN NP-added SK-BR-3 cells by 2',7'-dichlorodihydrofluorescein diacetate (H$_2$DCF-DA) staining. After APAN NP treatment, compared to negative control, ROS production increased within the margin of error. Collectively, APAN NPs can be applied as intracellular copper ion detector without significant viability decrease or ROS production. Therefore, APAN NPs offers a selective detection probe for copper ion in living cells with low toxicity.
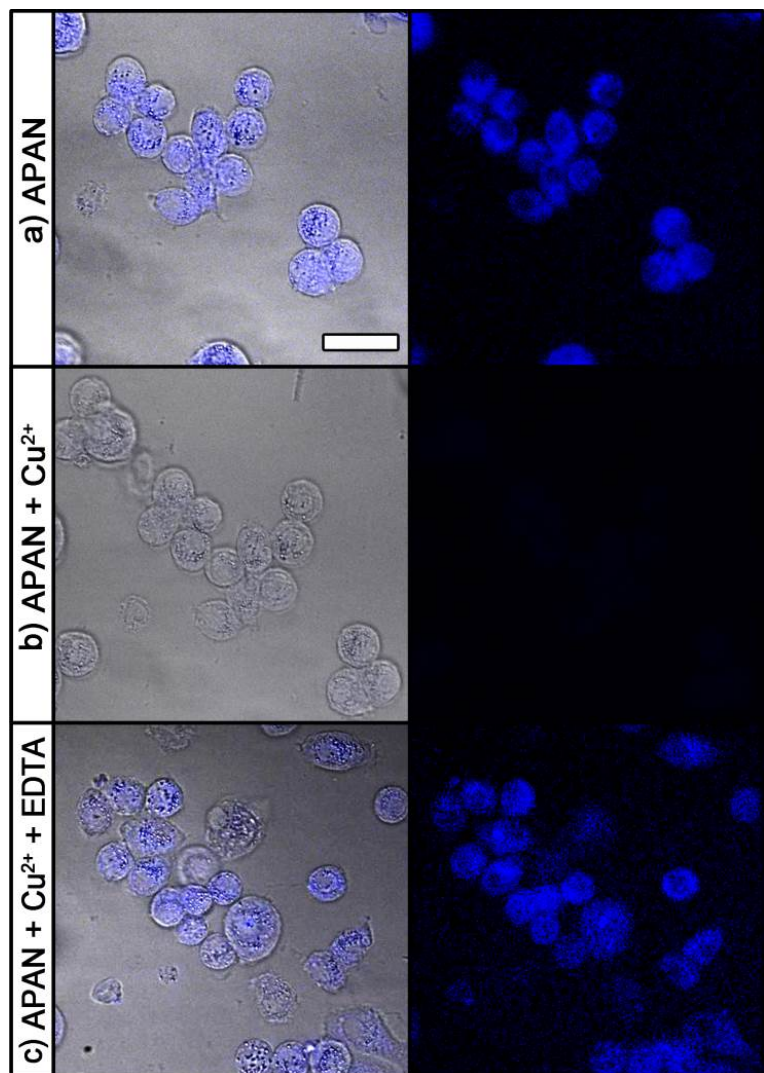
Figure 59. Live cell differential interference and fluorescence images of the SK-BR-3 cells. The cells were treated with (a) APAN NPs, (b) APAN+Cu^{2+}, (c) APAN+Cu^{2+}+EDTA (scale bar: 90 μm).
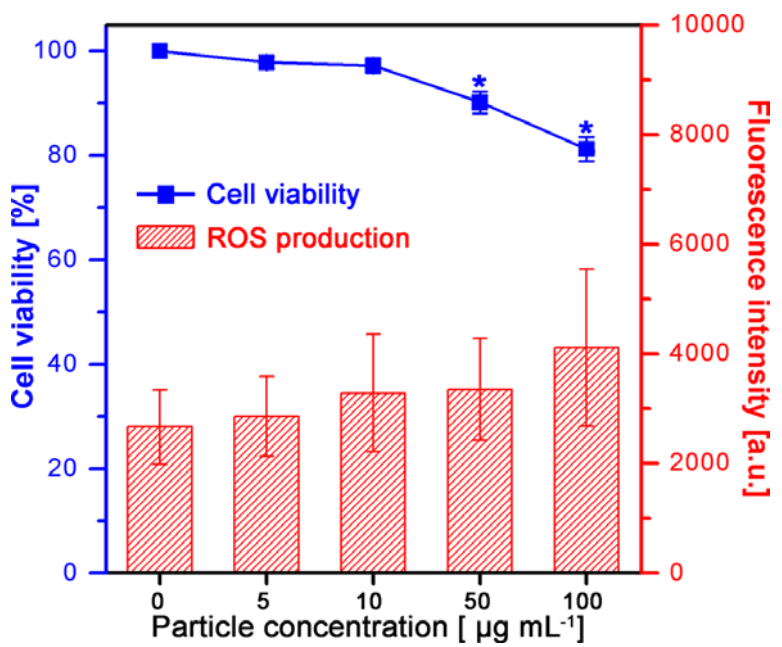
Figure 60. Viability and ROS production of SK-BR-3 cells incubated APAN NPs for 24 h.

3.3.2 Au decorated amidine-PAN nanoparticles

3.3.2.1 Fabrication of Au decorated amidine-PAN nanoparticles

Figure 61 illustrated a schematic diagram of the fabrication of the Au-APAN NPs used in this study. Polyacrylonitrile nanoparticles (PAN NPs) were synthesized by ultrasonic mediated emulsion polymerization, as previously described in part 3.3.1.1.[57] The gold nanoclusters (AuNCs), fabricated by reduction of chloroauric acid ($HAuCl_4$) with L-glutathione (GSH), were decorated on the surface of the APAN NPs *via* EDC/NHS chemistry. The as-synthesized AuNCs decorated APAN NPs (Au-APAN NPs) emit dual fluorescence; orange and blue fluorescence were respectively from the AuNCs and APAN NPs. The AuNCs have capability to react with hROS (O_2^-, superoxide; OCl^-, hypochlorite; and $\cdot OH$, hydroxyl radical), which induces quenching effect on the fluorescence of AuNCs. As a result of hROS detection, the fluorescence of Au-APAN NPs was changed from violet (blended color from blue and orange) to blue. The fluorescence intensity ratio between APAN NPs and AuNCs provides the information of intracellular hROS.

Figure 62a and b represent AuNCs and APAN NPs were uniform sphere in shape with diameter of *ca.* 2 nm and 51 nm, respectively. Inset image in Figure 2a indicated marked interplanar d spacing (0.24 nm) corresponding to that of the lattice planes of the Au. [125] After decoration of AuNCs on the surface of

the APAN NPs, average diameter increased from 51 nm to 55 nm (Figure 62c and d). The dark spots in Figure 62c denoted the successful incorporation of AuNCs on the APAN NPs. The amount of decorated AuNCs on the APAN NPs was measured as *ca.* 25.8 wt% by inductively coupled plasma emission spectrometer (ICP) analysis.

The formation of PAN, APAN NP, and Au-APAN NPs was confirmed by Fourier-transform infrared (FT-IR) spectrometry (Figure 63a). The FT-IR spectrum of the PAN NPs shows characteristic PAN peaks, including the C≡N stretching bands at 2244 cm^{-1} and C-H deformation peak at 1451 cm^{-1}. These peaks reveal the successful polymerization of PAN by ultrasonic mediated emulsion polymerization. For the APAN NPs, new double peaks related to primary amine group appeared, including peak at 3593 and 3654 cm^{-1}. After AuNC conjugation on the APAN NPs, new three peaks were appeared; N-H deformation peak at 1554 cm^{-1}, C=O stretching peak at 1711 cm^{-1}, and secondary amine stretching peak at 3335 cm^{-1}. The presence of AuNC was further confirmed by XPS spectra and enlarged Au 4f spectra (Figure 63b and c). On the basis of these data, amidine group and AuNC were successfully introduced on the PAN NP surfaces.
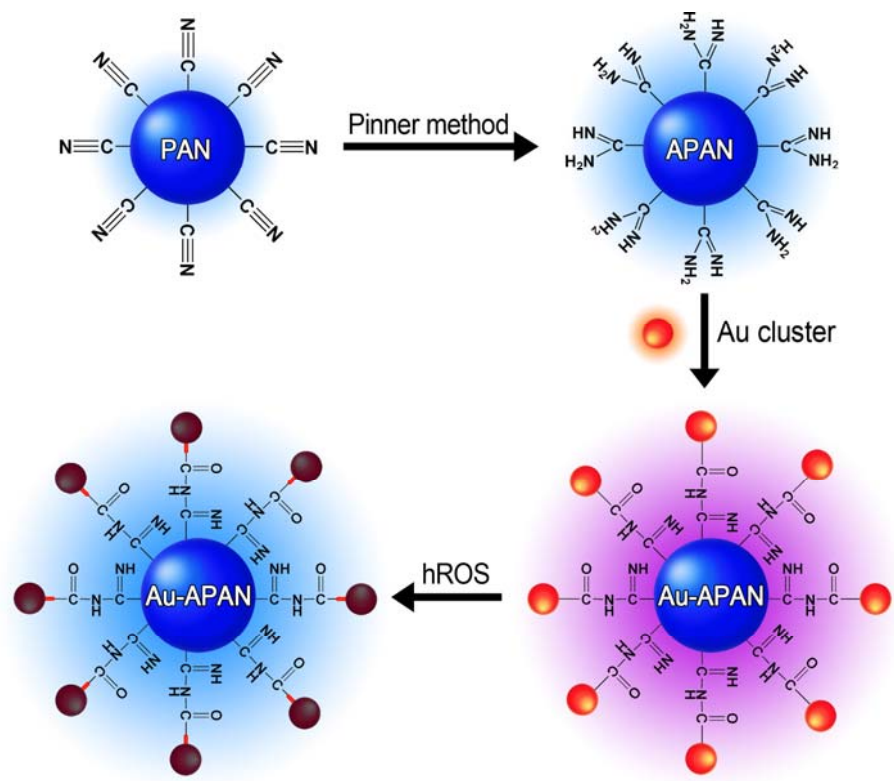
Figure 61. Schematic diagram of fabrication of Au-APAN NPs.
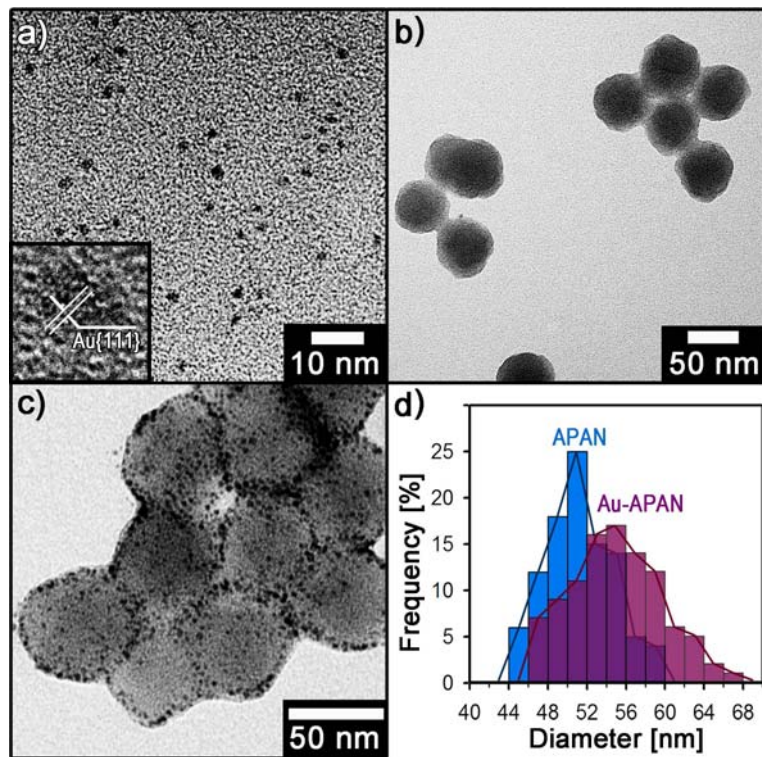
Figure 62. (a) High resolution TEM image of AuNCs, and TEM images of (b) APAN NPs, and (c) Au-APAN NPs. (d) size distribution histograms determined by TEM images (blue and violet mean APAN and Au-APAN NPs, respectively)
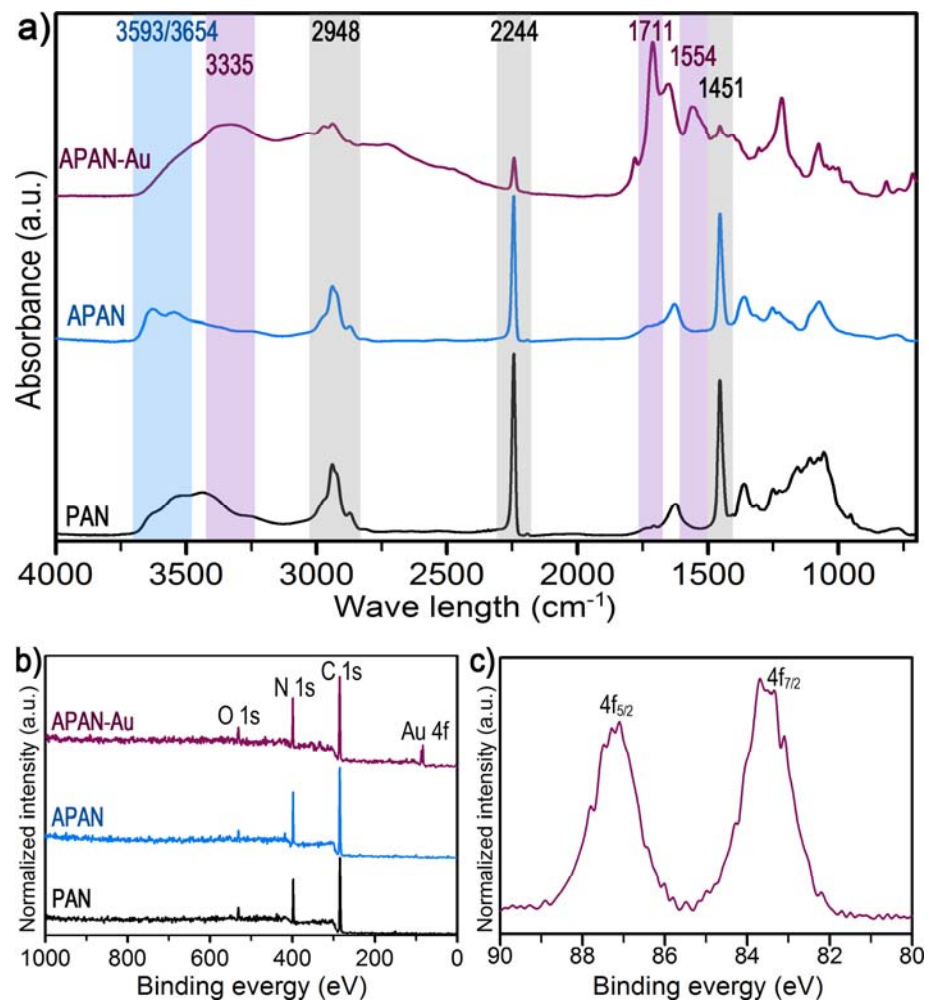
Figure 63. (a) FT-IR spectra of PAN (black), APAN (blue), and Au-APAN (violet) NPs. (b) XPS spectra of APAN (blue), and Au-APAN. (c) Enlarged Au 4f spectrum of Au-APAN.

Figure 64a and b displays representative absorbance and fluorescence spectra of AuNC (red line), APAN NP (blue line), and Au-APAN NP (black line). The AuNCs was showed a broad absorption band and emitted a strong orange fluorescence at 565 nm (λ_{ex}=290 nm) due to quantum confinement effect, which is similar result to previous reports.[126] In APAN NPs, absorption band was observed at 260 nm due to π-π* transition of the C=N group, and intense blue fluorescence was detected at 410 nm (λ_{ex}=290 nm).[118] The blue and orange fluorescence of APAN NP and AuNC were also confirmed by fluorescence photographs in Figure 64a. After the AuNC introduced on the surface of APAN NP, the fluorescence was changed into violet, neither blue nor red. Although the absorbance spectrum of Au-APAN NP was more similar to that of AuNC than APAN NP, Au-APAN NPs exhibited a dual-emission spectrum with two distinct fluorescence peaks (λ_{ex}=290 nm); one is at 405 nm from the APAN NP, and the other is at 560 nm from the decorated AuNCs on the surface of the APAN NP. The emission peaks originated from AuNC and APAN NP were respectively blue- and red-shifted by 5 nm, and they were well separated by 155 nm. Fluorescence spectra of Au-APAN NPs were analyzed at different excitation wavelength (Figure 64c). As excitation wavelength was changed from 270 nm to 310 nm, the emitted fluorescence intensity of APAN NP was gradually increased, while that of AuNC decreased simultaneously. The fluorescence intensity of APAN NP and AuNC was almost equal at an excitation wavelength of 290 nm, which is optimal

excitation wavelength for Au-APAN NP. The fluorescence quantum yield of the APAN

NP and AuNC were calculated as *ca.* 0.19 and *ca.* 0.11 using the standard reference, 7-

amino-4-methylcoumarin and rhodamine B. Collectively, these data verified the dual

emission property of Au-APAN NP and their enhanced resolution for monitoring and

bioimaging analysis.

To clarify the sensing ability of Au-APAN NPs, the selectivity of Au-APAN NP

was assessed by screening various biomolecules and ROS at a concentration of 1 mM

(Figure 64d). The intensity ratio of the two emission wavelengths (I_{405}/I_{560}) increased

by addition of the hROS (superoxide, hypochlorite, and hydroxyl radical), while no

fluorescence intensity change was detected in H_2O_2 (ROS) or other biomolecules.

Therefore, concentration dependent intensity ratio (I_{405}/I_{560}) change of Au-APAN NP

was evaluated focused on the hROS (Figure 64e, 6f, 65-67). The added hROS have

effect on both two emission wavelengths (I_{405}/I_{560}) of Au-APAN NP; a peak intensity

at 405 nm rapidly increased, whereas a peak at 560 nm showed gradual decline

(λ_{ex}=290 nm). The ratios of fluorescence intensities at 405 nm and 560 nm showed a

linear relationship with increasing hROS concentrations, suggesting that the Au-

APAN NP can be used as ratiometric sensor for hROS. The limit of detection (LOD)

was 1 nM, 5 nM, and 0.1 μM for superoxide, hydroxyl radical, and hypochlorite,

respectively. The LODs of Au-APAN NP for hypochlorite is 5 and 20 times better than

gold clusters decorated SiO_2 NPs and polyamidoamine dendrimers, respectively.[46,

127] In case of hydroxyl radical, Au-APAN NP also possesses 5 and 136 times lower LOD then gold clusters decorated SiO_2 nanoparticles and gold nanocluster, respectively.[45, 46] Only for superoxide, the LODs of Au-APAN NP is comparable to the previous reports.[50] In comparison with single wavelength emission system, change in dual emission wavelengths results in the enhanced sensitivity and resolution for ratiometric detection. Improved sensitivity of Au-APAN NP was also confirmed by inset images in Figure 64e. The fluorescence color changes of the Au-APAN NP are easy to be distinguished by the naked eye; the color was shifted from violet to blue by addition of hROS. Moreover, in the physiological concentrations, the minimum concentration of superoxide, hydroxyl radical, and hypochlorite is 0.1 nM, 50 nM, and 5 μM, respectively.[46, 128] Our LODs of Au-APAN NP is sufficient for detecting hROS in physiological concentration ranges, demonstrating the potential of Au-APAN NP for hROS detection under the physiological conditions with high sensitivity and selectivity.
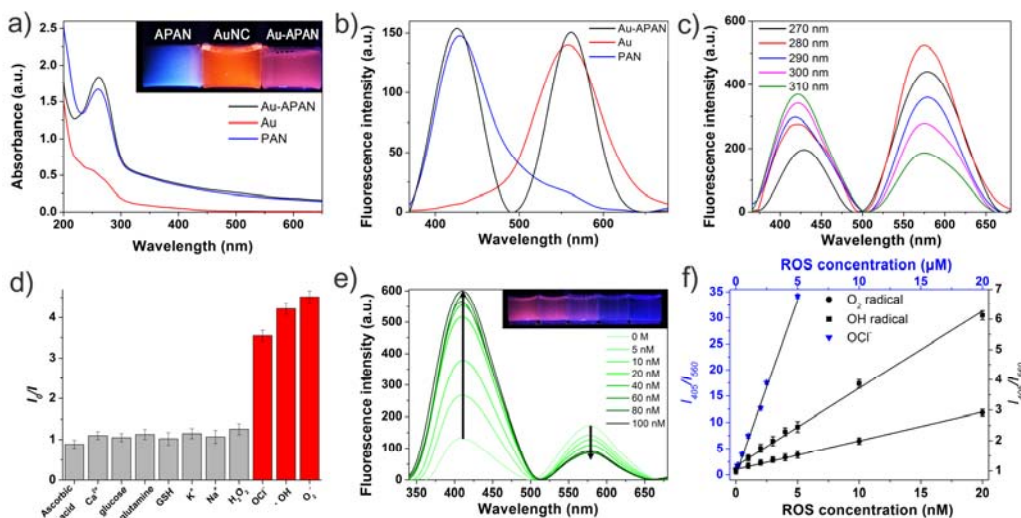
Figure 64. (a) UV-vis absorption spectra and (b) the representative fluorescence spectra of the AuNC (red), APAN NP (blue), and Au-APAN NP (black). (c) Fluorescence spectra of Au-APAN NPs at different excitation wavelength in 0.1 M HEPES buffer. (d) Selectivity of Au-APAN NPs (10 μg mL^{-1}) for different reactants (1 mM). (e) Fluorescence emission spectra of Au-APAN NPs in the presence of hydroxyl radicals at different concentrations (0-100 nM). (f) The relationship between emission fluorescence intensity of Au-APAN NPs and concentrations of hROS (superoxide, hypochlorite, and hydroxyl radical) was calculated. Insets: photograph taken with UV lamp irradiation (365 nm).
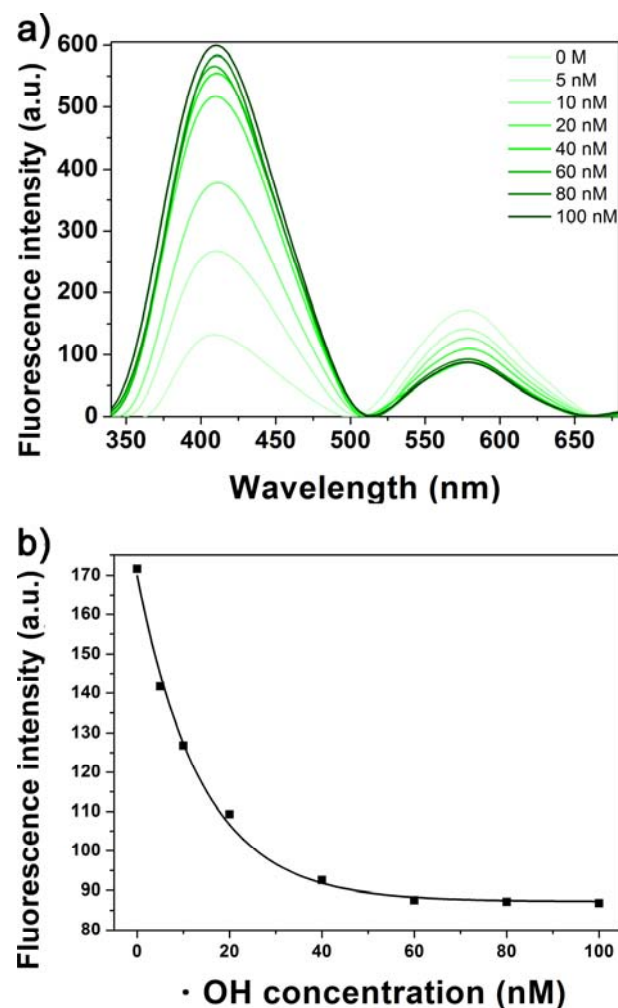
Figure 65. (a) Fluorescence spectral changes of Au-APAN NPs in the presence of hydroxyl radical (0-100 nM) and (b) their calibration plot.
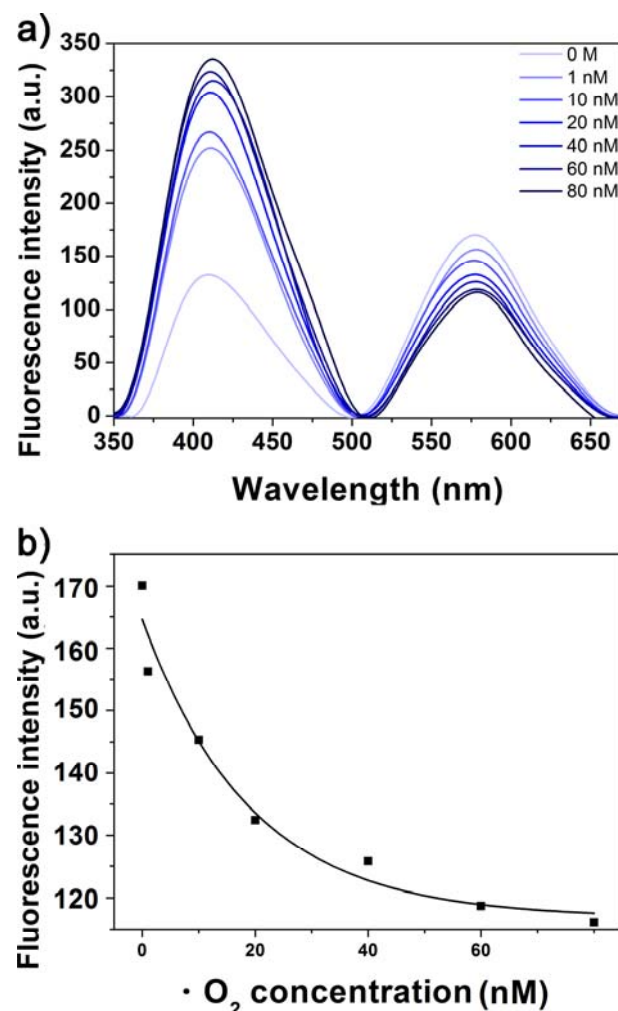
Figure 66. (a) Fluorescence spectral changes of Au-APAN NPs in the presence of superoxide radical (0-80 mM) and (b) their calibration plot.
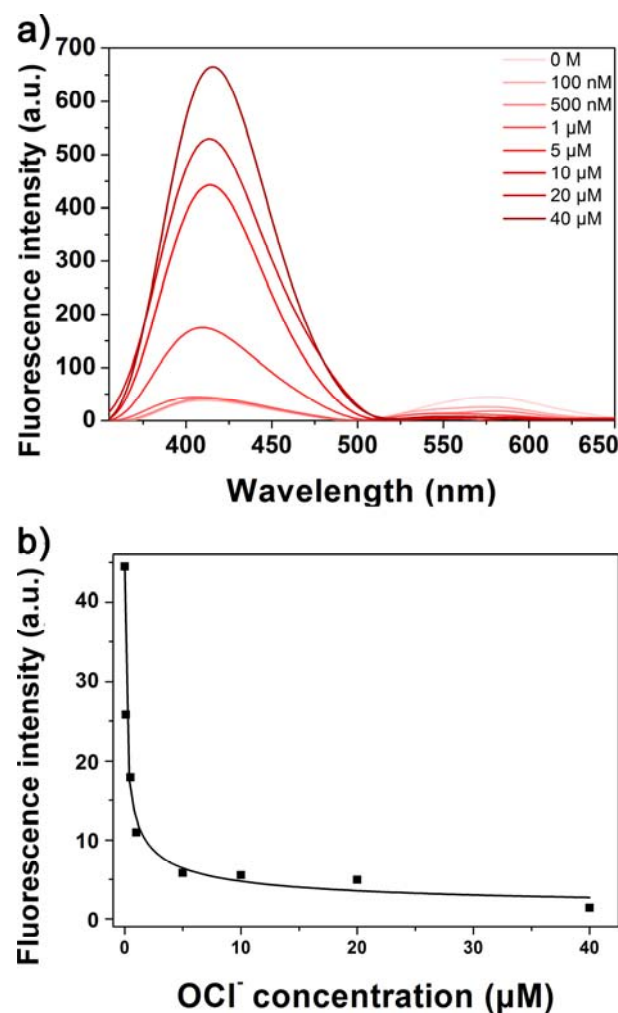
Figure 67. (a) Fluorescence spectral changes of Au-APAN NPs in the presence of hypochlorite (0-40 μM) and (b) their calibration plot.

3.3.2.2 Application for intracellular highly reactive oxygen species detection

To study the sensing ability of the Au-APAN NPs *in vitro*, mouse macrophage RAW264.7 cells were used as a model cells. RAW264.7 cells generate intracellular hROS in response to phorbol-12-myristate-13-acetate (PMA), making RAW264.7 cells suitable for investigating hROS signaling in mammalian system.[46, 119] Cellular uptake of Au-APAN NPs into RAW264.7 cells was first analyzed by TEM images. Most of the Au-APAN NPs were internalized and localized in endosomes without aggregation (Figure 68). After internalization, spherical shape of Au-APAN NPs was maintained and AuNCs still remained on the surface of APAN NPs (red arrow in the Figure 68c). The successfully internalized Au-APAN NPs were applied as fluorescence sensor probe for hROS detection in living cells.

The fluorescence images of Au-APAN NP treated RAW264.7 cells and their quantified results were shown in Figure 69a and e. Both blue and red fluorescence were observed at an excitation wavelength of 290 nm, leading the combination color as violet in differential interference contrast (DIC) images. After PMA treatment for 2 h, strong fluorescence signal was obtained in the blue channel, while no signal was captured in red channel due to reaction between AuNCs and hROS (Figure 69b). The quenched fluorescence of

AuNCs induced fluorescence color change from violet to blue in cells. Fluorescence quenching effect by PMA treatment on AuNCs also was confirmed by Figure 69e. Compared to the Au-APAN NP inserted cells, the median value and the ratio of red fluorescence exhibited cells decreased from 21.2 and 82% to 14.7 and 53% after PMA exposure. Three types of ROS scavenger were introduced into PMA and Au-APAN NP co-incubated cells to confirm monitoring ability of Au-APAN NP for ROS (Figure 69c, d, and f). First, 2,2,6,6-tetramethyl-piperidine-N-oxyl (TEMPO; superoxide dismutase mimic) was used for scavengers of O_2^- and inhibition of myeloperoxidase (enzyme for generating OCl^-).[46] In spite of PMA treatment, the bright red signal re-appeared in the cells, and the median value and the ratio of red fluorescent cell was returned to 21.5 and 81%. Instead of TEMPO, uric acid and dimethyl sulfoxide (DMSO) were selected for attenuating OCl^- and OCl^- /·OH, respectively.[46] When the uric acid and DMSO were added, the red fluorescence was recovered like TEMPO treated sample; however, the intensity was slightly weaker than that in TEMPO-inserted samples, indicating O_2^- was more generated than ·OH after PMA treatment. Moreover, the uneven fluorescence was observed in DIC image, which provides the location of O_2^- production. In case of conventional dyes for ROS, cells should be stained with another dye, which has different emission wavelength, for monitoring cells and

ROS at the same time. Au-APAN NPs, however, have the merit of dual-emission property; blue fluorescence visualizes the cells and red color provides the information of intracellular hROS. Therefore, Au-APAN NPs are capable of visualizing cell and intracellular ROS concurrently without additional staining for cell or ROS, which is appropriate for using sensor probe for hROS signaling.

Cytotoxicity is a crucial factor to be considered for application of Au-APAN NPs as intracellular sensor probe. To evaluate the effect of the Au-APAN NPs on the cells, adenosine triphosphate (ATP) based cell viability assay was conducted (Figure 70). ATP production in Au-APAN NPs-treated cells exhibited no significant decrease compared to negative control until at a concentration of 50 μg mL^{-1}. Even at a high concentration (100 μg mL^{-1}), the lowest viability was over 80%. Their ROS generating ability of the Au-APAN NPs was further verified because ROS production could have effect on not only toxicity but also accuracy of the sensing result of Au-APAN NPs. Compared to the negative control, the fluorescence intensity showed no significant change up to 100 μg mL^{-1}. These results implied that hROS detection results by Au-APAN NPs is reliable. Judging from these data, Au-APAN NPs, which has dual emission property, could provide both efficient cell imaging as well as hROS detection probe *in vitro* with low toxicity.
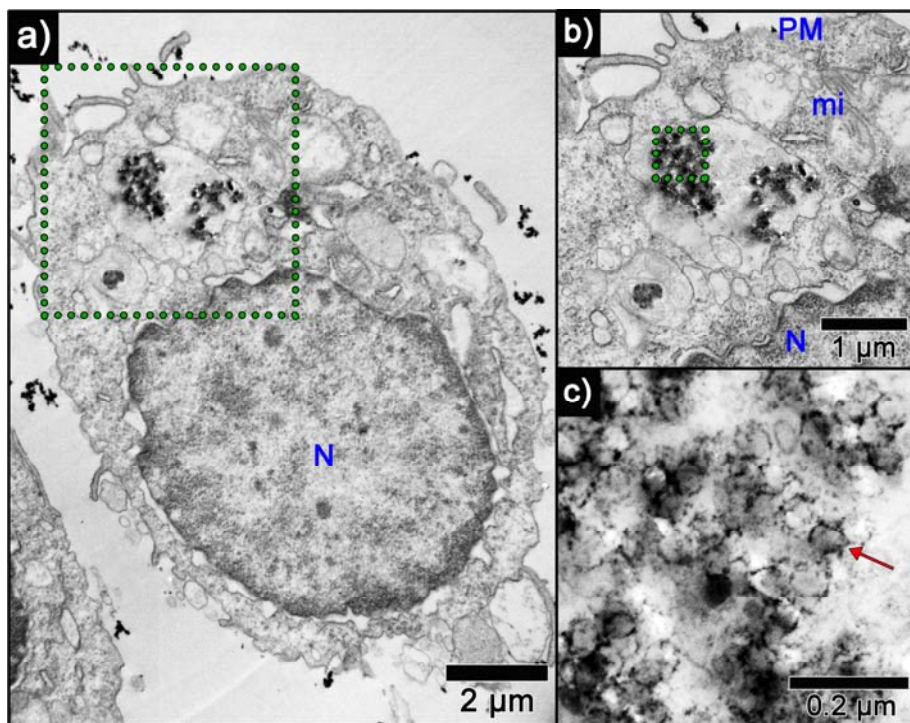
Figure 68. TEM images of RAW264.7 cells incubated with Au-APAN NPs for 24 h (25 μg mL^{-1}). Red arrow indicates the AuNCs on the Au-APAN NPs that are located in endosomes. Abbreviations: N as nucleus; PM as plasma membrane; mi as mitochondria.
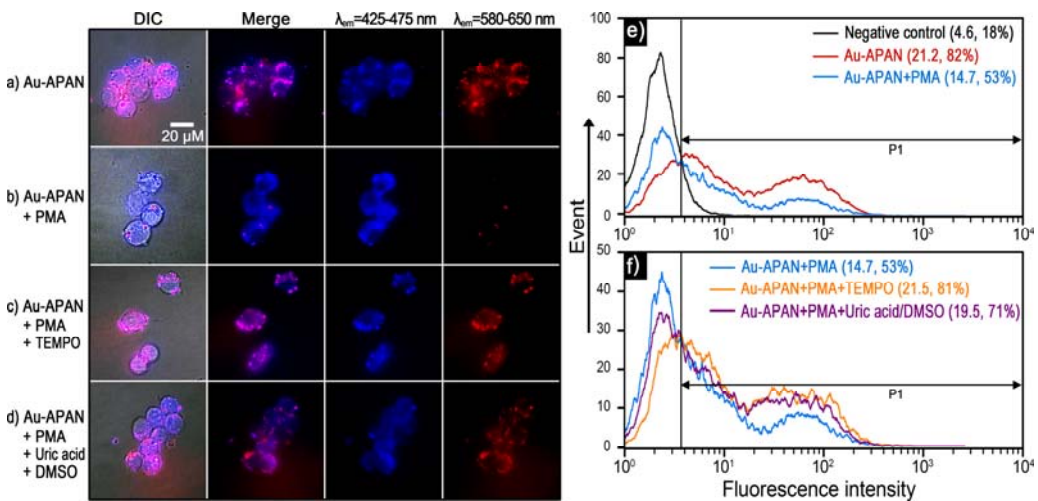
Figure 69. (a-d) Fluorescence images of Au-APAN NP treated RAW 264.7 cells. (e-f) Flow cytometry analysis of Au-APAN NPs inserted RAW264.7 cells based on the AuNCs (red fluorescence). The concentration of Au-APAN NP was 10 and 25 µg mL^{-1} in fluorescence images and flow cytometry analysis, respectively. Experimental conditions were below. Negative control: Non-Au-APAN NP treated cells. Au-APAN: cells were incubated with Au-APAN NPs for 24 h. Au-APAN NP+PMA: Cells treated with Au-APAN NPs for 24 h, followed by 1 µg mL^{-1} PMA for 2 h. Au-APAN NP+PMA+TEMPO: Cells treated with Au-APAN NPs for 24 h, followed by 1 µg mL^{-1} PMA for 2 h. Au-APAN NP+PMA+Uric acid/DMSO: Cells treated with Au-APAN NPs for 24 h, followed by 1 µg mL^{-1} PMA for 2 h. Then, 250 µM UA and 0.5% DMSO were inserted for additional 15 min.

Figure 70. Viability of and ROS production by RAW264.7 incubated with Au-APAN NPs for 24 h.

4. CONCLUSIONS

The multifunctional hybrid nanoparticles including five different metal oxide decorated SiO_2 nanoparticles, SiO_2/TiO_2 hollow nanoparticles, barium and strontium doped SiO_2/TiO_2 hollow nanoparticles, MnO_2 decorated PEDOT nanoparticles, gold nanocluster decorated PAN nanoparticles were prepared by diverse approaches. Furthermore, prepared nanomaterials exhibited the superior property in each application field owing to customized design of nanomaterials. The subtopics could be concluded in the view point of subtopics as follows;

1. Five different metal oxide (CeO_2, CuO, Fe_2O_3, MnO_2, and ZnO) decorated SiO_2 NPs were fabricated by sol-gel and chemical reduction method to accurately assess element-dependent toxicity. The size, shape, and metal oxide content of MOx-SiO_2 NPs were uniform, which made it possible to conduct a comparative study of element-dependent nanotoxicity. Based on toxic response, the MOx-SiO_2 NPs were classified into three groups; Group I, II, and III (less toxic, similar to, and more toxic than SiO_2 NPs). CeO_2 (Group I) reduced not only SiO_2 NP-treated toxicity, but also ROS production, owing to the Ce^{3+}/Ce^{4+} oxidation states. The toxicity of Fe-, Mn-, and Zn-SiO_2 NPs (Group III) was cell type-dependent, explained by DMT1 expression. These findings may provide a better understanding of comparative cytotoxicity for a library of nanomaterials with same physical

property, but with a wide range of elements.

2. Monodisperse HNP with diameters of 25, 50, 75, 100, and 125 nm were fabricated by sol-gel and a sonication mediated etching/redeposition method. The key factors affecting cellular uptake and nanotoxicity of HNPs with size-dependence were systematically investigated in human breast cancer SK-BR-3 and mouse alveolar macrophage J774A.1 cells. The number of cellular uptake of HNPs was in inverse proportion of HNP size, while the highest value of mean fluorescence intensity was HNP50. In addition the cellular uptake, the ATP production, apoptosis, and ROS revealed size-dependent toxicity of HNPs toward macrophages. These findings provide size-dependent nanotoxicity and uptake of HNPs, and lead to HNPs for bio-applications such as drug delivery and imaging probe.

3. The p-HNPs, Ba-HNPs, and Sr-HNPs were fabricated using sol-gel and sonication mediated etching/redeposition method and alkaline-earth metal hydroxide solution treatment to facilitate neuronal differentiation in cooperation with NGF. Regardless of HNP type, differentiation efficiency was improved by HNPs than NGF-only-treated cells though activating JNK, P38, and ERK pathways. Additionally, the average neurite length was in the order of Sr-HNP+NGF > Ba-HNP+NGF > p-HNP+NGF > NGF in all ranges of HNP concentrations. Doped Ba/Sr has influence on additional

elongation of the average neurite length though activating P38 and ERK pathways. To the best of our knowledge, this is the first investigation of the synergetic effects on promoting neuronal differentiation by Ba/Sr doped silica/titania hollow nanomaterials. To deliver NGF into cells efficiently, HNPs were further applied to encapsulate NGF. Neuronal differentiation was promoted by NGF encapsulated HNP than HNP with a daily addition of NGFs. Compared to previous research, NGF-Sr-HNP were exceptionally efficient for promoting neuronal differentiation. Therefore, Ba and Sr doped HNPs may provide a possibility for novel application of numerous metal-hybrid nanomaterials for cell differentiation.

4. PEDOT NPs were fabricated *via* chemical oxidation polymerization in reverse microemulsion and further modified with $KMnO_4$ to form MnO_2 domains on the PEDOT NPs by redox deposition. MnO_2/PEDOT NPs were investigated to enhance neurite outgrowth during differentiation and to enable real–time cellular monitoring of PC12 cells. PC12 cells showed enhanced differentiation with low toxicity in the presence of NGF+MnO_2/PEDOT NPs, where MnO_2 domains played a crucial role in facilitating the differentiation. Moreover, the MnO_2/PEDOT NPs were further applied as transducer for real–time monitoring of PC12 cells. The exocytosis of catecholamines triggered by plasma membrane depolarization

and the formation of Ca^{2+} selective ion channels was successfully detected by MnO_2/PEDOT sensor. The dual–functional MnO_2/PEDOT NPs offer a new method to induce neurite outgrowth and to detect exocytosed biomolecules.

5. An amidine modified PAN nanoparticle (APAN NPs) was prepared for the sensitive and selective detection of copper ion *in vitro*. PAN NPs were fabricated by sonication mediated emulsion polymerization, and further modified with amidine group by pinner method. Based on the quaching effect of the copper ion on APAN NPs, ratiometric detection were possible. Additionally, the limit of detection was 10 nM, which is better than or at least comparable to previous reports. The use of APAN NPs to detect intracellular copper ion was demonstrated in mammalian cells. The fluorescent APAN NPs with biocompatibility provide a new direction for the development of highly sensitive and selective sensors for intracellualr copper ions in living cells.

6. Au-APAN NPs were synthesized for use as a dual-emission fluorescent probe that can selectively detect intracellular hROS. The blue fluorescence peak from APAN NP increased with blue shift, while the red one from AuNCs decreased with red shift when the Au-APAN NPs reacted with hROS. This fluorescence behavior was highly selective for hROS, and

change in dual emission wavelengths results in the enhanced sensitivity and resolution for ratiometric detection. The use of these novel nanoparticles to detect changes in hROS concentration was demonstrated in macrophage cells. Considering these observations, the Au-APAN NPs offer a new way to selectively recognize hROS, and may lead to biomedical applications as an intracellular hROS sensor.

In summary, diverse multifunctional hybrid nanoparticles were fabricated, and evaluated their cytotoxicity, and applied as enhancement of neuronal differentiation and specific molecule detection. Three types of silica based hybrid nanoparticles were suggested by chemical reduction method and sonication mediated etching/redeposition methods. $MOx-SiO_2$ NP and HNPs were exhibited element- and size-dependent toxicity. The p-HNP, Ba-HNP, and Sr-HNPs were applied as neuronal differentiation enhancer, and further modified as encapsulating agent for nerve growth factor. Nerve growth factor encapsulating Sr-HNPs were exceptionally efficient for promoting neuronal differentiation. In case of polymer based hybrid nanoparticles, PEDOT and PAN NPs were respectively fabricated by chemical oxidation polymerization and sonication mediated emulsion polymerization, and used as substrate. Using redox deposition, MnO_2 were decorated on the PEDOT nanoparticles, and they

successfully enhanced the neuronal differentiation and detected the catecholamines released from the living cells. AuNCs were synthesized by chemical reduction method, and decorated on the APAN NPs. APAN NPs were used as fluorescence probe for monitoring of intracellular Cu^{2+} ion, and after AuNC decoration, they monitored hROS *in vitro* with dual emission property. Each hybrid nanoparticle are deliberately designed and customized of superior performance in specific applications. This study may provide understanding of fabricating various hybrid nanoparticles with multifunctionality and application of hybrid nanoparticles to biomedical application.

REFERENCES

[1]   R. Ma, T. Sasaki, *Adv. Mater.* **2010**, *22*, 5082.

[2]   W.-K. Oh, S. Kim, H. Yoon, J. Jang, *Small* **2010**, *6*, 872.

[3]   G. Bao, S. Mitragotri, S. Tong, *Annu. Rev. Biomed. Eng.* **2013**, *15*, 253.

[4]   J. Jang, K. Lee, *Chem. Commun.* **2002**, 1098.

[5]   H. Yoon, M. Chang, J. Jang, *Adv. Funct. Mater.* **2007**, *17*, 431.

[6]   J. Jang, J. Bae, E. Park, *Adv. Funct. Mater.* **2006**, *16*, 1400.

[7]   K. J. Lee, J. Yoon, S. Rahmani, S. Hwang, S. Bhaskar, S. Mitragotri, J. Lahann, *Proc. Natl. Acad. Sci. USA* **2012**, *109*, 16057.

[8]   L. Pan, H. Qiu, C. Dou, Y. Li, L. Pu, J. Xu, Y. Shi, *Int. J. Mol. Sci.* **2010**, *11*, 2636.

[9]   T. L. Kelly, M. O. Wolf, *Chem. Soc. Rev.* **2010**, *39*, 1526.

[10]   C. N. R. Rao, H. S. S. Ramakrishna Matte, R. Voggu, A. Govindaraj, *Dalton Trans.* **2012**, *41*, 5089.

[11]   B. L. Cushing, V. L. Kolesnichenko, C. J. O'Connor, *Chem. Rev.* **2004**, *104*, 3893.

[12]   J. He, M. T. Perez, P. Zhang, Y. Liu, T. Babu, J. Gong, Z. Nie, *J. Am. Chem. Soc.* **2012**, *134*, 3639.

[13]   R. Voggu, A. Shireen, C. N. R. Rao, *Dalton Trans.* **2010**, *39*, 6021.

[14]   Z. Xu, Y. Hou, S. Sun, *J. Am. Chem. Soc.* **2007**, *129*, 8698.

[15]   S. Y. Hwang, K. W. Kwon, K.-J. Jang, M. C. Park, J. S. Lee, K. Y. Suh, *Anal. Chem.* **2010**, *82*, 3016.

[16]   A. Janaszewska, M. Ciolkowski, D. Wróbel, J. F. Petersen, M. Ficker, J. B. Christensen, M. Bryszewska, B. Klajnert, *Nanomed. Nanotechnol. Biol. Med.* **2013**, *9*, 461.

[17]   B. D. Chithrani, A. A. Ghazani, W. C. W. Chan, *Nano Lett.* **2006**, *6*, 662.

[18]   F. Pagliari, C. Mandoli, G. Forte, E. Magnani, S. Pagliari, G. Nardone, S. Licoccia, M. Minieri, P. Di Nardo, E. Traversa, *ACS Nano* **2012**, *6*, 3767.

[19]   S. Hussain, F. Al-Nsour, A. B. Rice, J. Marshburn, B. Yingling, Z. Ji, J. I. Zink, N. J. Walker, S. Garantziotis, *ACS Nano* **2012**, *6*, 5820.

[20] N. Singh, G. J. S. Jenkins, R. Asadi, S. H. Doak, *Nano Reviews* **2010**, *1*, 5358.

[21] N. Lee, H. R. Cho, M. H. Oh, S. H. Lee, K. Kim, B. H. Kim, K. Shin, T.-Y. Ahn, J. W. Choi, Y.-W. Kim, S. H. Choi, T. Hyeon, *J. Am. Chem. Soc.* **2012**, *134*, 10309.

[22] S. E. Lohse, C. J. Murphy, *J. Am. Chem. Soc.* **2012**, *134*, 15607.

[23] C. Gunawan, W. Y. Teoh, C. P. Marquis, R. Amal, *ACS Nano* **2011**, *5*, 7214.

[24] C. M. Weekley, J. B. Aitken, S. Vogt, L. A. Finney, D. J. Paterson, M. D. de Jonge, D. L. Howard, P. K. Witting, I. F. Musgrave, H. H. Harris, *J. Am. Chem. Soc.* **2011**, *133*, 18272.

[25] Z. Ji, X. Wang, H. Zhang, S. Lin, H. Meng, B. Sun, S. George, T. Xia, A. E. Nel, J. I. Zink, *ACS Nano* **2012**, *6*, 5366.

[26] L. Zhang, T. J. Webster, *Nano Today* **2009**, *4*, 66.

[27] M. Georgiou, S. C. J. Bunting, H. A. Davies, A. J. Loughlin, J. P. Golding, J. B. Phillips, *Biomaterials* **2013**, *34*, 7335.

[28] J. A. Kim, N. Lee, B. H. Kim, W. J. Rhee, S. Yoon, T. Hyeon, T. H. Park, *Biomaterials* **2011**, *32*, 2871.

[29] J. M. Razal, M. Kita, A. F. Quigley, E. Kennedy, S. E. Moulton, R. M. I. Kapsa, G. M. Clark, G. G. Wallace, *Adv. Funct. Mater.* **2009**, *19*, 3381.

[30] Y. Luo, M. S. Shoichet, *Nat. Mater.* **2004**, *3*, 249.

[31] J. A. Roth, C. Horbinski, D. Higgins, P. Lein, M. D. Garrick, *Neurotoxicology* **2002**, *23*, 147.

[32] W. H. Lin, D. Higgins, M. Pacheco, J. Aletta, S. Perini, K. A. Marcucci, J. A. Roth, *J. Neurosci. Res.* **1993**, *34*, 546.

[33] J. Aaseth, G. Boivin, O. Andersen, *J. Trace Elem. Med. Biol.* **2012**, *26*, 149.

[34] L. Zhao, H. Wang, K. Huo, X. Zhang, W. Wang, Y. Zhang, Z. Wu, P. K. Chu, *Biomaterials* **2013**, *34*, 19.

[35] O. Z. Andersen, V. Offermanns, M. Sillassen, K. P. Almtoft, I. H. Andersen, S. Sørensen, C. S. Jeppesen, D. C. E. Kraft, J. Bøttiger, M. Rasse, F. Kloss, M. Foss, *Biomaterials* **2013**, *34*, 5883.

[36] F. Yang, D. Yang, J. Tu, Q. Zheng, L. Cai, L. Wang, *Stem Cells* **2011**, *29*, 981.

[37] Y. Xin, J. Jiang, K. Huo, T. Hu, P. K. Chu, *ACS Nano* **2009**, *3*, 3228.

[38] G. Ciofani, L. Ricotti, C. Canale, D. D'Alessandro, S. Berrettini, B. Mazzolai, V. Mattoli, *Colloid Surf. B-Biointerfaces* **2013**, *102*, 312.

[39] L. Schwartz, D. Atlas, *Neurosci. Lett.* **1992**, *146*, 17.

[40] W. H. Suh, K. S. Suslick, G. D. Stucky, Y. H. Suh, *Prog. Neurobiol.* **2009**, *87*, 133.

[41] G. A. Silva, *Nat. Rev. Neurosci.* **2006**, *7*, 65.

[42] Y. Liu, X. Dong, P. Chen, *Chem. Soc. Rev.* **2012**, *41*, 2283.

[43] S. Kim, W.-K. Oh, Y. S. Jeong, J. Jang, *Adv. Funct. Mater.* **2013**, *23*, 1947.

[44] W. Wang, S.-H. Zhang, L.-M. Li, Z.-L. Wang, J.-K. Cheng, W.-H. Huang, *Anal. Bioanal. Chem.* **2009**, *394*, 17.

[45] M. Zhuang, C. Ding, A. Zhu, Y. Tian, *Anal. Chem.* **2014**, *86*, 1829.

[46] T. Chen, Y. Hu, Y. Cen, X. Chu, Y. Lu, *J. Am. Chem. Soc.* **2013**, *135*, 11595.

[47] W.-K. Oh, Y. S. Jeong, K. J. Lee, J. Jang, *Anal. Methods* **2012**, *4*, 913.

[48] H. Sun, N. Gao, L. Wu, J. Ren, W. Wei, X. Qu, *Chem. Eur. J.* **2013**, *19*, 13362.

[49] P. G. Georgopoulos, A. Roy, M. J. Yonone-Lioy, R. E. Opiekun, P. J. Lioy, *J. Toxicol. Env. Health-Pt b-Crit. Rev.* **2001**, *4*, 341.

[50] N. Li, H. Wang, M. Xue, C. Chang, Z. Chen, L. Zhuo, B. Tang, *Chem. Commun.* **2012**, *48*, 2507.

[51] H. P. Indo, I. Nakanishi, K. Ohkubo, H.-C. Yen, M. Nyui, S. Manda, K.-i. Matsumoto, K. Fukuhara, K. Anzai, N. Ikota, H. Matsui, Y. Minamiyama, A. Nakajima, H. Ichikawa, S. Fukuzumi, T. Ozawa, C. Mukai, H. J. Majima, *RSC Adv.* **2013**, *3*, 4535.

[52] C. Kim, S. Kim, W.-K. Oh, M. Choi, J. Jang, *Chem. Eur. J.* **2012**, *18*, 4902.

[53] H. Yoon, J.-Y. Hong, J. Jang, *Small* **2007**, *3*, 1774.

[54] R. Liu, J. Duay, S. B. Lee, *ACS Nano* **2010**, *4*, 4299.

[55] Q. He, H. G. Sudibya, Z. Yin, S. Wu, H. Li, F. Boey, W. Huang, P. Chen, H. Zhang, *ACS Nano* **2010**, *4*, 3201.

[56] H. G. Sudibya, J. Ma, X. Dong, S. Ng, L. J. Li, X. W. Liu, P. Chen, *Angew. Chem. Int. Ed.* **2009**, *48*, 2723.

[57] K. J. Lee, W.-K. Oh, J. Song, S. Kim, J. Lee, J. Jang, *Chem. Commun.* **2010**, *46*, 5229.

[58]   Z. Luo, X. Yuan, Y. Yu, Q. Zhang, D. T. Leong, J. Y. Lee, J. Xie, *J. Am. Chem. Soc.* **2012**, *134*, 16662.

[59]   C. Yeonho, P. Younggeun, K. Taewook, P. L. Luke, *Nat. Nanotechnol.* **2009**, *4*, 742.

[60]   T. Xia, M. Kovochich, M. Liong, L. Mädler, B. Gilbert, H. Shi, J. I. Yeh, J. I. Zink, A. E. Nel, *ACS Nano* **2008**, *2*, 2121.

[61]   H. Zhang, Z. Ji, T. Xia, H. Meng, C. Low-Kam, R. Liu, S. Pokhrel, S. Lin, X. Wang, Y.-P. Liao, M. Wang, L. Li, R. Rallo, R. Damoiseaux, D. Telesca, L. Mädler, Y. Cohen, J. I. Zink, A. E. Nel, *ACS Nano* **2012**, *6*, 4349.

[62]   K. H. Müller, J. Kulkarni, M. Motskin, A. Goode, P. Winship, J. N. Skepper, M. P. Ryan, A. E. Porter, *ACS Nano* **2010**, *4*, 6767.

[63]   S. L. Montes-Fonseca, E. Orrantia-Borunda, A. Aguilar-Elguezabal, C. González Horta, P. Talamás-Rohana, B. Sánchez-Ramírez, *Nanomed. Nanotechnol. Biol. Med.* **2012**, *8*, 853.

[64]   J. Wu, C. Wang, J. Sun, Y. Xue, *ACS Nano* **2011**, *5*, 4476.

[65]   S. Kim, W.-K. Oh, Y. S. Jeong, J.-Y. Hong, B.-R. Cho, J.-S. Hahn, J. Jang, *Biomaterials* **2011**, *32*, 2342.

[66]   Ž. Krpetić, P. Nativo, I. A. Prior, M. Brust, *Small* **2011**, *7*, 1982.

[67]   E.-J. Yang, S. Kim, J. S. Kim, I.-H. Choi, *Biomaterials* **2012**, *33*, 6858.

[68]   J. R. Henderson, D. A. Fulton, C. J. McNeil, P. Manning, *Biosens. Bioelectron.* **2009**, *24*, 3608.

[69]   I. Celardo, M. De Nicola, C. Mandoli, J. Z. Pedersen, E. Traversa, L. Ghibelli, *ACS Nano* **2011**, *5*, 4537.

[70]   B. Reddy, A. Khan, *Catal. Surv. Asia* **2005**, *9*, 155.

[71]   M. S. Wason, J. Colon, S. Das, S. Seal, J. Turkson, J. Zhao, C. H. Baker, *Nanomed. Nanotechnol. Biol. Med.* **2013**, *9*, 558.

[72]   J. Wu, J. Sun, Y. Xue, *Toxicol. Lett.* **2010**, *199*, 269.

[73]   J. Park, D.-H. Lim, H.-J. Lim, T. Kwon, J.-S. Choi, S. Jeong, I.-H. Choi, J. Cheon, *Chem. Commun.* **2011**, *47*, 4382.

[74]   R. Foldbjerg, P. Olesen, M. Hougaard, D. A. Dang, H. J. Hoffmann, H. Autrup, *Toxicol. Lett.* **2009**, *190*, 156.

[75] M. Choi, C. Kim, S. Ok Jeon, K. Soo Yook, J. Yeob Lee, J. Jang, *Chem. Commun.* **2011**, *47*, 7092.

[76] T. Zhang, J. L. Stilwell, D. Gerion, L. Ding, O. Elboudwarej, P. A. Cooke, J. W. Gray, A. P. Alivisatos, F. F. Chen, *Nano Lett.* **2006**, *6*, 800.

[77] X. Huang, X. Teng, D. Chen, F. Tang, J. He, *Biomaterials* **2010**, *31*, 438.

[78] F. Osaki, T. Kanamori, S. Sando, T. Sera, Y. Aoyama, *J. Am. Chem. Soc.* **2004**, *126*, 6520.

[79] N. G. Bastús, E. Sánchez-Tilló, S. Pujals, C. Farrera, C. López, E. Giralt, A. Celada, J. Lloberas, V. Puntes, *ACS Nano* **2009**, *3*, 1335.

[80] Y. Yuan, C. Liu, J. Qian, J. Wang, Y. Zhang, *Biomaterials* **2010**, *31*, 730.

[81] A. Nel, T. Xia, L. Mädler, N. Li, *Science* **2006**, *311*, 622.

[82] L. A. Mitchell, F. T. Lauer, S. W. Burchiel, J. D. McDonald, *Nat. Nanotechnol.* **2009**, *4*, 451.

[83] J. Du, D. H. Daniels, C. Asbury, S. Venkataraman, J. Liu, D. R. Spitz, L. W. Oberley, J. J. Cullen, *J. Biol. Chem.* **2006**, *281*, 37416.

[84] J. Liu, J. Xu, R. Che, H. Chen, Z. Liu, F. Xia, *J. Mater. Chem.* **2012**, *22*, 9277.

[85] T. Cao, Y. Li, C. Wang, C. Shao, Y. Liu, *Langmuir* **2011**, *27*, 2946.

[86] J. Zhang, J. H. Bang, C. Tang, P. V. Kamat, *ACS Nano* **2009**, *4*, 387.

[87] Z. H. Chen, C. Kim, X.-B. Zeng, S. H. Hwang, J. Jang, G. Ungar, *Langmuir* **2012**, *28*, 15350.

[88] A. K. Gaharwar, S. M. Mihaila, A. Swami, A. Patel, S. Sant, R. L. Reis, A. P. Marques, M. E. Gomes, A. Khademhosseini, *Adv. Mater.* **2013**, *25*, 3329.

[89] S. Huang, P. J. Chueh, Y.-W. Lin, T.-S. Shih, S.-M. Chuang, *Toxicol. Appl. Pharmacol.* **2009**, *241*, 182.

[90] W.-K. Oh, S. Kim, M. Choi, C. Kim, Y. S. Jeong, B.-R. Cho, J.-S. Hahn, J. Jang, *ACS Nano* **2010**, *4*, 5301.

[91] M. Moriyama, H. Moriyama, A. Ueda, Y. Nishibata, H. Okura, A. Ichinose, A. Matsuyama, T. Hayakawa, *BMC Cell Biol.* **2012**, *13*, 21.

[92] D. E. Read, A. M. Gorman, *Cell. Mol. Life Sci.* **2009**, *66*, 2975.

[93] S. H. Bhang, T.-J. Lee, J. M. Lim, J. S. Lim, A. M. Han, C. Y. Choi, Y. H. Kim Kwon, B.-S. Kim, *Biomaterials* **2009**, *30*, 126.

[94] L. Meng, R. Chen, A. Jiang, L. Wang, P. Wang, C.-z. Li, R. Bai, Y. Zhao, H. Autrup, C. Chen, *Small* **2013**, *9*, 1786.

[95] X. Dong, W. Shen, J. Gu, L. Xiong, Y. Zhu, H. Li, J. Shi, *J. Phys. Chem. B* **2006**, *110*, 6015.

[96] X. Jin, W. Zhou, S. Zhang, G. Z. Chen, *Small* **2007**, *3*, 1513.

[97] R. Liu, H. Liu, Z. Qiang, J. Qu, G. Li, D. Wang, *Journal of Colloid and Interface Science* **2009**, *331*, 275.

[98] N. B. Patel, D. B. Mistry, *Int. J. Polym. Mater.* **2004**, *53*, 653.

[99] D. G. Drubin, S. C. Feinstein, E. M. Shooter, M. W. Kirschner, *J. Cell. Biol.* **1985**, *101*, 1799.

[100] A. A. Gilad, P. Walczak, M. T. McMahon, B. N. Hyon, H. L. Jung, K. An, T. Hyeon, P. C. M. Van Zijl, J. W. M. Bulte, *Magn. Reson. Med.* **2008**, *60*, 1.

[101] J. Shin, R. M. Anisur, M. K. Ko, G. H. Im, J. H. Lee, I. S. Lee, *Angew. Chem. Int. Ed.* **2009**, *48*, 321.

[102] K. M. Erikson, K. Thompson, J. Aschner, M. Aschner, *Pharmacol. Ther.* **2007**, *113*, 369.

[103] J. R. Casey, S. Grinstein, J. Orlowski, *Nat. Rev. Mol. Cell Biol.* **2010**, *11*, 50.

[104] O. Tsiklauri, T. Marsagishvili, G. Tsurtsumiya, S. Kirillov, D. Dzanashvili, *Russ. J. Electrochem.* **2008**, *44*, 1166.

[105] E. M. Shapiro, A. P. Koretsky, *Magn. Reson. Med.* **2008**, *60*, 265.

[106] C. Au, A. Benedetto, M. Aschner, *Neurotoxicology* **2008**, *29*, 569.

[107] S. Cassano, S. Agnese, V. D'Amato, M. Papale, C. Garbi, P. Castagnola, M. R. Ruocco, I. Castellano, E. De Vendittis, M. Santillo, S. Amente, A. Porcellini, E. V. Avvedimento, *J. Biol. Chem.* **2010**, *285*, 24141.

[108] M. B. Steketee, S. N. Moysidis, X.-L. Jin, J. E. Weinstein, W. Pita-Thomas, H. B. Raju, S. Iqbal, J. L. Goldberg, *Proc. Natl. Acad. Sci. USA* **2011**, *108*, 19042.

[109] T.-I. Chao, S. Xiang, J. F. Lipstate, C. Wang, J. Lu, *Adv. Mater.* **2010**, *22*, 3542.

[110] D. Liu, X. He, K. Wang, C. He, H. Shi, L. Jian, *Bioconjugate Chem.* **2010**, *21*, 1673.

[111] M. S. Qiu, S. H. Green, *Neuron* **1992**, *9*, 705.

[112] W. Wang, S. H. Zhang, L. M. Li, Z. L. Wang, J. K. Cheng, W. H. Huang, *Anal.*

Bioanal. Chem. **2009**, *394*, 17.

[113] D. M. Omiatek, Y. Dong, M. L. Heien, A. G. Ewing, *ACS Chem. Neurosci.* **2010**, *1*, 234.

[114] U. Mittnacht, H. Hartmann, S. Hein, H. Oliveira, M. Dong, A. P. Pêgo, J. Kjems, K. A. Howard, B. Schlosshauer, *Nano Lett.* **2010**, *10*, 3933.

[115] T. Cohen-Karni, Q. Qing, Q. Li, Y. Fang, C. M. Lieber, *Nano Lett.* **2010**, *10*, 1098.

[116] X. Duan, R. Gao, P. Xie, T. Cohen-Karni, Q. Qing, H. S. Choe, B. Tian, X. Jiang, C. M. Lieber, *Nat. Nanotechnol.* **2012**, *7*, 174.

[117] W.-K. Oh, Y. S. Jeong, J. Song, J. Jang, *Biosens. Bioelectron.* **2011**, *29*, 172.

[118] L. Yang, W. Zhu, M. Fang, Q. Zhang, C. Li, *Spectroc. Acta Pt. A-Molec. Biomolec. Spectr.* **2013**, *109*, 186.

[119] W.-K. Oh, Y. S. Jeong, S. Kim, J. Jang, *ACS Nano* **2012**, *6*, 8516.

[120] X. Liu, H. Chen, C. Wang, R. Qu, C. Ji, C. Sun, Y. Zhang, *J. Hazard. Mater.* **2010**, *175*, 1014.

[121] S. Deng, R. Bai, J. P. Chen, *J. Colloid Interface Sci.* **2003**, *260*, 265.

[122] Z. Li, L. Zhang, L. Wang, Y. Guo, L. Cai, M. Yu, L. Wei, *Chem. Commun.* **2011**, *47*, 5798.

[123] A. Zhu, Q. Qu, X. Shao, B. Kong, Y. Tian, *Angew. Chem. Int. Ed.* **2012**, *51*, 7185.

[124] M. A. Habeeb Muhammed, P. K. Verma, S. K. Pal, A. Retnakumari, M. Koyakutty, S. Nair, T. Pradeep, *Chem. Eur. J.* **2010**, *16*, 10103.

[125] H. Wu, L. Wang, J. Zhang, Z. Shen, J. Zhao, *Catal. Commun.* **2011**, *12*, 859.

[126] J. Zheng, C. Zhou, M. Yu, J. Liu, *Nanoscale* **2012**, *4*, 4073.

[127] T.-H. Wu, C.-P. Liu, C.-T. Chien, S.-Y. Lin, *Chem. Eur. J.* **2013**, *19*, 11672.

[128] E. Cadenas, K. J. A. Davies, *Free Radic. Biol. Med.* **2000**, *29*, 222.

국문초록

최근, 나노 크기의 단일시스템 안에 다양한 요소들을 도입하는 연구가 생명과학 분야에서 많은 관심을 받고 있다. 기존의 물질이나 단일 요소로 구성된 나노 물질에 비해, 복합 나노 물질은 다양한 분야에서 매우 뛰어난 성능을 발휘하며 또한 다 기능성을 가지고 있다는 장점이 있다. 이에 나노 기술의 발전과 함께 복합 나노 물질을 제조하는 연구가 활발히 진행되고 있다. 나노 입자는 이런 복합성을 가질 수 있는 가장 기본적인 구조이며, 또한 다른 나노 구조체에 비해 세포 내에 가장 많이 도입될 수 있는 형태이다. 하지만, 생명과학분야에 적합한 복합 나노 입자를 제조하는 연구에 관한 보고는 여전히 부족한 실정이다.

본 학위논문에서는 다 기능성을 가진 복합 나노 입자를 제조하여 세포 내 독성을 평가하여 보았으며, 또한 본 입자를 신경세포 분화 촉진과 특정 분자 검출에 응용 하였다. 본 학위논문은 실리카 기반, 피돗 기반, 그리고 폴리아크릴로니트릴 기반 복합 나노 입자, 이렇게 총 세 개의 부분으로 구성되어 있다.

세가지 종류의 실리카 기반 복합 나노 입자는 화학적 환원방법과 초음파 매개 에칭/재증착 방법을 통해 제조하였다. 다섯 가지 다른 종류의 산화금속(이산화세륨, 산화구리, 산화철, 이산화망간, 그리고 산화아연)이 도입된 실리카 나노 입자와 실리카/티타니아 중공 나노 입자는 각각 원소와 크기 의존적인 독성이 조사되었다. 그리고 바륨과 스트론튬이

192

도핑된 실리카/티타니아 중공 나노 입자는 신경 분화 촉진제로 응용하였으며, 더 나아가 신경성장인자의 전달체로 사용하였다. 신경성장인자가 도입된 스트론튬이 도핑된 실리카/티타니아 중공 나노 입자가 가장 뛰어난 분화 촉진 효과를 발휘하였다.

피돗 나노 입자는 에멀젼 상에서 산화중합을 통해 제조되었으며, 기판으로 이용되었다. 이산화망간을 피돗 나노 입자 표면에 산화환원 증착방법을 통해 도입하였으며, 제조된 본 복합 나노 입자는 신경세포 분화를 촉진시켰으며, 또한 살아있는 세포에서 방출되는 카테콜아민을 성공적으로 감지하였다.

아미딘이 도입된 폴리아크릴로니트릴 나노 입자는 초음파 매개 에멀젼 중합을 통해 제조되었으며, 피너방법을 통해 아미딘그룹으로 표면이 개질 되었다. 생체친화성을 가지고 있는 형광 아미딘-폴리아크릴로니트릴 나노 입자는 살아있는 세포 안에 있는 구리 이온에 대해 높은 민감도와 선택성을 가지는 센서 개발에 있어 새로운 방향성을 제시하여 주었다. 또한, 금 나노 클러스터를 합성하여 본 아미딘-폴리아크릴로니트릴 나노 입자 표면에 도입하였으며, 이에 두 가지 형광을 동시에 발휘하는 복합 나노 입자가 제조 되었다. 이중 형광 성질은 특정 활성산소종에 대해 높은 선택성을 발휘하였으며, 또한 비례적인 감지를 위한 높은 민감도와 해상도를 제공하였다. 낮은 독성을 가지고 있는 금 나노 클러스터-아미딘-폴리아크릴로니트릴 복합 나노 입자는 생체 내에서 효과적으로

세포를 이미징하는 에이전트로 적용이 될 수 있으며, 동시에 특정 활성산소종을 감지하는 센서로도 적용 될 수 있다.

본 학위 논문에서는 복합 나노 입자를 제조하는 다양한 방법과 생명과학분야 응용 가능성에 관한 연구를 수행하였다. 본 학위논문에서 제조된 다 기능성 복합 나노 입자들은 신경분화 촉진제, 카테콜아민 센서, 그리고 형광 감지 탐침 같은 생명과학분야에 응용하였다. 본 입자들은 각각의 응용에 적합하고 최적의 성능을 낼 수 있도록 디자인되고 제조되었다. 이런 결과들은 다양한 다 기능성의 복합 나노 입자를 제조하고, 이들을 생명과학분야에 적용하는 것에 관한 정보들을 제공하게 될 것이다.

주요어: 복합 나노 입자; 다 기능성; 세포 독성; 신경 분화; 카테콜아민 센서; 형광 센서

학번: 2009-20981